UNIVERSITY OF CALIFORNIA
SANTA CRUZ

UNLOCKING TIME-DOMAIN & MULTIMESSENGER ASTROPHYSICS AND THE DISCOVERY OF THE FIRST OPTICAL COUNTERPART TO A GRAVITATIONAL WAVE SOURCE

A dissertation submitted in partial satisfaction of the
requirements for the degree of

Doctor of Philosophy

in

ASTRONOMY AND ASTROPHYSICS

by

David A. Coulter

September 2023

The Dissertation of David A. Coulter is approved:

Enrico Ramirez-Ruiz, Chair

Ryan J. Foley

Daniel Kasen

S. Bradley Cenko

Peter F. Biehl
Vice Provost and Dean of Graduate Studies

Table of Contents

List of Figures

List of Tables

Abstract

Unlocking Time-domain & Multimessenger Astrophysics

and the

Discovery of the First Optical Counterpart to a Gravitational Wave Source

by

David A. Coulter

The modern study of astrophysics is being transformed by advances across multiple fronts. New fast, wide, deep, and multi-color surveys are pushing into novel parameter spaces and generating an exponentially growing volume of data. Simultaneously, the first direct detection of gravitational waves (GWs) in 2015 has created a global race to search for their luminous counterparts. Here I present three major results that reside at the intersection of this new science and the methods, algorithms, and technology that enable it. The first is `YSE-PZ`, a transient survey management platform that enables three major transient surveys: the Young Supernova Experiment, the Keck Infrared Transient Survey, and the Swope Supernova Survey. Second, I describe the discovery of the first optical counterpart to gravitational wave source, the kilonova (KN) SSS17a/AT 2017gfo. Discovering the KN and localizing it to the galaxy NGC 4993 paved the way for all the science that followed: it confirmed that there are electromagnetic (EM) counterparts to GWs, it allowed a redshift of NGC 4993 to be combined with the GW-derived luminosity distance to GW170817 and enabled the first standard siren measurement of H_0, and lead to the ability for rapid follow-up observations to confirm that binary neutron star (BNS) mergers are prolific astrophysical sites for the synthesis of the r-process elements. Finally, I

present a new ultraviolet, optical, and infrared search for the electromagnetic (EM) counterpart to GW190425, the second-ever BNS merger discovered by the LIGO-Virgo-KAGRA Collaboration (LVK). Intrinsic properties and observational limitations meant that any counterpart to GW190425 would be much harder to discover than SSS17a was, and neither our search, nor the broader EM community's search, discovered a credible counterpart. I contrast this speculative counterpart to SSS17a and discuss how KN diversity complicates our picture of heavy-element nucleosynthesis. I perform a combined analysis of the EM community's search for GW190425 using a new GW search and analysis tool called `Teglon`. Through `Teglon`, I calculate the most comprehensive upper limits on this potential EM counterpart to GW190425, as well as discuss opportunities for enhancing the community's coordination for the next BNS GW event in the LVK's fourth observing run and beyond.

For Monine. Through your love, all things are possible.

Personal Acknowledgments

For the sake of all, I will try to keep acknowledgements brief and in no particular order. It takes a village to raise a Ph.D.; everyone along the way makes the climb possible and the summit worth it.

To my girls, Noa and Zoe: Anything is possible!

To my Mom: No matter how old he may get, a son will always need his mother.

To my Dad: You're right, I'm not a rocket scientist. I wish you could've been here.

To Ryan: Thank you for your vision and your scientific insight. Without your guidance and support, I would not be here.

To my Thesis Committee: Thank you for taking me on and pushing me to become better.

To Capt. Brad and all the crew on Hijinx 1.0 & 2.0: Three, two, one, *helm's over*!

To Charlie and Peter: You both have given me a lot to look up to, and a lot to live up to; thank you both dearly.

Published Material

The text of this dissertation includes reprints of the following published material led by Coulter, with the permission of the listed coauthors.

Chapter 2 was published in the literature as Coulter et al. (2022). I was responsible for the architecture of the data model and application, writing the core code base, writing text, and creating the figures. I wish to thank my coauthors David Jones and Peter McGill for their tireless efforts in building out the code base, documentation, continuous integration, virtualization, and contributing toward the text. I also wish to thank my coauthor Ryan J. Foley for his generous support and feedback in the course of this research.

Chapter 3 was published in the literature as Coulter et al. (2017a). I was responsible for performing the analysis, writing the text, and creating the figures. I wish to thank my coauthor Ryan J. Foley, collaborators from the Carnegie Observatories, and the UC Santa Cruz One Meter, Two Hemispheres Collaboration for their generous support and feedback in the course of this research.

Scientific Acknowledgments

I gratefully acknowledge research support from the National Science Foundation Graduate Research Fellowship Program Under Grant No. DGE1339067. The UCSC transients team is supported in part by NASA grants NNG17PX03C, 80NSSC18K0303, 80NSSC19K0113, 80NSSC19K1386, 80NSSC20K0953, 80NSSC21K2076, 80NSSC22K1513, 80NSSC22K1518, and 80NSSC23K0301; NSF grants AST–1720756, AST–1815935, and AST–1911206; grants associated with Hubble Space Telescope programs DD– 14925, DD–15600, GO–15876, GO–16238, SNAP– 16239, GO–16690, SNAP–16691, and GO–17128; the Gordon & Betty Moore Foundation; the Heising-Simons Foundation, generous donations from many individuals through a UCSC Giving Day grant, by fellowships from the Alfred P. Sloan Foundation (R.J.F.), the David and Lucile Packard Foundation to (R.J.F. and E.R.), and the Niels Bohr Professorship from the DNRF (E.R.).

I thank the LIGO/Virgo Collaboration, and all those who have contributed to gravitational wave science for enabling this discovery. I thank J. McIver for alerting us to the LVC circular. I thank J. Mulchaey (Carnegie Observatories director), L. Infante (Las Campanas Observatory director), and the entire Las Campanas staff for their extreme dedication, professionalism, and excitement, all of which were critical in the discovery of the first gravitational wave optical counterpart and its host galaxy as well as the observations used in this study. I thank the University of Copenhagen, DARK Cosmology Centre, and the Niels Bohr International Academy for hosting D.A.C., R.J.F., A.M.B., E.R., and M.R.S. during the discovery of GW170817/SSS17a.

Calculations presented in Coulter et al. (2017a) used resources of the National Energy

Research Scientific Computing Center (NERSC), which is supported by the Office of Science of the U.S. Department of Energy under Contract No. DE-AC02-05CH11231. The Computational HEP program in The Department of Energy's Science Office of High Energy Physics provided resources through Grant #KA2401022. Coulter et al. (2017a) includes data gathered with the 6.5 meter Magellan Telescopes located at Las Campanas Observatory, Chile. This research has made use of the NASA/IPAC Extragalactic Database (NED) which is operated by the Jet Propulsion Laboratory, California Institute of Technology, under contract with the National Aeronautics and Space Administration. Figure 4A from Coulter et al. (2017a) is based on observations made with the NASA/ESA Hubble Space Telescope, obtained from the Data Archive at the Space Telescope Science Institute (https://archive.stsci.edu; Program 14840), which is operated by the Association of Universities for Research in Astronomy, Inc., under NASA contract NAS 5–26555. These observations are associated with programs GO–14840. The data presented in Coulter et al. (2017a) and the code used to perform the analysis are available at `https://ziggy.ucolick.org/sss17a/`.

For my work on GW190425, I appreciate the expert assistance of the staffs at the various observatories where data were obtained. I thank S. Wyatt, A. Tohuvavohu, and I. Arcavi for their work on Treasure Map, as well as in providing data for the LCOGT portion of the anlysis, L. Singer and M. Coughlin for their guidance and expertise on a range of gravitational wave astronomy topics, and R. Hausen and P. McGill for input on software engineering, A. Palmese for her peer review, and D. Jones for help in quantifying our limits. I also acknowledge the use of public data from the *Swift* data archive. C.D.K. is partially supported by a CIERA postdoctoral fellowship, and M.R.S. is supported by the STScI Postdoctoral Fellowship.

Chapter 1

Introduction

1.1 An Exponential Growth in Transient Science

The modern study of astrophysical transients has been transformed by an exponentially growing volume of data. This growth is driven by the transition from narrow-field, galaxy-targeted surveys (e.g., the Lick Observatory Supernova Search; Filippenko et al. 2001) to wide-field time-domain surveys (e.g., All-Sky Automated Survey for Supernovae (ASAS-SN; Shappee et al. 2014), the Young Supernova Experiment (YSE; Jones et al. 2021), and the Zwicky Transient Facility (ZTF; Bellm et al. 2019a); see Chapter 2 for a more complete list). The discovery rate is expected to further increase by an additional order of magnitude with the start of survey operations for the Vera Rubin Observatory's Legacy Survey of Space and Time (LSST; LSST Science Collaboration et al. 2009b) and the Nancy Grace Roman Space Telescope (Spergel et al. 2015). In addition to this explosion in science data, associated survey data, archival data, and metadata are also increasing with the number of discoveries.

These fast, wide, deep, and multicolor surveys are revolutionizing transient astronomy. High cadence observations reveal physics only accessible with rapid follow-up observations. For supernovae, observations obtained within hours of explosion for can probe the outermost layers of the progenitor star (e.g., Soderberg et al. 2008; Modjaz et al. 2009; Ofek et al. 2010; Bloom et al. 2012; Tinyanont et al. 2022), illuminate any circumstellar material before it is swept up by the incoming SN ejecta (e.g., Sternberg et al. 2011; Gal-Yam et al. 2014; Jacobson-Galán et al. 2020a, 2022a; Terreran et al. 2022), and reveal details of the progenitor system (e.g., Marion et al. 2016; Hosseinzadeh et al. 2017; Dimitriadis et al. 2019a; Shappee et al. 2019; Miller et al. 2020). However, astronomical facilities are still relatively few and oversubscribed, and to realize transient science goals requires balancing scientific, technical, and human resources. Without efficient ways to manage this deluge of data, we risk missing new and interesting events, or may fail to recognize or respond to opportunities to uncover novel or unexpected physics.

Therefore, to make the most of the science that is being enabled by advances in technology and survey design, the community needs to make a commensurate investment in the software used to bridge the gap between data and information, and to empower scientists to take the appropriate actions at the appropriate time. Furthermore, the way that software is developed is increasingly important. Scientific code bases are built in isolation, are generally slow to adopt industry best practices, and there is a wide variance in whether authors of code use source control, implement object-oriented design principles (or some other clearly understood design concept), write clear documentation that is maintained, or implement testing harnesses or continuous integration to manage code quality.

To rise to these challenges, NASA has formalized these best practices into a vision for

software development that emphasizes transparency, accessibility, inclusivity, and reproducibility called the Open-Source Science Initiative (OSSI)[1]. At its core, the OSSI seeks to set a culture that can both scale with the growth of astronomical data and its complexity while breaking down barriers to its understanding. While NASA is leading the way in promoting open science, it is up to scientists to follow and to build out systems and tools that embody these tenets. This sea change in how science can be done is fortuitously timed to coincide with one of the most recent and technologically demanding revolutions in astrophysics: gravitational wave astronomy.

1.2 Gravitational Waves and Promise of Multimessenger Astronomy

In 2015, the Laser Interferometer Gravitational-Wave Observatory (LIGO) directly detected gravitational waves (GWs) from a pair of merging black holes (BHs) (Abbott et al. 2016c), and was awarded the 2017 Nobel Prize in Physics for opening a new window into the Universe. In the inspiral during the last seconds before merger, extragalactic GW radiation becomes strong enough that a network of terrestrial GW detectors, the LIGO, Virgo, and KAGRA collaboration (LVK), can detect not only the existence of these massive and compact systems, but can infer the distance to the progenitor system, it's angular momentum, and even it's tidal deformability. However, without interactions with surrounding baryons, merging BHs are not expected to produce a luminous counterpart.

This basic picture is different for systems that include a neutron star (NS) component — for instance, a binary neutron star (BNS) or neutron-star black hole (NSBH) system. For

[1] https://science.nasa.gov/open-science-overview

these systems, it is in principle possible to detect EM counterparts. Such systems have long been thought to be the progenitors of short gamma-ray bursts (sGRB) due to their energetics (isotropic energies of 10^{54} erg) and variability timescales of milliseconds (setting the progenitor size scales to hundreds or thousands of kilometers; Berger 2014). In addition to non-thermal EM counterparts, the disruption of a NS can produce $\sim$0.01–0.1 $M_\odot$ of radioactive, r-process rich material (Metzger 2019). As this material decays, it heats the ejecta and creates a "kilonova" (KN) (e.g., Roberts et al. 2011; Kasen et al. 2013; Li & Paczyński 1998; Metzger et al. 2010) which can be detected in ultraviolet, optical, and infrared wavelengths (denoted collectively as UVOIR emission).

Combining information from more than one fundamental force of nature, i.e., "multimessenger" astronomy (MMA), allows us to probe physical phenomena not available to each signal alone. The first time such a feat was achieved was in 1987, with the optical discovery of supernova (SN) 1987A in the Large Magellanic Cloud (Kunkel et al. 1987), accompanied by a detection of neutrinos at Japan's Kamiokande-II neutrino detector (Hirata et al. 1987). This event marked the first direct detection of neutrinos known to be associated with a SN, and through connecting these particles to SN 1987A, they informed the physics of how core-collapse SNe explode, how NSs form, and set the mass and charge limits for neutrinos themselves (Arnett et al. 1989).

In the same vein, detecting an EM counterpart to a GW would be similarly revolutionary. Because GWs encode the luminosity distance to the progenitor system in the GW itself, localizing a luminous counterpart to a host galaxy and obtaining its redshift would provide a direct measurement of Hubble's Constant, H_0, called a standard siren (Holz & Hughes

2005). Furthermore, detecting the UVOIR emission from a KN and modeling its peak luminosity, time scale for evolution, and color evolution (and thus, opacity), would reveal the presence of r-process elements (Kasen et al. 2013). Finally, by combining GW measurements of the progenitor's total system mass with models of the KN emission, the eventual fate of the remnant could be ascertained – either a black hole, unstable (i.e., rotationally supported) neutron star, or a stable neutron star. This in turn would inform the maximum mass of a neutron star, the Tolman–Oppenheimer–Volkoff mass, $M_{\rm TOV}$ (Oppenheimer & Volkoff 1939; Tolman 1939).

Despite this incredible potential for scientific advancement, finding an EM counterpart is incredibly challenging because the triangulated sky localizations for GW events are based on the "time-of-arrival" differences measured by terrestrial GW detectors. This measurement is difficult both because of the large speed of light compared to the separations of detectors, and the fact that it is rare for all of the LVK's detectors to be online simultaneously. The result are localizations that tend to be hundreds or thousands of square degrees. In addition, the EM counterparts to these events are also incredibly faint and fade quickly. To understand why requires a detailed look at the anatomy of a kilonova.

1.3 Kilonovae

Since the seminal work of Burbidge et al. (1957), it has been known that approximately half of all elements heavier than iron require a nucleosynthetic pathway that does not occur during the course of normal stellar fusion. Such a pathway necessitates a physical situation where many neutrons can be captured by a seed nuclei faster than the β-decay timescale, and that results in the formation of neutron-rich, heavy isotopes which are radioactively unstable.

This process is referred to as the rapid neutron capture process, or r-process. For it to proceed, there needs to be a relative abundance of neutrons. This abundance is quantified as the *electron fraction*, or the fraction of charged particles over all nucleons in a medium,

$$Y_e \equiv \frac{n_p}{n_p + n_n} \tag{1.1}$$

where n_p is the number density of protons and n_n is the number density of neutrons. For a medium to be "neutron-rich", $Y_e < \frac{1}{2}$ is required. Lattimer & Schramm (1974) first postulated that an astrophysical site for such an excess of neutrons could be in the mergers of BHs and NSs. In such a merger, after a NS has been tidally shredded, this material would undergo violent decompression and provide the flux of neutrons required for the r-process to proceed.

In the ejecta of such an event, heavy isotopes are rapidly built up, creating radioactive nuclei far from the valley of beta stability. An ensemble of isotopes then decay according to their half lives, with a characteristic net heating rate,

$$\dot{Q} \propto t^{-1.3} \tag{1.2}$$

where $\dot{Q}$ is the r-process heating rate, and t is in days (Metzger et al. 2010; Roberts et al. 2011). For some of the heaviest of these daughter nuclei (the lanthanides, atomic numbers $57 < \mathrm{Z} < 71$), the resulting atoms have complex electronic structures with with open f shells. These valence shells have millions of bound-bound transitions, leading to incredibly large opacities $> 10\times$ that of iron, and shifting the emissivity of the resulting ejecta from the UV and optical to the IR (Kasen et al. 2013).

Because this ejecta is radioactive and optically thick, photons cannot escape until the mean density has dropped due to relativistic expansion. For simplicity, if we assume a spherically symmetric ejecta, the optical depth of the ejecta, τ, can be parameterized as,

$$\tau \approx \rho\kappa R = \frac{3M\kappa}{4\pi R^2} \tag{1.3}$$

Where R is the radius of the ejecta of mass M moving at velocity v, and κ is the material's opacity. For a 1D random walk from the center of the ejecta to the surface, after N unit-steps a photon is displaced $\sqrt{N}$ steps. The total number of mean-free paths to the surface is $\sim \tau$, so the cumulative scatterings to reach the surface of the ejecta is τ^2. Therefore the diffusion timescale is roughly,

$$\begin{aligned} t_{\rm diff} &\approx \tau^2 \frac{R}{c\tau} = \tau \frac{R}{c} && (1.4)\\ &= \frac{R}{c}\frac{3M\kappa}{4\pi R^2} && (1.5)\\ &= \frac{3M\kappa}{4\pi c v t} && (1.6) \end{aligned}$$

where we set $R = vt$. This photon diffusion time scale sets the time of peak for the light curve, when the time t equals t_{diff} (Arnett et al. 1989; Metzger 2017),

$$t_{\rm peak} \equiv \left(\frac{3M\kappa}{4\pi\beta v c}\right)^{1/2} \tag{1.7}$$

Here β is a parameter that depends on the exact density profile of the ejecta (usually set by

simulations, and in the case of Metzger (2019), $\beta = 3$). If we wrap up $\frac{3}{4\pi\beta}$ in a convenience parameter B ≈ 0.08, Equation 1.7 becomes,

$$t_{\rm peak} \approx \left(\frac{BM\kappa}{vc}\right)^{1/2} \tag{1.8}$$

$$= 1.5 \text{ days} \left(\frac{M}{10^{-2}M_\odot}\right)^{1/2} \left(\frac{v}{0.1c}\right)^{-1/2} \left(\frac{\kappa}{1 \text{ cm}^2\text{g}^{-1}}\right)^{-1/2} \tag{1.9}$$

If we consider a case where opacity is close to that of iron, i.e., very little to no r-process elements mixed in the ejecta, Table 1 of Tanaka et al. (2020) maps a $Y_e = 0.4$ to a $\kappa \approx 1$ cm^2 g^{-1}, which by Equation 1.9 yields a $t_{\rm peak} = \sim$1 day. On the other hand, for an r-process enriched ejecta, the same author maps a $Y_e = 0.15$ to a $\kappa \approx 30$ cm^2 g^{-1}, which yields a $t_{\rm peak} = \sim$8.5 days. Therefore, the composition (i.e., opacity) of the material has a direct impact on the time scale for the KN to evolve — with heavier elements generating a more slowly evolving KN.

To understand the peak luminosity of such a transient, we need two other pieces of information, the radius, $R_{\rm peak}$, and the temperature, $T_{\rm peak}$, which must satisfy,

$$L_{\rm peak} = 4\pi R_{\rm peak}^2 \sigma_B T_{\rm peak}^4 \tag{1.10}$$

where σ_B is the Boltzmann constant. We can derive R_{peak} from t_{peak} by,

$$
\begin{aligned}
R_{\rm peak} &\approx v t_{\rm peak} && (1.11)\\
&= \left(\frac{BM\kappa v}{c}\right)^{1/2} && (1.12)\\
&\approx 1.3\times10^{15}\ {\rm cm}\left(\frac{\kappa}{10\ {\rm cm^2\ g^{-1}}}\right)^{1/2}\left(\frac{v}{0.1c}\right)^{1/2}\left(\frac{M}{10^{-2}M_\odot}\right)^{1/2} && (1.13)
\end{aligned}
$$

which is valid so long that the β-decay timescale is $<<$ than $t_{\rm peak}$. Because the radioactive heating given in Equation 1.2 is always *decreasing*, the luminosity of the KN should be maximized around $t_{\rm peak}$,

$$Q_{\rm peak} \approx \dot{Q}(t_{\rm peak}) \times t_{\rm peak}. \tag{1.14}$$

$L_{\rm peak}$ is therefore,

$$L_{\rm peak} \approx \frac{Q_{\rm peak}}{t_{\rm peak}}, \tag{1.15}$$

and by Equation 1.10, $T_{\rm peak}$ is,

$$T_{\rm peak} \approx \left(\frac{L_{\rm peak}}{4\pi R_{\rm peak}^2 \sigma_B}\right)^{1/4} \tag{1.16}$$

More ejecta mass provides more matter to radioactively decay, and therefore results in a more luminous transient; however, from simulations, the amount of r-process rich ejecta estimated from such a merger, $\sim$0.01–0.1 $M_\odot$ (Rosswog et al. 2013; Metzger 2019), sets the peak luminosity scale roughly $10^3\times$ that of a classical nova, leading to the name "kilonova" coined

by Metzger et al. (2010). For this same ejecta, values of κ can range from that of iron (order unity) to 10s of $\mathrm{cm}^2\ \mathrm{g}^{-1}$, resulting in a t_{peak} of up to a week. Taken together, when we search for such a counterpart, we must be fast enough to catch a kilonova before it fades, yet image deeply enough to catch these intrinsically faint counterparts (see Figure 1.1 for a numerical comparison of these effects). Intensive work studying the effect of line opacities of r-process elements have shown their opacities remain nearly 2 orders of magnitude greater than iron-group elements out to mid-infrared wavelengths (Kasen et al. 2013). Therefore, a robust prediction is that KN also tend to be red in the optical, and potentially brighter in the infrared.

By fitting observed light curves to KN models, the key physical parameters of ejecta mass, ejecta velocity, and ejecta opacity can be ascertained. And, given the above physical properties of KNe, it is clear that finding these objects will be difficult — they are relatively faint, they are red, and they are quickly evolving. Fortunately, they are also massive, and in the seconds before merger emit gravitational radiation that can be detected by the ground-based GW detectors.

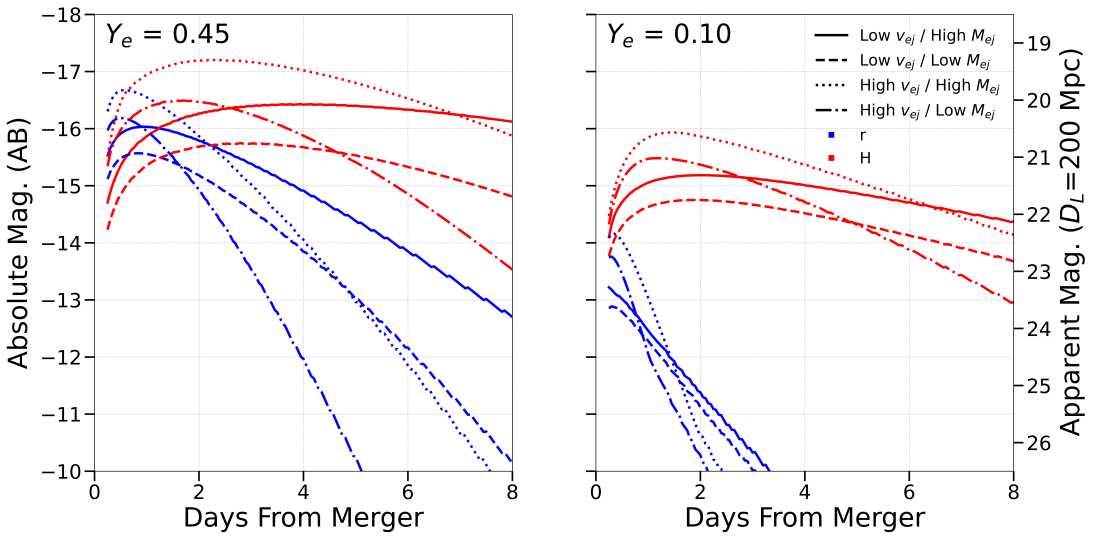

Figure 1.1 A comparison of KNe models from Metzger (2019). *Left* Models for a $Y_e = 0.45$ which correspond to a $\kappa \approx 1$. Ejecta mass, M_{ej}, and ejecta velocity, v_{ej}, are varied between "low" and "high" values (0.33/0.09 $M_\odot$ and 0.31/0.09 c). Low v_{ej} / high M_{ej} is given by a solid line, low v_{ej} / low M_{ej} by a dashed line, high v_{ej} / high M_{ej} by a dotted line, and high v_{ej} / low M_{ej} by a dot-dash line. Curves in blue are in the optical r-band, and in curves in red are in the infrared H-band. The effect of Equation 1.7 can be seen in the light curves: faster v_{ej} leads to earlier peaks, while larger M_{ej} leads to later peaks. In accordance with Equation 1.15, larger M_{ej} also lead to more luminous peaks. *Right* The same family of light curves, but for models with $Y_e = 0.10$ which correspond to a $\kappa > 30$. These light curves demonstrate the effect of lanthanide opacities dramatically shifting emission to the red. For the LVK's fourth observing run, BNS mergers could be detected (at low signal-to-noise) out to a distance of 200 megaparsecs, and for red KNe, detecting such a transient may be difficult or impossible in optical bands after a few days. In both cases, these models demonstrate that the best chances of finding a KN are within a week of GW merger.

1.4 A Discovery in Gravity and Light

On 2017 August 17, the Laser Interferometer Gravitational-wave Observatory (LIGO) and the Virgo interferometer detected gravitational waves emanating from a binary neutron star merger, GW170817 in its second observing run. Nearly simultaneously, the *Fermi* and INTEGRAL telescopes detected a gamma-ray transient, GRB 170817A. 10.9 hours after the gravitational wave trigger, our team, the One-Meter Two Hemispheres (1M2H) Collaboration,

using my original work, discovered a transient and fading optical source, Swope Supernova Survey 2017a (SSS17a; also known as AT 2017gfo), coincident with GW170817. SSS17a is located in NGC 4993, an S0 galaxy at a distance of 40 megaparsecs.

This discovery is covered in detail in Chapter 3, but represents a watershed moment and the start of a new era of MMA. Combining GW and EM data from this one event, fulfilled many of the promises of MMA, and significant advances were made in NS demographics (Abbott et al. 2019a), the origin of heavy elements (Kilpatrick et al. 2017), the nuclear EOS (Capano et al. 2020), the nature of gravity (Baker et al. 2017), and measurement of the Hubble constant, H_0 (Abbott et al. 2017d).

The key to rapidly localizing the KN with the relatively small field of view Swope telescope (~ 0.25 deg^2), was to search by pointing at luminous galaxies within the high-probability localization (Kanner et al. 2012; Gehrels et al. 2016) versus "tiling" the entire localization region. This strategy was particularly well suited because the event was so close and galaxy catalogs are highly complete at this distance — however this will not be the case with distant mergers.

This discovery is also a case study in how technical preparedness enables MMA. Because our team was so well-prepared, not only did we discover SSS17a on our 9th planned image, we obtained the only spectrum within 24 hours of the GW trigger (Shappee et al. 2017). Surprisingly, SSS17a's early-time light curve contained a "blue" component (i.e., a component with $\kappa \approx 0.08$ cm^2 g^{-1}) suggesting that there was a portion of its ejecta that had a very low opacity, and therefore a relative lack of lanthanides (Drout et al. 2017; Kilpatrick et al. 2017). Despite the success at relatively rapidly localizing the KN and measuring this early component, even earlier opportunities to observe it were missed. During that crucial time, there were no

constraints on its early bolometric light curve leading to open questions about whether it was powered by radioactive decay or some other cooling mechanism (Arcavi 2018).

Since this discovery the race has been on to find another KN, however as GW detectors have made steady advances in their sensitivity and range, EM follow-up to GW sources has commensurately become more challenging. This trend, coupled with are localization areas and faint and quickly fading transients, makes these same techniques less effective for finding EM counterparts. Therefore, if we are to answer some of the questions that SSS17a posed, and if we are to fully understand the BNS channel for r-process enrichment, we need to find the next KN and that requires new tools, algorithms, and techniques.

1.5 Outline of this work

Unlocking the promise of real-time transient science requires a multi-pronged approach. In Chapter 2, I present my work on building a next-generation software platform `YSE-PZ` , which is designed to efficiently organize and prioritize an ever increasing volume of transient data being generated by a variety of public and private sources. `YSE-PZ` seeks to empower human decision making, allowing users to construct ad hoc queries to select scientifically interesting samples of transients, to automatically annotate transients if they meet certain criteria, and to streamline requests for follow-up. This software is also portable, open-source, and well-documented, and is provided for free for the entire astronomical community to use and to modify to their own needs. In Chapter 3, I present the discovery of the first optical counterpart to a gravitational wave source, which has set the stage for a new era in multimessenger astronomy. The observation of a binary neutron star merger in gravitational waves, a short gamma ray burst ~ 2 seconds

later, and a kilonova in UVOIR $\sim$ 11 hours after the merger, has confirmed that neutron stars do merge, that they are prolific astrophysical sites for the r-process, and that neutron star mergers are associated with short gamma ray bursts. Because these kilonovae fade and change colors so rapidly, and because these events hold so much promise for uncovering fundamental physics, this discovery has set the stage for a new paradigm in transient astronomy — one that requires the coordination of global networks of telescopes and optimization of observing strategies, all in real-time. In Chapter 4, I present a new tool called `Teglon` in the context of the search for the second-ever binary neutron star merger detected in gravitational waves, GW190425. `Teglon` builds upon the success of the first discovery by extending our strategies to take into account galaxy catalog completeness and can agnostically combine community data products into the most comprehensive limits on likely electromagnetic counterpart models. I have also built `Teglon` to be open-source, portable, and available to the entire community.

Chapter 2

YSE-PZ: A Transient Survey Management Platform that Empowers the Human-in-the-Loop

2.1 Introduction

Time-domain astronomy is experiencing an exponentially growing rate of astrophysical transient discoveries, with 24,634 transients reported in 2021[2] compared to only 909 in 2011[3], a 27-fold increase. The rising discovery rate is driven by the transition from narrow-field galaxy-targeted surveys (e.g., the Lick Observatory Supernova Search; Filippenko et al. 2001) to wide-field time-domain surveys, including the All-Sky Automated Survey for Supernovae (ASAS-SN; Shappee et al. 2014), the Asteroid Terrestrial-impact Last Alert System (ATLAS; Tonry et al.

[2] https://www.wis-tns.org/stats-maps
[3] https://www.rochesterastronomy.org/sn2011/snstats.html

2018), the Catalina Real-Time Transient Survey (CSS; Drake et al. 2009), the Gaia Photometric Science Alerts (Hodgkin et al. 2021), the Mobile Astronomical System of Telescope-Robots (MASTER; Lipunov et al. 2010), the Panoramic Survey Telescope and Rapid Response (Pan-STARRS) Survey for Transients (PSST; Huber et al. 2015), the Palomar Transient Factory (PTF; Law et al. 2009), the Nearby Supernova Factory (SNfactory; Aldering et al. 2002), the Young Supernova Experiment (YSE; Jones et al. 2021), and the Zwicky Transient Facility (ZTF; Bellm et al. 2019a). The discovery rate is expected to further increase by an additional order of magnitude with the start of survey operations for the Vera Rubin Observatory's Legacy Survey of Space and Time (LSST; LSST Science Collaboration et al. 2009b).

The corresponding continually expanding volume of data introduces new challenges for data management, transient triage, and follow-up decisions. On average, ∼50 new transients are reported to the International Astronomical Union (IAU) every day, with several times more *potential* transients identified in survey data. Without efficient ways to sift data streams to find targets of interest, we risk missing novel transient events or failing to discover them in time to obtain follow-up observations before they have changed or faded. Furthermore, collating data from multiple transient surveys and extant archives is essential to have the most complete dataset for making decisions in real time.

For supernovae (SNe), follow-up observations obtained within the first hours to days after explosion are particularly critical since they probe the outermost layers of a SN's ejecta and its progenitor star (e.g., Soderberg et al. 2008; Modjaz et al. 2009; Ofek et al. 2010; Bloom et al. 2012; Tinyanont et al. 2022), illuminate close-in circumstellar material before it is overrun (e.g., Sternberg et al. 2011; Gal-Yam et al. 2014; Jacobson-Galán et al. 2020a, 2022a; Terreran et al.

2022), and reveal details of the progenitor system (e.g., Marion et al. 2016; Hosseinzadeh et al. 2017; Dimitriadis et al. 2019a; Shappee et al. 2019; Miller et al. 2020). While wide-field high-cadence observations are critical to discover SNe at early times, additional tools are necessary to *identify* these SNe before this phase has passed.

Methods of managing transient data have evolved from transient survey websites in the 1990s and early 2000s, such as the Rochester Astronomy Supernova webpage[4] that started in 1996. This website collated information about every SN, including its location, brightness, and host galaxy. Many SNe had finding charts, providing critical information not transmitted through International Astronomical Union (IAU) Circulars and Central Bureau Electronic Telegrams (CBETs; Green 2002), which at the time were the primary way for professional astronomers to communicate about SNe in (near) real-time. In 1997, the introduction of The Astronomer's Telegram (ATel) constituted the next advance in the real-time distribution of astronomical information. For the first time, human editors were not required to vet information prior to distribution, instead maximizing the reliability of posted information by restricting those who could post to the service to professional astronomers whose identities were verified prior to activation (Rutledge 1998). By front-loading verification and relying on automation to send notices, the lag between posting and receiving information was reduced to $\sim$1 second. As IAU reporting diminished throughout the early 2000s, ATels continue to be an important source of real-time transient information, while the Rochester webpage became the de facto database for all transients until the IAU system was overhauled and the new Transient Name Server (TNS)[5] re-engaged the community in 2016.

[4] https://www.rochesterastronomy.org/supernova.html.
[5] https://www.wis-tns.org/.

Internal webpages for high-redshift SN cosmology surveys including Equation of State: SupErNovae trace Cosmic Expansion (ESSENCE; Smith et al. 2002), SDSS-II (Frieman et al. 2008), SNFactory (Aldering et al. 2002), and the Supernova Legacy Survey (SNLS; Astier et al. 2006) also tracked SN discoveries from their specific surveys and included important information about the sources, such as brightness and classification. Over time, these systems became more sophisticated. Several systems began to splinter into "search" services and "target and observation managers" (TOMs). The former would be a database of potential transients from the survey (e.g., Goldstein et al. 2015), while the latter would consist of "promoted" transients of interest that could be monitored. For several surveys, these internal tools were significantly more powerful than the Rochester webpage or the CBETs, causing further fragmentation.

In recent years, the community has tackled the challenge of effectively and efficiently acting on modern transient data streams by breaking the problem into two complementary layers: so-called data "brokers," which broadly replicate the search features of previous surveys but with several enhancements; and continually improved TOMs. Data brokers parse the data from raw transient alert streams by filtering on criteria such as those that reduce false positive detections or indicate likely SNe.Many brokers have focused on the ZTF alert stream, which has ∼1 million alerts a night, including MARS (Brown et al. 2013a), ANTARES (Saha et al. 2014), Lasair (Smith & Gray 2018), AMPEL (Nordin et al. 2019), Fink (Möller et al. 2021), ALeRCE (Förster et al. 2021), and Pitt-Google[6]. Nearly all of these brokers will also be tasked with serving the Rubin Observatory alert stream — which will provide ∼10 million alerts per night — as it begins operation in the mid-2020s. Some of these brokers include features such as

[6] https://github.com/mwvgroup/Pitt-Google-Broker.

value-added galaxy catalog cross-matching (e.g., via `GHOST`; Gagliano et al. 2021). Several also give the user flexibility to define their own transient filtering criteria and execute queries on a flexibly-defined set of data attributes.

After transient data have been parsed by a broker, a TOM will store the pre-processed alert packages and facilitate follow-up observations or identify samples for subsequent scientific analyses. Some recently developed TOMs include the Palomar Transient Factory (PTF) Follow-up Marshal (Rau et al. 2009), the RoboNet Microlensing System (Tsapras et al. 2009), the PESSTO Marshall (Smartt et al. 2015), the Supernova Exchange (SNeX; Howell & Global Supernova Project 2017), SkyPortal (van der Walt et al. 2019), the TOM-toolkit (Street et al. 2018), the Global Relay of Observatories Watching Transients Happen (GROWTH) Marshall (Kasliwal et al. 2019), the Transient Science Server (Smith et al. 2020), the SNAD ZTF object viewer (Malanchev et al. 2022), and the NASA Exoplanet Follow-Up Portal (ExoFOP)[7].

These tools are usually designed for a single survey and purpose, with common limitations including a focus on specific data sets or surveys, the lack of access to the public, and a closed source codebase. The notable exceptions are SkyPortal and the TOM Toolkit, which are open-source[8,9], extensible, and customizable TOM frameworks. Because these TOMs are so flexible, they require some customization to get started, and in the case of the TOM Toolkit, it and all its dependencies must also be directly installed by a user. Despite the rich combination of brokers and TOMs currently available, it remains challenging to leverage data into effective decision-making. Automated tools that retrieve metadata, fit models, or classify transients often need human intervention to robustly identify transients of interest and select scientifically

[7] https://exofop.ipac.caltech.edu/tess/
[8] https://github.com/TOMToolkit
[9] https://skyportal.io/

interesting samples of transients.

Here, we present YSE-PZ, a transient survey management platform. YSE-PZ combines traditional TOM functions, e.g., data collation and resource management, with interfaces that allow users to define Python-based queries, SQL queries, and metadata tags, to filter on data *within* YSE-PZ's internal database like a data broker. This unique combination addresses the ongoing challenges in real-time decision-making by empowering the human-in-the-loop to flexibly identify key properties, trends, and relationships within a TOM environment. YSE-PZ is open-source, publicly available software that synthesizes astronomical data from existing public transient surveys and combines these data with private data, user-uploaded data, archival metadata, and output from value-added services. YSE-PZ synthesizes and displays these distinct data in an easy-to-digest format, provides a variety of query and filtering tools that supports filtering these data streams into scientific samples of interest, and enhances real-time decision-making. YSE-PZ does not require any package dependencies other than Docker to be installed on the target machine (see Section 4.7), and an instance of the application can be installed and run quickly within an identical environment in which it was developed. Finally, YSE-PZ includes a framework for planning and executing follow-up observations, allowing transients to be managed from discovery through to analysis of follow-up data.

In Section 2.2 we give an overview of the YSE-PZ platform. In Section 2.3 we discuss our generic transient workflow, and in Section 2.4 we share use cases that illustrate how YSE-PZ supports a diverse set of user and science requirements. We discuss YSE-PZ in the context of a broader open science ecosystem in Section 4.7. We conclude in Section 2.6.

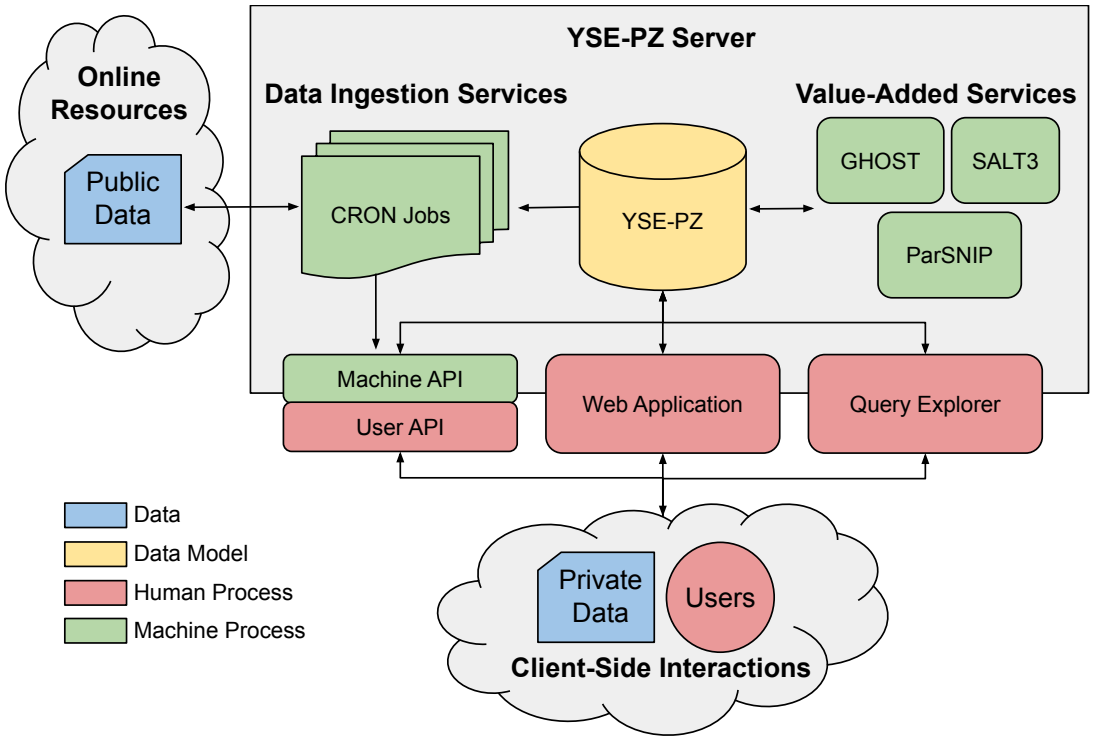

Figure 2.1 Architectural schematic of `YSE-PZ`. Arrows show the flow of data between entities. All entities within the rectangle are housed on the UCSC Transients Team's research server. Users of `YSE-PZ` are associated with a survey and interact with the application via the API, web user interface (UI), and the Query Explorer. CRON Jobs, which are run server-side, request data from external public services. These data are posted back to the application via the API. Value-added services including host-galaxy association via `GHOST` (Gagliano et al. 2021), transient classification via `ParSNIP` (Boone 2021), and transient light-curve fitting with `SALT3` (Kenworthy et al. 2021) are also run server-side and populate the `YSE-PZ` database with auxiliary transient information.

2.2 YSE-PZ

`YSE-PZ` is a new transient survey management platform that takes an object-oriented approach to modeling the full workflow of transient observations. This workflow is built on `YSE-PZ`'s data model, which defines relationships between the transient, its data, and metadata. This model also defines the types of data that `YSE-PZ` can store and upon which it can act. `YSE-PZ` is also a dynamic application; it continually ingests new transients, their data and

metadata, invokes value-added services that annotate these data, and performs application-level maintenance tasks.

In this section, we will first cover YSE-PZ's data model (Section 2.2.1) and task management system (Section 2.2.3), and then we will enumerate the data (Section 2.2.4 and 2.2.5) as well as features (Section 2.2.6) enabled by these two components. We then describe how a human-in-the-loop interacts with YSE-PZ via the query engine (Section 2.2.7), front-end web application (Section 2.2.2), API (Section 2.2.8), and user groups and permissions (Section 2.2.9).

2.2.1 Data Model

YSE-PZ is a Django-based web application[10] employing a MySQL[11] backend and a Representational State Transfer (REST) compliant Application Programming Interface (API) (see Figure 2.1). To model the objects within the transient workflow, YSE-PZ uses the Django Object-Relational Mapper (ORM) framework. The ORM allows a developer to model transient properties, behaviors, and relationships within Python code rather than creating these objects directly in SQL. This developer-friendly approach makes extending the application easier.

YSE-PZ's data model is constructed to be general enough to model any transient survey data, astronomical metadata, and observational workflow. While this generality makes some queries more complex than those against a simpler data model, the advantage is that YSE-PZ can ingest any public or private astronomical data and define workflows down to the instrument configuration for follow-up requests.

Within YSE-PZ, the main objects include the transients themselves, their host galaxies,

[10] https://www.djangoproject.com/
[11] https://www.mysql.com/.

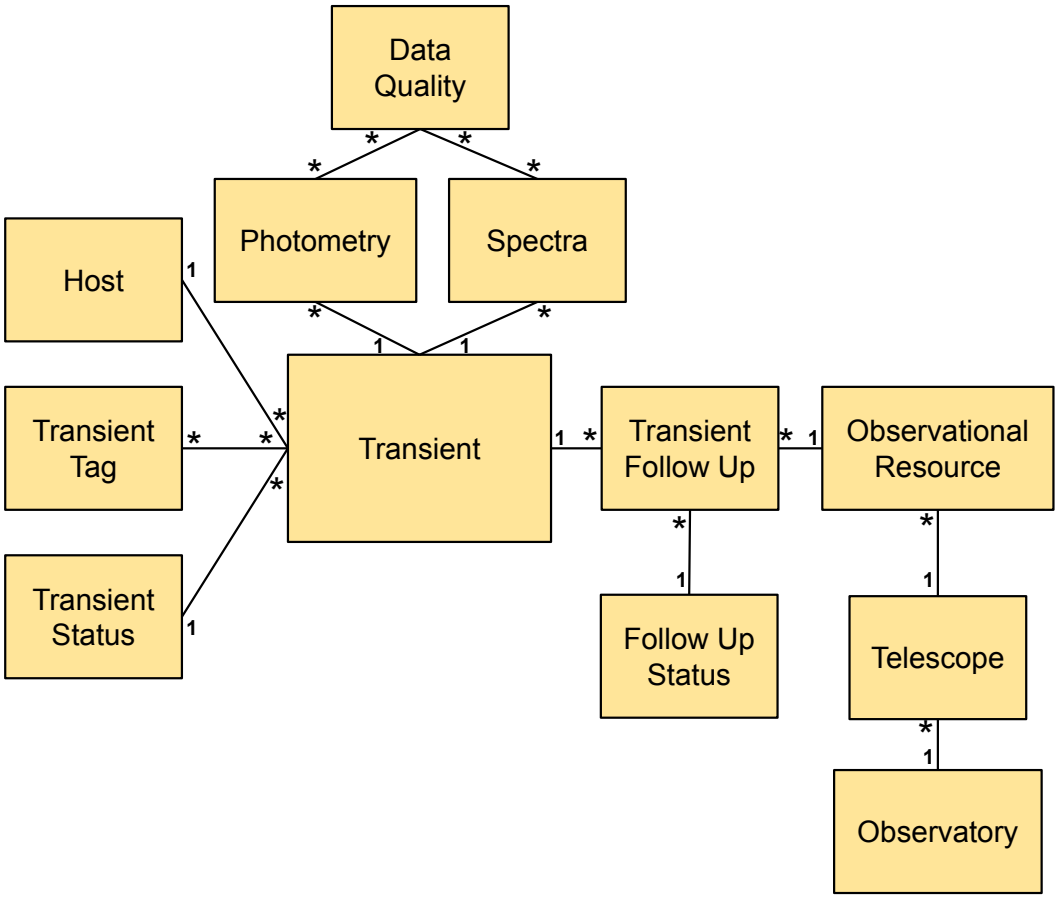

Figure 2.2 Simplified `YSE-PZ` data model. This schematic shows how a representative sample of objects within the schema are related and anchored to a transient. Lines that terminate in a "1" denote a singular relationship, while lines that terminate in a "*" denote a "many" relationship, e.g., `Transient` has a many-to-many relationship with `Transient Tag`, but a one-to-many relationship to `Photometry`. See Section 2.2.1 for an expanded discussion.

metadata, public data, private data, and auxiliary data such as observing resources and follow-up requests. `YSE-PZ` has 100 tables, for a complete listing of tables, see the `YSE-PZ` GitHub repository[12]. For brevity, we present a simplified science schema of `YSE-PZ` in Figure 2.2, conceptually focused on the central `YSE-PZ` objects. A `Transient` object is defined by its name, coordinates, and discovery date. A `Transient` object is also connected to other data and metadata objects. For example, a `Transient` has associated astronomical data objects, `Photometry` and `Spectra`, each defined by fields like flux, magnitude, bandpass, etc. A `Transient` also has an associated metadata object called `Transient Status` that stores how a given transient relates to a user's workflow (see Section 2.3).

In the case of `Photometry` and `Spectra`, a `Transient` has a "one-to-many" relationship, i.e., one transient may have many data points, but each data point is associated with only one transient. On the other hand, some object relations are "many-to-many", e.g., the `Transient-Transient Tag` relationship. The `Transient Tag` object holds a user-defined tag that can be applied to any transient, and denotes some interesting property (see Section 2.2.7). One tag may apply to many transients, and a transient may have many different tags for many different properties. These relationships are denoted in Figure 2.2.

2.2.2 Front-End Web Application

The Django ORM also powers a front-end web application in the industry-standard design pattern of the Model-View-Controller (MVC) architecture. In this paradigm, web requests are made to a controller object, which acts as a gateway that routes incoming requests to the appropriate resource, e.g., a web page or direct data download.

[12] https://github.com/davecoulter/YSE_PZ

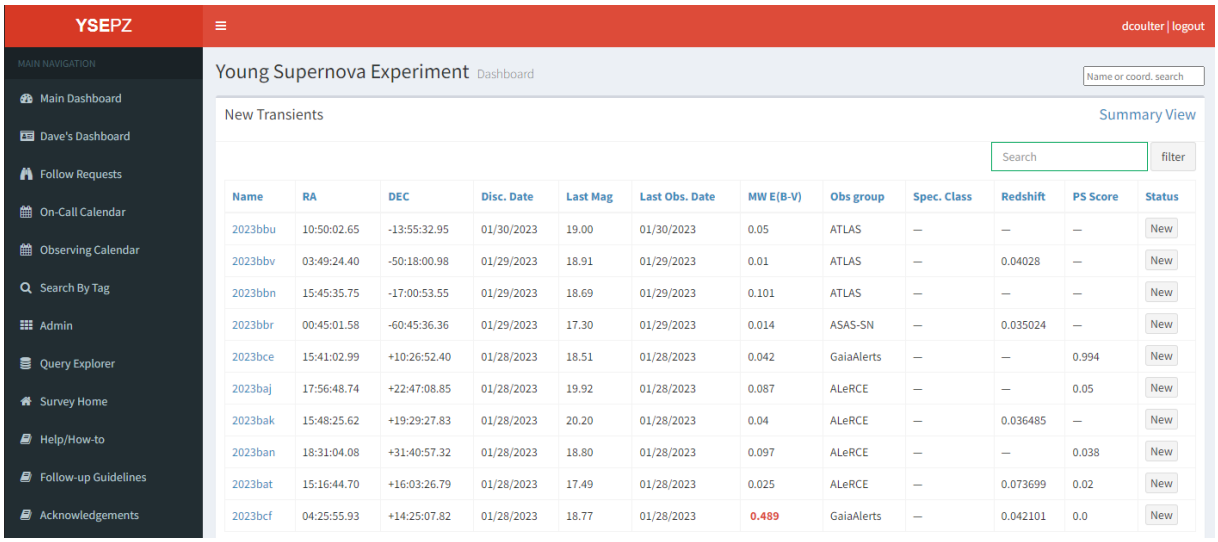

Figure 2.3 One of `YSE-PZ`'s main dashboard tables. Transients with "New" status are displayed in a searchable "New Transients" HTML table with associated summary information for each transient (see Section 2.3 for a description of how the transient statuses are used). In addition to the table shown, tables for transients grouped by other statuses ("Following", "Interesting", "Watch", "Finished Following", and "Needs Template") are available further down the dashboard. Milky Way reddening values in the "MW E(B-V)" column are automatically displayed in red when they are >0.2 mag. The left navigation bar provides easy access to the rest of `YSE-PZ`'s features and views.

Based on the requested URL, user identity, and group permission, the controller will retrieve the information of interest from the database using the Django ORM and then package these data into an object called a `model`. A `model` is a dictionary of structured data that is rendered dynamically by an HTML template, called a `view`. The final rendered HTML is what a user sees in their browser.

`YSE-PZ` accomplishes most of its front-end functionality with a series of interactive dashboards that allow data to be displayed in space-efficient, paginated tables with the ability to sort on each column displayed. Upon logging into `YSE-PZ`, a user is greeted with the main dashboard, which displays newly ingested transients from TNS into a table called "New Transients" (Figure 2.3). Below the New Transients table, there are further tables for transients with

different user-configurable statuses: *Followup Requested*, *Following*, *Interesting*, *Watch*, *Finished Following*, and *Needs Template* (see Section 2.3.1 for a description of these statuses). While these are the default statuses, it's important to note that a user is free to define any status they wish, as well as to customize the main page of the application to reflect their workflow preferences.

The front-end web application also has a left navigation bar with links to other parts of the site, including a separate web page that displays all follow-up requests made for each telescope resource, an on-call calendar which is configurable to send SMS text messages to users who want to respond to events in real time (e.g., searching for gravitational wave counterparts, see Section 2.4.4), an observation calendar (which displays configured observing resources in a calendar format, see Figure 2.8), a search utility that can query the database for transients that have been tagged with user-defined tags (see Figure 2.6), a Query Explorer[13] that allows users to flexibly create ad hoc queries against the database on any property of the data model, and an administration function exposed by Django that allows a user with administrative permissions to edit data in the database directly using a built-in, Django web form. Finally, each user has their own personal dashboard that can be configured to display transients of interest. To do this, a user writes a query to select objects using the Query Explorer, and then attaches that query to their dashboard. Users can also select from a predefined set of python-based queries for this purpose.

Transient data can then be viewed via template-generated, individual transient detail pages (see Figure 2.4). These transient detail pages are tab-based, and each tab provides different views of the data and different functions available to a user. On the main Summary tab, all

[13]The `YSE-PZ` Query Explorer is built off of the `Django SQL Explorer` https://django-sql-explorer.readthedocs.io/en/latest/

available photometry and spectroscopy that a user is permitted to view (see Section 2.2.9) is plotted via an interactive `Bokeh` JavaScript widget. Metadata and external links to archival data (e.g., NED and TNS) are shown at the top of the page, and archival Digitized Sky Survey (DSS), SDSS, Pan-STARRS, and DECam legacy survey images are shown in a section devoted to galaxy host data. On the Follow-up tab, there are resources for requesting follow-up for a transient, as well as forms to add new observational resources to the system (see Section 2.3.3. A Detailed Photometry tab provides a tabular view of all transient photometry, as well as a convenient way to download this data. *HST* and *Chandra* tabs report if archival image footprints coincide with the transient position, and a Comments tab allows users to attach free-form comments to a transient.

2.2.3 `YSE-PZ`'s Task Management System

The dynamic part of `YSE-PZ` is the configured Command Run On (CRON) job. These task runners are modular, configured for a single task, and interact with the API via `POST`s, as well as the Django ORM. The modular nature of these CRON jobs makes extending `YSE-PZ`'s functionality straightforward. In principle, CRON jobs can be run from any server and interact purely with the API to `GET` or `POST` any necessary data; however, `YSE-PZ` largely uses CRON jobs that are constructed to directly query the database on the `YSE-PZ` back-end for computational efficiency. These server-side CRON jobs are constructed and organized using the `django-cron`[14] module, which allows users to create and configure CRON jobs using Django's application settings file, as well as providing access to the ORM's representation of `YSE-PZ` objects.

[14] https://django-cron.readthedocs.io/en/latest/.

YSE-PZ uses CRON jobs to continually ingest public data (see Section 2.2.4), retrieve archival and metadata (see Section 2.2.5), and invoke value-added services (see Section 2.2.6). CRON jobs are also used by YSE-PZ to perform various other tasks, including annotating data (e.g., flagging transients in *TESS* fields), scheduling YSE survey observations (see Section 2.4), and performing daily database back-ups. For more on how YSE-PZ is used by specific collaborations, see Section 2.4.

2.2.4 Sources of Publicly Available Transient Data

YSE-PZ retrieves and stores data from the following sources via CRON jobs:

1. **The Transient Name Server** (TNS[15]). TNS is the official reporting service for the International Astronomical Union (IAU) that provides available photometry and spectroscopic classifications for publicly reported transients discovered by the community. The CRON job that handles TNS data ingestion queries their API every five minutes to ingest newly discovered transients or to update previously ingested transients with new photometric, spectroscopic, and classification data. Because existing transients may be updated within TNS, this CRON job has logic to prevent transients from being duplicated[16].

2. **ATLAS forced photometry** (Tonry et al. 2018; Smith et al. 2020; Shingles et al. 2021). The Asteroid Terrestrial-impact Last Alert System (ATLAS) surveys the visible sky in the "cyan" and "orange" bands ("cyan" is approximately the same as $g + r$; "orange" is

[15] https://www.wis-tns.org/.

[16] We require that any new transient be greater than 2 arcsec from the position of an existing transient *or* be discovered more than a year earlier/later. While this still allows for duplicate events in rare cases with an exceptionally long reporting/discovery lag time, it generally mitigates against missing new transients at a coincident location in the same galaxy; an occurrence that could be particularly scientifically interesting.

approximately $r + i$) every two days. `YSE-PZ` automatically queries the public ATLAS forced photometry data once per day for a subset of transients of interest that we identify using a `YSE-PZ` query.

3. **Gaia photometric science alerts** (Hodgkin et al. 2021). Gaia observes the whole sky with a spatially heterogeneous cadence (e.g., Boubert et al. 2020) but typically makes successive pairs of observations separated by 2-4 weeks in the G-band (a broad white-light filter). Gaia alerts are queried hourly.

4. **PSST via the Transient Science Server**. PSST surveys ∼14,000 square degrees of sky in the i and w (white light that is roughly $g + r + i$) bands at an irregular cadence with 1-4 return visits of each field scheduled within 15 days of the first observation. PSST photometry is ingested every two hours.

5. ***Swift* optical and ultraviolet photometry via the *Swift* quick-look data archive**[17]. Once per hour, we query all previously unanalyzed *Swift* imaging for overlap with transients in YSE-PZ and perform forced aperture photometry on these images at the locations of the transients.

6. **The Young Supernova Experiment via the Transient Science Server** (Smith et al. 2020). The Young Supernova Experiment surveys ∼1500 square degrees of sky at any time to a depth of $gri \simeq 21.5$ mag, and $z \simeq 20.5$ mag, with a three-day cadence. YSE data are vetted using the Transient Science Server, and transients deemed both "good" and "possible" (indicating a transient that may be real) by the YSE team are ingested to

[17] https://swift.gsfc.nasa.gov/cgi-bin/sdc/ql

YSE-PZ every 30 minutes.

7. **ZTF via the ANTARES Astronomical Time-domain Event Broker** (Matheson et al. 2021). ZTF is currently surveying the northern extragalactic sky on a two-day cadence, with publicly available photometry in the *gr* bands. We use the ANTARES client to ingest ZTF photometry for transients reported to TNS; ZTF photometry is queried upon ingestion of the TNS transients and updated twice per day for transients not flagged as "Ignore" (see Section 2.3.1 for status labels). Forced photometry can be manually requested via the ZTF forced photometry service[18] and is uploaded within approximately one hour, depending on the speed of the ZTF forced photometry server[19].

8. Additional photometric and spectroscopic data from individual collaboration follow-up surveys currently using YSE-PZ are continually added to YSE-PZ via private scripts that POST their data through the API. This workflow demonstrates the extensibility of the platform, as well as an example of API-only CRONs referred to in Section 2.2.3.

While TNS is the primary source for transients to enter the YSE-PZ database, transients can also be directly discovered by collaborations that use YSE-PZ, and ingested via the API (see the YSE Case Study in Section 2.4). In these cases, YSE-PZ's API has been designed to match existing transients by position, taking a union of the final objects' properties while setting the default transient name to the IAU name from TNS.

[18] https://ztfweb.ipac.caltech.edu/cgi-bin/requestForcedPhotometry.cgi

[19] Previously, YSE-PZ used the "Make Alerts Really Simple" (MARS, from the Las Cumbres Observatory; Brown et al. 2013a) broker to perform the same task, but this service has been taken offline by Las Cumbres Observatory at the end of January 2023.

2.2.5 Sources of Archival data

Archival data and metadata, including static-sky data and forced photometry, are retrieved for each transient using several public catalogs and image servers. Cutout archival images at the location of each transient are displayed using image servers from SDSS (York et al. 2000), Pan-STARRS (Chambers et al. 2016), the Digitized Sky Survey via Aladin (Bonnarel et al. 2000; Boch & Fernique 2014), and the DESI Legacy Imaging Surveys (Dey et al. 2019). These data are not stored in the database but can be easily downloaded by the user. Any available *HST*, *Spitzer*, and *Chandra* data are included on each transient detail page (see Section 2.2.2), and the existence of such archival data from each source is stored in the `Transient` table to facilitate queries on transients with archival space-based data. Archival Pan-STARRS1 catalog data (Chambers et al. 2016; Flewelling et al. 2020) are also used to determine whether a given transient coincides with a point source (Tachibana & Miller 2018), indicating a likely flaring star.

2.2.6 Value-added services

`YSE-PZ` uses `GHOST` (Gagliano et al. 2021) to match each transient to its most likely host galaxy; `GHOST` also measures a photometric redshift via `Eazy PhotoZ` (Aleo et al. 2022) for each host galaxy from a fully connected, feed-forward neural network algorithm trained on Pan-STARRS data. `YSE-PZ` also includes interactive plots and plot-anlysis tools. Plotting is performed with Bokeh (Bokeh Development Team 2018), and interactive `SALT3` fitting is performed (Kenworthy et al. 2021) using `sncosmo` (Barbary et al. 2022). These routines estimate light-curve parameters and approximate times of maximum light under the assumption that a

transient is a Type Ia SN. Finder charts for each transient can be generated automatically on request from the user, and airmass plots, target rise/set times, and moon angle information from `astroplan` (Morris et al. 2018) are also included (see Section 2.3.3 for a discussion on these features).

2.2.7 Queries & Tags

All data in the `YSE-PZ` database can be queried either through the REST API or the Query Explorer. These queries are custom written to meet a user or survey group's transient science goals. The most-used queries are those that identify recently discovered transients with rising light curves and queries that find unclassified transients in a magnitude- or volume-limited sample. For example, the Keck Infrared Transient Survey (Section 2.4), uses these queries to identify subsets of transients for follow-up observations. The results of these queries can be displayed on a user's personal dashboard page or accessed programmatically through the web application itself (see Appendix 2.8 for example queries).

While queries provide a powerful way to interrogate the data, `YSE-PZ` also enables users to apply customizable tags to objects (see Figure 2.6). Tags are user-defined, text strings that can be attached as metadata to transients. These tags empower users to create arbitrary groupings of transients, and provides an additional property upon which queries can be built. Tags can also be applied automatically to facilitate data triage from certain sources or science programs.

2.2.8 Application Programming Interface

YSE-PZ contains two Application Programming Interfaces (APIs), a machine-facing API used to ingest or extract raw data from an authorized user into YSE-PZ's tables directly, and a user-facing API that allows users to upload data to YSE-PZ through a system of checks and flags that allow data to be created, modified, and deleted while checking for logical inconsistencies and errors like incomplete data, incorrectly formatted data, or duplication. The machine API is provided by a Django plugin module called the Django REST framework, while the user API was written by YSE-PZ developers. Both APIs are easily extensible and continue to evolve as needed to accommodate new science requirements.

2.2.9 User Groups and Permissions

YSE-PZ has been designed to support multiple surveys and collaborations within a single instance. This is accomplished through user-defined "user groups" that can be associated with astronomical data uploaded through the API. Access to these data (both download and display) is then controlled by adding or removing users to specific groups. An example of this data access control is shown in Figure 2.5.

While user groups offer reasonable control over access to private data, we recommend that if data security is a concern, a separate instance of YSE-PZ be deployed. In this scenario, there is no possibility of one group gaining access to another group's data on the same system. See Section 4.7 for a discussion on YSE-PZ deployment approaches.

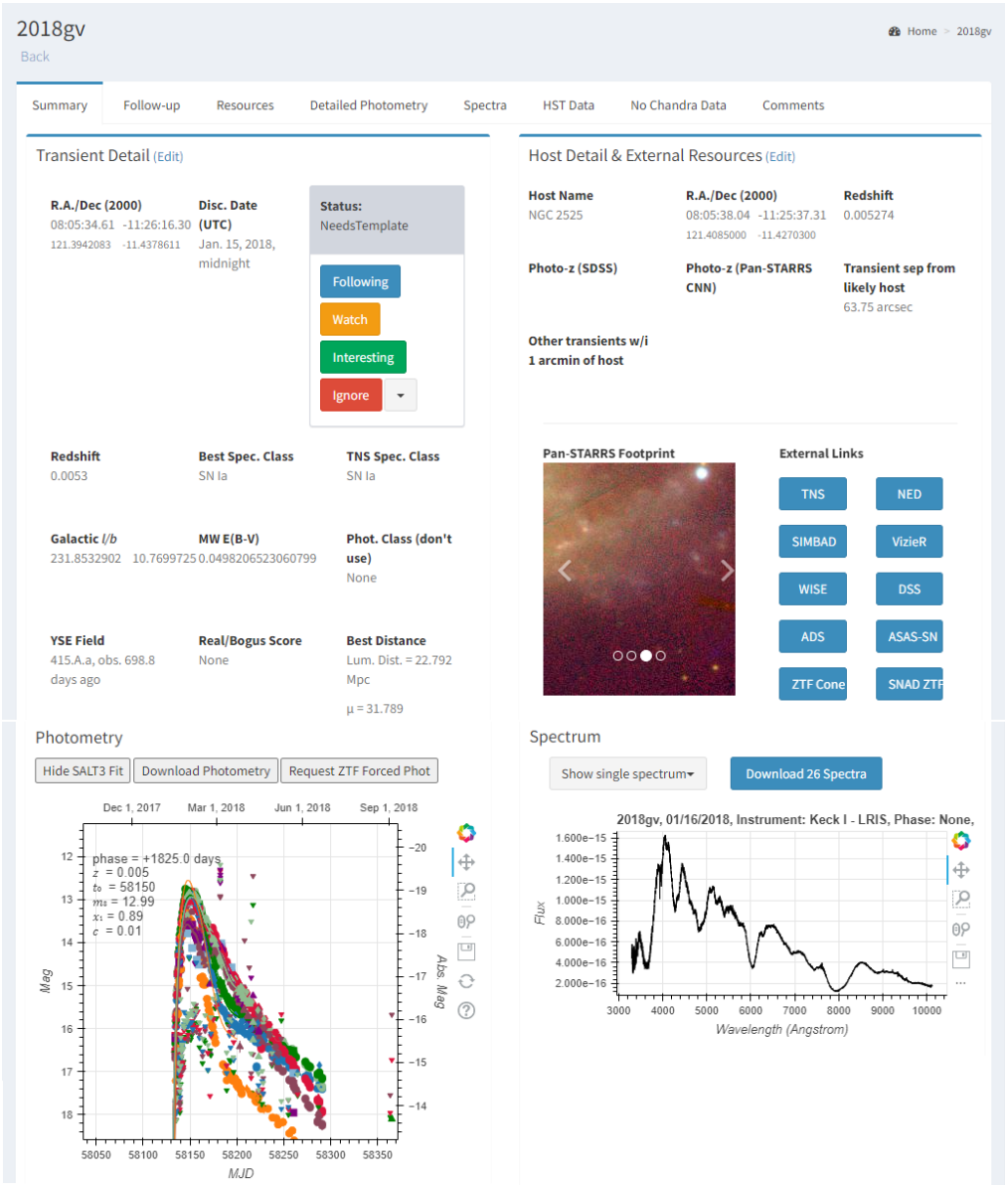

Figure 2.4 Subset of elements of a `YSE-PZ` transient detail page, which shows information related to a single transient (in this case, SN 2018gv; Yang et al. 2020). The top-left quadrant enumerates the basic positional information for a transient and includes controls for changing a transient's status. The top-right quadrant focuses on host-galaxy data, including postage stamp images and links to external web services. In the bottom-left quadrant, there is an interactive Bokeh (Bokeh Development Team 2018) light curve plot showing photometric data for the transient. Three buttons allow the user to toggle a SALT3 (Kenworthy et al. 2021) model light curve fit to the photometry, download the photometric data, and request forced photometry for the transient from ZTF. The bottom-right quadrant shows an interactive plot of the spectral data for the transient, with buttons allowing users to display all spectra for the transient simultaneously or individually, and to download the data. From left to right, the tabs along the top panel include the Summary tab, which is currently selected in this Figure, tools for requesting follow-up observations for the given transient (the Follow-up tab), a list of observation resources that can be triggered for a transient with per-observatory airmass plots and a utility to generate finder charts (the Resources tab), a downloadable, tablular-formatted list of all photometry on a transient (the Detailed Photometry tab), detailed spectral information (the Spectra tab; not currently implemented), *Hubble Space Telescope* and *Chandra X-ray Observatory* archival data at the transient location, respectively, and a text area allowing users to attach free-form comments to a transient (Comments tab).

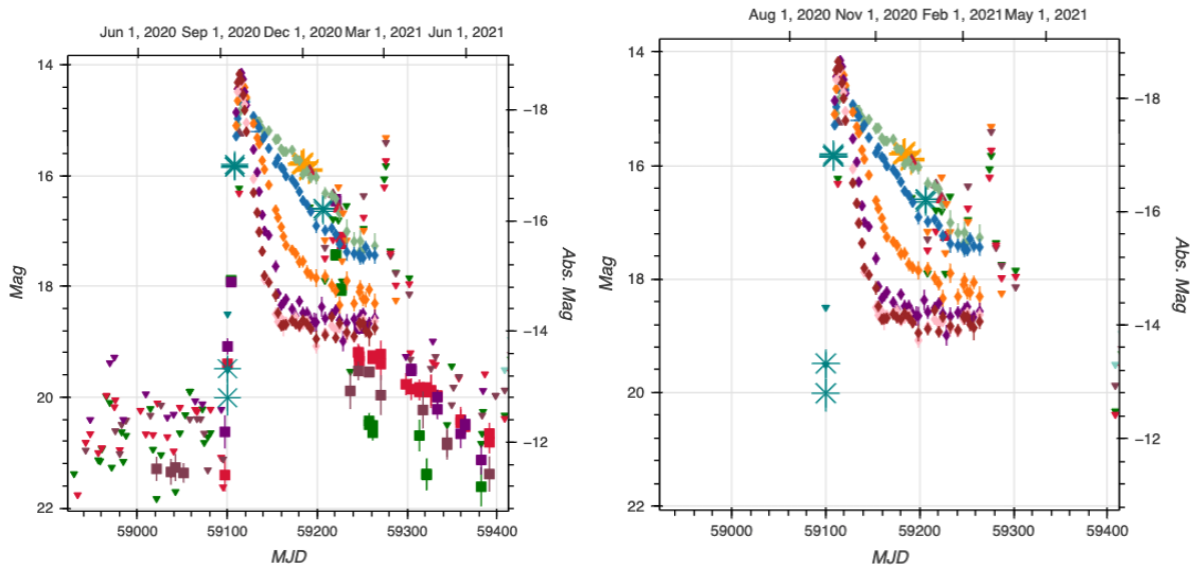

Figure 2.5 An example (SN 2020tlf; Jacobson-Galán et al. 2022a) of the effect of `YSE-PZ` group permissions as shown through the displayed light-curve plot on an object's detail page. Detections and non-detections are displayed as different symbols including an error bar (although sometimes smaller than the plotted symbol) and downward-pointing triangles, respectively. Left: The full light curve of a transient as seen by a user with membership in all `YSE-PZ` groups. Right: A view of the same transient from the perspective of a user with membership in only a select number of `YSE-PZ` groups. In this case, users with access to YSE Pan-STARRS data (displayed as squares) could see the pre-explosion brightening described by Jacobson-Galán et al. (2022a), while those without access to those private data would not see this behavior. Since there is a gap in the YSE Pan-STARRS data not long after explosion, the combination of multiple data sources were critical to follow the evolution of SN 2020tlf.

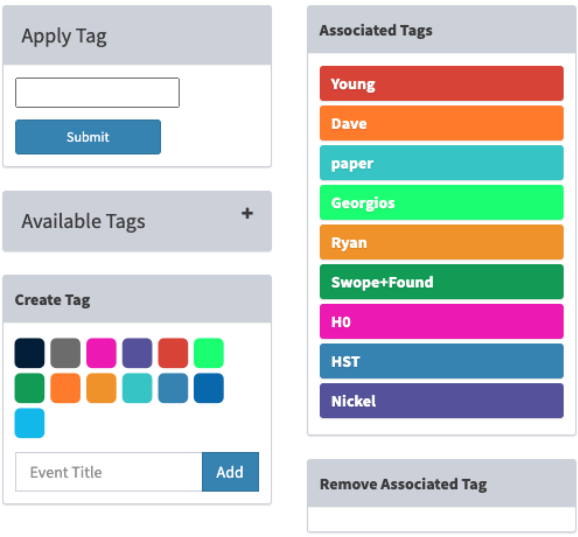

Figure 2.6 The `YSE-PZ` transient tag form, which is located on each transient detail page. This form allows a user to associate arbitrary tags with a given transient, allowing configurable and user-customized tracking.

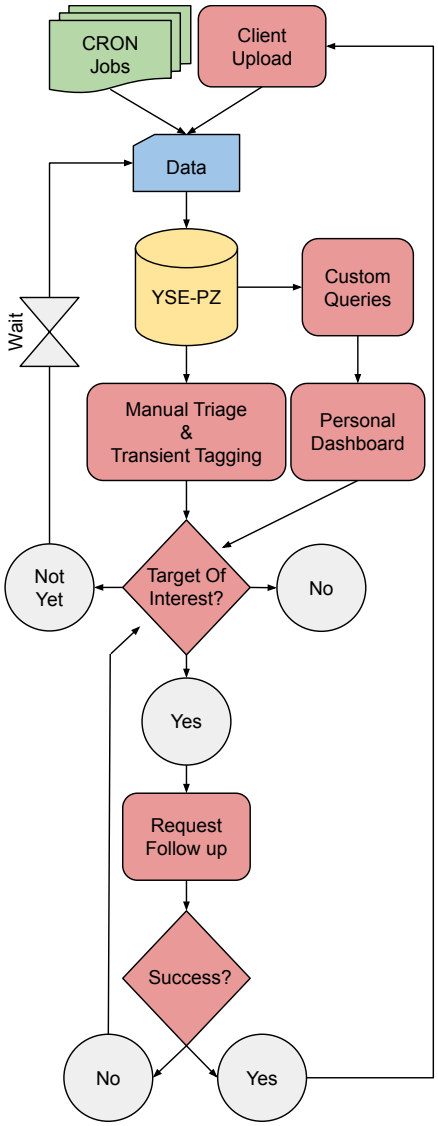

Figure 2.7 Data flow within `YSE-PZ`. New transients, as well as their scientific data and metadata, are ingested into `YSE-PZ` and then triaged by a human either through manually screening new transients, tagging individual transients, or by writing queries based on various transient properties. After identifying interesting candidates, follow-up requests can be made and subsequent data can be uploaded.

Figure 2.8 Observing calendar showing all scheduled resources for a given month. Both the observing asset and Principal investigator (PI) for each resource is shown.

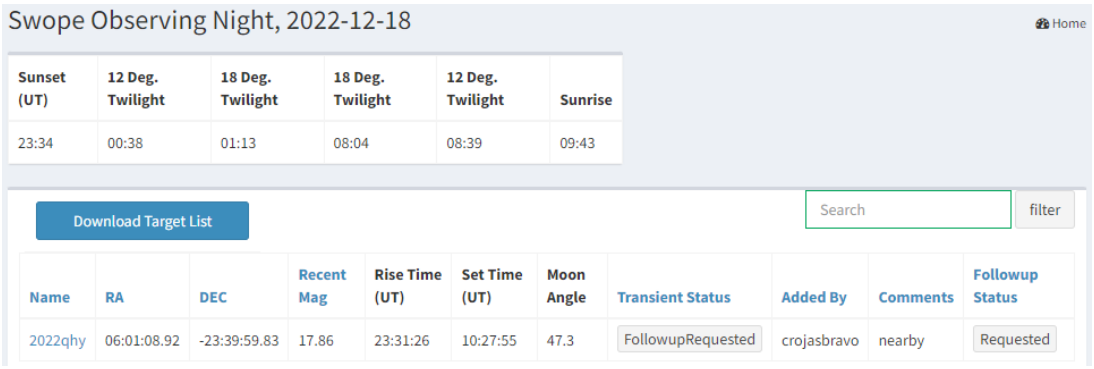

Figure 2.9 Partial screenshot of an observing night schedule webpage showing requested transient targets and their associated basic information and status. Users are able to download the target list from this page.

2.3 The YSE-PZ transient Lifecyle

In this section we detail how `YSE-PZ` is used to triage, analyze, and obtain follow-up data for transients. Figure 2.7 shows an overview of the entire life cycle of an ingested transient in `YSE-PZ`. We explain each aspect of the workflow below.

2.3.1 Manual Triage and Transient Tagging

When transients are first ingested into `YSE-PZ`, they are given a status of *New*. As described in Section 2.2.2, users interact with these transients through a series of dashboards (e.g., Figure 2.3) with sortable, paginated tables that include redshifts, classifications, Milky Way reddening, last reported magnitudes, and discovery dates for each transient. These provide the user an overview of the data and allow them to easily view and triage new transients.

Though the exact status categories can be altered by the user, our team has found the following status categories to be useful:

- *New*: a transient that has just entered the system.
- *Watch*: a transient that could be potentially interesting, but hasn't risen to the level of being targeted for follow-up observations. Most transients are triaged into this category from their initial status of *New*.
- *Interesting*: an interesting transient that may be targeted for follow-up observations.
- *Followup Requested*: A transient for which a follow-up request has been made.
- *Following*: a transient actively being followed. At least one observation is necessary for this status to be used.

- *Needs Template*: a transient with completed follow-up observations, but that require template observations (i.e., observations with no transient flux).
- *Followup Finished*: a transient whose dedicated follow-up observations have been completed, including template observations.
- *Ignore*: a transient where no follow-up observations have been obtained and none are expected to be obtained.

These statuses are broadly descriptive enough to organize, track, and act on most transients as they flow through the follow-up process. However, where these metadata states are insufficient, users can create or assign custom metadata tags (see Section 2.2.7 and Figure 2.6) to create new groupings of transients.

2.3.2 Custom Queries and Personal Dashboards

In addition to screening new transients as they are ingested, users can write and execute custom queries as described in Section 2.2.7, and attach them to their personal dashboards as described at the end of Section 2.2.2. These queries can be written to select transients based on interesting properties or trends in the data (e.g., rising light curves, close distances, etc.), and offer ways to define scientific samples for further study.

2.3.3 Requesting and Planning Follow-up Observations

Each transient within `YSE-PZ` has an automatically generated transient detail page (see Figure 2.4). Within the detail page, users can navigate to the Follow-up tab which has a series of simple forms to record follow-up requests and to add new observational resources to the system.

If a user adds a new resource to the system, it is displayed in a calendar format on the Observing Calendar (see Figure 2.8).

To manually request follow-up observations a user can link one of these resources to the transient. Finder charts and airmass plots, which can be used to vet the feasibility of a follow-up request, are available on the transient's detail page under the Resources tab. Once a request is made, a history of all requests, and their statuses (e.g., *Requested*, *Successful*, *Failed*, etc.), are displayed. All requested transients for an observing night are accessible through the observing calendar, and are displayed with interactive dashboards (see Figure 2.9. Each row of this dashboard contains comments left for the observer and a link back to the transient detail page.

In addition to manual follow-up, it is also possible to automatically trigger follow-up observations with `YSE-PZ`. As mentioned in Section 2.2.4, API-only CRON jobs can be written to select transients that have been tagged using `YSE-PZ`'s tagging system (see Section 2.2.7 and Figure 2.6), and then external scripts can query the `YSE-PZ` database via the API to select all tagged transients and submit them directly to queue-based networks like Las Cumbres Observatory's API (Brown et al. 2013a; Nation et al. 2022) and NOIRLab's AEON network (Briceño & Astronomical Event Observatory Network 2020). An enhancement to allow `YSE-PZ` to submit observation requests directly to observatory APIs is forthcoming.

2.3.4 Uploading Follow-up Data

Finally, after transient follow-up observations have been successfully obtained a user can upload the data to `YSE-PZ` via the API. These uploads can be manual or can be automated

by adding an upload stage to an independent data reduction CRON jobs. Once uploaded, the transient detail page can be refreshed to display this new data, and a user closes the workflow loop shown in Figure 2.7.

2.4 Case Studies

The transient life cycle described above is only one of many possible use cases for `YSE-PZ`. Below, we outline several additional collaboration-level workflows that `YSE-PZ`'s flexible platform enables.

2.4.1 Photometric and Spectroscopic Monitoring of Interesting Transients by the UC Santa Cruz Transient Team

Although transient sample sizes are growing exponentially, some of the most interesting questions related to transients are best answered by observing individual, extraordinary events. The University of California, Santa Cruz Transient Team spectroscopically and photometrically monitors dozens of interesting transients simultaneously. We use `YSE-PZ` to triage all discovered transients, track interesting objects, and schedule follow-up observations. Here, we describe in detail how The University of California Santa Cruz Transient Team uses the triage tags outlined in Section 2.3.1.

After a transient discovery is announced on TNS, `YSE-PZ` will ingest the basic information for this transient. Initially, `YSE-PZ` labels its transient status as *New*, and it will appear on the dashboard under this category. Some transients are immediately deemed uninteresting (e.g., old discoveries, high Galactic reddening, coincident with a known quasar or Galactic star) and

their status is changed to *Ignore*. A particularly interesting transient will either immediately have follow-up observations requested, at which point its status is automatically updated to *Followup Requested*, or its status is changed to *Interesting*. The remaining transients have their statuses changed to *Watch*.

For the interesting transients, we will usually manually request forced photometry to obtain those data on a timescale faster than the automatic CRON job would provide. Additional examination of data on the detail page will often result in applying user-defined tags (e.g., "Young").

Either through the main dashboard, where one can sort transients based on the time the last data was obtained, or through the personal dashboard, users can easily monitor these interesting events separately from the bulk of active transients. During normal monitoring or in preparation for a classical observing night, we will use ad hoc queries displayed on the personal dashboard and queries from user-defined tags to select targets for follow-up observations. Some ad hoc queries include targets rising quickly and those with new data within a day of discovery. Useful user-defined tags include "personal" tags for individual users (usually marked by their name) and qualitative information such as those objects for which a paper will be written. We also examine observation requests from previous observing nights to request observations of additional objects.

Once an object has targeted follow-up observations, its status is changed to *Following*. When we no longer expect to obtain more data for an object, we change the status to either *Followup Finished* or *Needs Template* depending on if a template observation is required.

If no targeted follow-up data is obtained and there is no expectation to obtain data,

a transient's status is changed to *Ignore*. Changing the status not only reduces the number of objects that we are actively monitoring, but also stops now unnecessary CRON jobs executing for that transient (see Section 2.2.3).

The bulk of transients have a life cycle where their status changes from *New* to *Watch* to *Ignore*; this occurs for thousands of transients each year and requires tools to reduce the workload. Using a query (Section 2.2.7), we select all transients with a *Watch* status and where there has been no new data in three weeks. These objects are good candidates for changing their status to *Ignore* without examining each object in detail. We have a separate query to look at the subset of those objects that might have interesting aspects such as being particularly bright at the time of the last observation. After manually examining the potentially interesting objects (and possibly updating their status to Interesting), we can change all remaining object from the initial query to *Ignore* in bulk.

2.4.2 Survey Planning and Operations with YSE

As introduced Section 2.2.4, YSE is a time-domain survey that combines proprietary Pan-STARRS and other public imaging data, along with significant follow-up resources, to survey a large fraction of the high Galactic latitude Northern sky. For an overview of the survey's goals and operations, see Jones et al. (2021) and Aleo et al. (2022).

`YSE-PZ` is an integral part of YSE operations, supporting the survey's transient discovery process and organizing its transient follow-up observations. YSE relies on complex interfaces between reduced data products (via the Image Processing Pipeline (IPP); Magnier et al. 2020), initial transient vetting (via the Transient Science Server; Smith et al. 2020), and data synthesis

via YSE-PZ. Critically, YSE-PZ enables a "secondary" vetting of potential YSE SN discoveries. The YSE survey cannot easily rule out whether a possible transient is a moving object, such as an asteroid, because YSE has just five minutes between its observations in two different filters. To mitigate this, YSE uploads unverified transients into YSE-PZ to cross-match against other public surveys.

Vetting these candidates is made easy through YSE-PZ because observers can search both publicly reported transients at the possible SN location, as well as trigger jobs to download ZTF or ATLAS forced photometry. Furthermore, because YSE-PZ collates a variety of archival data, such as host galaxy redshifts, team members can use queries to identify an approximate luminosity for a given transient and help the team decide if the transient is likely real and/or young. YSE-PZ also uses its record of YSE fields and YSE observations to see if publicly reported transients have YSE imaging at their location and then queries forced photometry at that location via the Pan-STARRS IPP. IPP forced photometry is then added to the YSE database, and can result in recent non-detections that alert the team that a transient is young. By combining these public, private, and archival data streams, YSE-PZ is perfect for this secondary transient vetting, confirming new transient discoveries, and optimizing follow-up decisions.

YSE-PZ is also used to schedule and monitor the status of every Pan-STARRS observation for YSE. YSE-PZ stores each Pan-STARRS observation in a `Survey Observation` model, which includes the status of each observation (i.e., if it was successfully observed) and important characteristics of each observation (e.g., seeing, airmass, etc.). Team members access these metadata from the API to ensure that future observations meet the desired cadence, filter choice, and moon avoidance criteria, while allowing individual survey images to be inspected

for photometric quality. The `YSE-PZ` data model also contains survey-specific objects to model YSE's Survey Minimum Schedulable Blocks (SMSBs), which are logical groupings of survey field centers. These MSBs enable YSE observers to dynamically manipulate and schedule groups of survey fields, e.g., to image nearby SNe or galaxies of interest, through an interactive tool within `YSE-PZ`.

2.4.3 Query Driven Follow-up Observations with the Keck Infrared Transient Survey

The Keck Infrared Transient Survey (KITS) is a NASA Key Strategic Mission Support program (Programs 2022A_N125, 2022B_N169, 2023A_N040; PI Foley) to usethe Near-InfraRed Echellette Spectrometer (NIRES; Wilson et al. 2004) on the 10-m Keck 2 telescope to obtain, and subsequently make publicly accessible, near-infrared (NIR) spectra of all types of astrophysical transients (Tinyanont et al. in prep.). Specifically, KITS emphasizes observations of rare transients, as well as obtaining spectra of more common transients at epochs with poor existing NIR spectroscopic data, which will be crucial to interpreting *James Webb Space Telescope* (*JWST*; Gardner et al. 2006) data of transients at higher redshift. These data will also play a key role in planning future time-domain surveys with the upcoming *Nancy Grace Roman Space Telescope* (Spergel et al. 2015).

To accomplish these goals, KITS selects targets with three different criteria powered by queries written with `YSE-PZ`'s Query Explorer: (1) a survey of SNe Ia at phases with poor NIR spectroscopic observations and/or with large host extinction, (2) a magnitude-limited survey of all transients with $r < 17$ mag, and (3) a volume-limited survey of transients with $z < 0.01$. For

examples of these queries, see Appendix 2.8.

In addition to defining samples of transients to observe, the KITS team tags every KITS object with a custom tag. This tag makes querying `YSE-PZ` for all KITS objects simple, and facilitates tracking the progress of the overall survey, generating survey statistics, producing analysis plots, and planning which are observations are needed to maximize the science goals of the survey.

2.4.4 Making Decisions with Archival, Meta, and Astronomical Data Sources with the Swope Supernova Survey

The Swope Supernova Survey is a time-domain survey that uses the 1-m Swope telescope at Las Campanas Observatory to obtain *uBVgri* follow-up imaging of SNe and other astrophysical transients (Kilpatrick et al. 2018a). A chief aim of the SSS is to produce a sample of low-redshift, cosmologically useful Type Ia SNe akin to the Foundation Supernova Survey (Foley et al. 2018). `YSE-PZ` is used to check if the host of the transient is nearby, whether that host has coincident *Chandra* and *HST* imaging, and ZTF and ATLAS forced photometry can constrain whether the transient is young. For transients that are assumed to be SN Ias, the `SALT3` function on the transient detail page (see Section 2.2.6) can assess important SN properties like phase and luminosity.

Since 2017, SSS has also searched for the electromagnetic (EM) counterparts to gravitational wave (GW) sources, as a part of the One-Meter Two-Hemispheres (Coulter et al. 2017b; Kilpatrick et al. 2017) and the Gravity Collective (Kilpatrick et al. 2021) collaborations. During a search, astronomers do not know when and where to search for EM counterparts beforehand;

this information is published by the LIGO-Virgo-KAGRA Collaboration in the form of localization maps. These maps can range in size from tens to thousands of square degrees on the sky (Abbott et al. 2020a), and depending on the area, subsequent searches can identify hundreds to thousands of transient candidates a night.

It is crucial to locate EM counterparts to GW sources as quickly as possible to understand their physics because they change on fast timescales (Arcavi 2018). This urgency means that most candidates can not be vetted before they are reported, so they are reported through messaging networks like the Gamma-Ray Coordinates Network (GCN; Barthelmy et al. 1995) and ATels instead of the TNS. While `YSE-PZ` does not yet support directly ingesting ATels or GCNs (i.e., at the time of writing neither service guarantees machine-parsable content), combining information from ATels and GCNS with `YSE-PZ`'s archival information is key in committing follow-up resources to these candidates. `YSE-PZ` can be queried to find spatially coincident pre-existing transients, candidates can be matched to a host galaxy to estimate their luminosity distance, and forced photometry can reveal pre-GW event variability. If no viable counterparts are discovered, spatial and temporal queries can retrieve all reported candidates (and their data) potentially associated with GW event to rule them out, allowing for search data to be interpreted as upper limits on counterpart models.

2.5 `YSE-PZ` and NASA's Open-Source Science Initiative

Astronomy faces challenges beyond those solely posed by exponentially increasing data volumes. Large transient surveys and their associated software infrastructure (e.g., Alert brokers, TOMs, value-added services) are often sprawling, complex, and difficult to install and

run. To ensure that large collaborations run efficiently, that effort is not duplicated, and to broaden collaboration within the scientific community, the *way* that software is built is increasingly as important as the software itself. In the face of these challenges, NASA has made a long-term commitment to the Open-Source Science Initiative (OSSI)[20] with the aim of implementing NASA's Strategy for Data Management and Computing for Groundbreaking Science[21]. At the heart of the OSSI are four core principles: transparency, accessibility, inclusivity, and reproducibility.

While `YSE-PZ` was conceived and the initial framework was built before NASA had adopted the OSSI, our initial goals, structures, and development approaches were aligned with its principles, and we now use the OSSI as a guide for our work moving forward. For instance, `YSE-PZ` is transparent; its code base is open source and developed on Github[22] under a GNU General Public License v3.0. `YSE-PZ` is inclusive; extensive documentation describing how to use the web interface and API, and how to install and develop against the application is hosted by `readthedocs`[23]. `YSE-PZ` is accessible and reproducible; its environment has been virtualized and the orchestration between its required services is scripted using `Docker` (Merkel 2014). Enabled by `Docker`, all of `YSE-PZ`'s required components, i.e., its database, operating systems, standard and customized packages, etc., are packaged together in a way to make the application installable with only a handful of commands[24].

Beyond the portability that virtualization affords, having `YSE-PZ` constructed this way

[20] https://science.nasa.gov/open-science-overview.
[21] https://science.nasa.gov/science-red/s3fs-public/atoms/files/SDMWG%20Strategy_Final.pdf
[22] https://github.com/davecoulter.
[23] https://yse-pz.readthedocs.io/en/latest/.
[24] See https://yse-pz.readthedocs.io/en/latest/install.html for instructions on how to run `YSE-PZ` using `Docker`.

removes the installation and deployment barrier that can stifle new developers from contributing to the project. To increase the transparency and reproducibility of all contributions to `YSE-PZ`, code is merged through pull requests that include both peer reviews and several automatic and manual tests. Promoting code this way builds confidence that code is of high quality, does what it is intended to do, protects our production environment from preventable bugs, and enhances the application's stability.

2.6 Conclusions

In this work we describe the features and implementation of `YSE-PZ`, a transient survey management platform. We highlight our model of the machine-human workflow used to accumulate data on scientifically interesting transients, and discuss how the design and development operations used to develop `YSE-PZ` are aligned with the OSSI.

There are currently more than a dozen public, active data sources for transient data. `YSE-PZ` leverages this public transient survey data by combining sources such as ZTF, ATLAS, ASAS-SN, and *Gaia* that make the entire photometric transient light curve public, with other surveys that publish the first photometric epochs or provide public transient spectra. `YSE-PZ` then combines these data with private transient data obtained by individual transient science teams.

`YSE-PZ` has a flexible data model for ingesting these data from multiple data streams. Data can be easily displayed, queried or downloaded, and the database itself can be queried to search for transients that display certain photometric or spectroscopic behavior. Archival data and contextual metadata is combined as part of the data model to allow a holistic picture of

each transient.

YSE-PZ also addresses the challenge of optimizing follow-up resources for a given transient science case. Transient science goals require incorporating considerations such as the brightness of the transient versus the size of the follow-up telescope, the latency of follow-up observations compared to how fast the transient is evolving, the wavelength/frequency range at which the transient must be observed, and the priority of the observations versus the time remaining in a given program.

YSE-PZ addresses these issues by storing each available observing resource and observing night in the database, and listing all facilities in a calendar page. Users request transients for follow-up observations, with comments that motivate the follow-up request, and the list of transients requested for each resource and observing night are listed on an observing night's detail page.

Although YSE-PZ's design is effective for the data volume from current ongoing surveys, the next generation of surveys will present new challenges for our transient management workflows. Current data streams are small enough to allow the human-machine workflow shown in Figure 2.7 to select individual scientifically interesting transients to be followed (see Appendix 2.9 for a list of publications enabled by YSE-PZ) and to build scientifically useful samples of transients (e.g., Aleo et al. 2022). However, for next-generation, high-volume transient surveys such as LSST which will find $\sim 10^5$ bone fide transients a year — at least a 6-fold increase in our current data ingestion rate — further workflow automation will become increasingly necessary. Despite this, humans will always be more flexible than static code routines and may always be required to manually request follow-up observations on high-value resources; therefore, this next

generation of infrastructure needs to do more than simply remove "human bottlenecks" and instead empower humans to make effective decisions in real-time.

Realizing the scientific potential of these data will require a corresponding investment in infrastructure tools. `YSE-PZ` is poised to meet these challenges by incorporating new technologies that will reconcile automation with human-centered decision-making processes. New messaging protocols like Apache Kafka[25] are moving the astronomical community toward a "publication-subscription" model of information ingestion; `YSE-PZ` will adapt and enable users to subscribe to alert streams from any astronomical data broker with customizable filters. `YSE-PZ` will also continue to take advantage of machine-learning advances in automatic transient classification (e.g., Boone 2021; Burhanudin & Maund 2022), and could be combined with citizen science platforms (e.g., Christy et al. 2022; Zevin et al. 2017) to further empower, or even *optimize* (e.g., Walmsley et al. 2020; Wright et al. 2017), robust human-in-the-loop decision making at scale.

2.7 Software Utilized

`Docker` (Merkel 2014), `NumPy` (Harris et al. 2020), `Bokeh` (Bokeh Development Team 2018), `Astropy` (Astropy Collaboration et al. 2013a, 2018), `Django` (`https://www.djangoproject.com`), `sncosmo` (Barbary et al. 2022), `MySQL` (`https://www.mysql.com/`, `YSE-PZ` (Coulter et al. 2022), `GHOST` (Gagliano et al. 2021), `healpy` (Zonca et al. 2019a; Górski et al. 2005a), `abseil-py` (`https://github.com/abseil/abseil-py`), `ALeRCE` (Förster et al. 2021), `antares-client` (`https://gitlab.com/nsf-noirlab/csdc/antares/client`), `asn1crypto` (`https://github.com/wbond/`

[25] `https://kafka.apache.org/`

asn1crypto), astroplan (Morris et al. 2018), Astroquery (Ginsburg et al. 2019), astunparse (https://github.com/simonpercivall/astunparse), attrs (https://github.com/python-attrs/attrs), backcall (https://github.com/takluyver/backcall), beautifulsoup (https://www.crummy.com/software/BeautifulSoup/), bson (https://github.com/py-bson/bson), cachetools(https://github.com/tkem/cachetools/), casjobs (https://github.com/dfm/casjobs), certifi(https://github.com/certifi/python-certifi), cffi (https://cffi.readthedocs.io/en/latest/), chardet (https://github.com/chardet/chardet), click (https://github.com/pallets/click/), confluent-kafka (https://github.com/confluentinc/confluent-kafka-python), coreapi (https://github.com/core-api/python-client/), cryptography (https://github.com/pyca/cryptography), matplotlib (Hunter 2007), cython (https://github.com/cython/cython), dustmaps (Green 2018a), extinction (https://github.com/kbarbary/extinction), flatbuffers (https://github.com/google/flatbuffers), gast (https://github.com/serge-sans-paille/gast/), google-auth (https://github.com/googleapis/google-auth-library-python), google-pasta (https://github.com/google/pasta), grpc (https://github.com/grpc/grpc) hdf5/h5py (The HDF Group 1997), html5lib (https://github.com/html5lib/html5lib-python), httpie (https://github.com/httpie/httpie), inda (https://github.com/kjd/idna), imbalanced-learn (https://github.com/scikit-learn-contrib/imbalanced-learn), iminuit (Dembinski et al. 2022), importlib_metadata (https://github.com/python/importlib_metadata) iniconfig (https://github.com/pytest-dev/iniconfig), ipython (https://github.com/ipython/ipython), itypes (https://github.com/PavanTatikonda/itypes), jedi (https://github.com/davidhalter/jedi), jeepney (https://gitlab.com/takluyver/jeepney), jinja (https://github.com/

pallets/jinja/), joblib (https://github.com/joblib/joblib, joypy (https://github.com/leotac/joypy), keras (Chollet & others 2018), keyring (https://github.com/jaraco/keyring), kiwisolver (https://github.com/nucleic/kiwi), lxml (https://lxml.de/), markdown (https://github.com/Python-Markdown/markdown), markupsafe (https://github.com/pallets/markupsafe/), marshmallow (https://github.com/marshmallow-code/marshmallow), marshmallow-jsonapi, (https://github.com/marshmallow-code/marshmallow-jsonapi), mimeparse (https://code.google.com/archive/p/mimeparse/), mpld3 (https://github.com/mpld3/mpld3), mysqlclient (https://github.com/PyMySQL/mysqlclient), oauthlib (https://github.com/oauthlib/oauthlib), opt_einsum (Smith & Gray 2018), optional_django (https://github.com/markfinger/optional-django), packaging (https://github.com/pypa/packaging), pandas (Team 2022), parso (https://github.com/davidhalter/parso), pexpect (https://github.com/pexpect/pexpect), photutils (Bradley et al. 2022), pickleshare (https://github.com/pickleshare/pickleshare), pillow (Van Kemenade et al. 2022), pluggy (https://github.com/pytest-dev/pluggy), progressbar2 (https://github.com/WoLpH/python-progressbar), prompt-toolkit (https://github.com/prompt-toolkit/python-prompt-toolkit), protobuf (https://github.com/protocolbuffers/protobuf), ptyprocess (https://github.com/pexpect/ptyprocess), py (https://github.com/pytest-dev/py), pyans1 (https://github.com/etingof/pyasn1), pycparser (https://github.com/eliben/pycparser), pyerfa (Van Kerkwijk 2021), pygments (https://github.com/pygments/pygments), pyparsing (https://github.com/pyparsing/pyparsing/), pytest (https://github.com/pytest-dev/pytest/), dateutil (https://github.com/dateutil/dateutil), python-utils (https://github.com/WoLpH/python-utils), pytz (https://pythonhosted.org/pytz/), PyVo (Graham et al. 2014), pyyaml (https://github.

com/yaml/pyyaml), requests (https://github.com/psf/requests), request-mock (https://github.com/jamielennox/requests-mock), requests-oathlib (https://github.com/requests/requests-oauthlib), rfpimp (https://github.com/parrt/random-forest-importances), rsa (https://github.com/sybrenstuvel/python-rsa), sklearn (Pedregosa et al. 2011), SciPy (Virtanen et al. 2020), seaborn (Waskom 2021), secretstorage (https://github.com/mitya57/secretstorage),sfdmap (https://github.com/kbarbary/sfdmap), six (https://github.com/benjaminp/six), sqlparse (https://github.com/andialbrecht/sqlparse), tensorflow (Abadi et al. 2016), termcolor (https://github.com/termcolor/termcolor), threadpoolclt (https://github.com/joblib/threadpoolctl), toml (https://github.com/uiri/toml), tornad (https://github.com/tornadoweb/tornado), traitlets (https://github.com/ipython/traitlets), typegaurd (https://github.com/agronholm/typeguard), typing_extensions (https://github.com/python/typing_extensions), unicodecsv (https://github.com/jdunck/python-unicodecsv), uritemplate (https://github.com/python-hyper/uritemplate), urllib3 (https://github.com/urllib3/urllib3), wcwidth (https://github.com/jquast/wcwidth), webencodings (https://github.com/gsnedders/python-webencodings), werkzeug (https://github.com/pallets/werkzeug), wget (https://pypi.org/project/wget/), wrapt (https://github.com/GrahamDumpleton/wrapt), zipp (https://github.com/jaraco/zipp), zope.interface (https://github.com/zopefoundation/zope.interface), asgiref (https://github.com/django/asgiref/), zoneinfo (https://github.com/pganssle/zoneinfo), auditlog (https://github.com/gmware/auditlog), gunicorn (https://github.com/benoitc/gunicorn), tendo (https://github.com/pycontribs/tendo), opencv-python (https://github.com/opencv/opencv-python), aladin-lite (Bonnarel et al. 2000; Boch & Fernique 2014) Eazy PhotoZ (Gagliano et al. 2021; Aleo et al. 2022)

2.8 Example database queries

This section contains example queries which can be run from the `MySQL Explorer` interface by a user and shows how transients of interest can be selected. A more extensive list of query examples can be found in `YSE-PZ`'s documentation.[26]

2.8.1 Selecting volume-limited and recently discovered SNe Ia

The query below selects SNe Ia discovered within the last 356 days with either a transient or host redshift < 0.03. The names of the transients meeting this criteria are returned in descending order of their discovery date. In the query below `disc_date` is the transient discovery data, `photo_z` is the host photometric redshift, and `TNS_spec_class` is the spectroscopic classification from the transient name server.

```
SELECT
    DISTINCT transient.name, transient.disc_date
FROM YSE_App_transient transient
LEFT JOIN YSE_App_host host ON host.id = transient.host_id
WHERE
    (transient.redshift OR host.redshift OR host.photo_z) IS NOT NULL
    AND COALESCE(transient.redshift, host.redshift, host.photo_z) <= 0.03
    AND DATEDIFF(curdate(),transient.disc_date) < 365
    AND transient.TNS_spec_class LIKE '%Ia%'
ORDER BY
    transient.disc_date DESC;
```

2.8.2 Selecting new southern and unclassified transients

The query below selects the names of new transients which are spectroscopically unclassified (`TNS_spec_class is NULL`), in the southern sky (`dec`$<= -30$), have a flux signal-to-noise of 2 (`flux/flux_err >= 2`), a magnitude error < 1.0 (`mag_err < 1.0`), and the current day to

[26] https://yse-pz.readthedocs.io/en/latest/queries.html

be > 21 and > 7 days from the first and latest distinct detections, respectively. The names of the transients are returned in descending order of first detection.

```
WITH TransientStats AS
(
    SELECT
        t.id,
        t.‘name‘,
        MIN(pd.obs_date) AS ‘first_detection‘,
        MAX(pd.obs_date) AS ‘latest_detection‘,
        COUNT(pd.obs_date) AS ‘number_of_detection‘
    FROM YSE_App_transient t
    JOIN YSE_App_transientphotometry tp ON tp.transient_id = t.id
    JOIN YSE_App_transientphotdata pd ON pd.photometry_id = tp.id
    WHERE
        (pd.flux/pd.flux_err) >= 2 AND
        pd.mag_err < 1.0 AND
        t.TNS_spec_class IS NULL AND
        t.dec <= -30
    GROUP BY
        t.id
)
SELECT
    ‘name‘
FROM
    TransientStats ts
WHERE
    TO_DAYS(CURDATE())- TO_DAYS(first_detection) < 21 AND
    TO_DAYS(CURDATE())- TO_DAYS(latest_detection) < 7 AND
    TO_DAYS(latest_detection) - TO_DAYS(first_detection) > 0.01 AND
    number_of_detection > 1
ORDER BY
    first_detection DESC;
```

2.8.3 Selecting a magnitude-limited sample

```
SELECT
    DISTINCT t.name,
    t.ra,
    t.‘dec‘
FROM YSE_App_transient t, YSE_App_transientphotdata pd, YSE_App_transientphotometry p
```

```
WHERE
    pd.photometry_id = p.id AND
    pd.id = (
        SELECT
            pd2.id
        FROM YSE_App_transientphotdata pd2,     YSE_App_transientphotometry p2
        WHERE
            pd2.photometry_id = p2.id AND
            p2.transient_id = t.id AND
            ISNULL(pd2.mag) = False AND
            pd2.flux/pd2.flux_err > 3
        ORDER BY
            pd2.mag ASC
         LIMIT 1
     ) AND

  pd.mag < 17 AND
  t.‘dec‘ > -30 AND
  (t.name LIKE ’202%’ OR t.name LIKE ’201%’) AND
  DATEDIFF(curdate(),t.disc_date) < 365 AND
  t.TNS_spec_class is not NULL AND
  t.TNS_spec_class != ’CV’ AND
  t.TNS_spec_class != ’SN Ia’;
```

2.9 Publications enabled by YSE-PZ

A non-exhaustive search of the literature reveals that YSE-PZ has enabled the following publications in some capacity: Fulton et al. (2023), Angus et al. (2022), Aleo et al. (2022), Davis et al. (2022), Ward et al. (2022), Kilpatrick et al. (2022b), Pastorello et al. (2022), Jacobson-Galán et al. (2022b), Tinyanont et al. (2022), Dimitriadis et al. (2022), Gagliano et al. (2022), Jacobson-Galán et al. (2022a), Dettman et al. (2021), Kilpatrick et al. (2021), Wang et al. (2021), Armstrong et al. (2021), Jencson et al. (2021), Barna et al. (2021), Jones et al. (2021), Hinkle et al. (2021), Holoien et al. (2020), Hung et al. (2020), Jacobson-Galán et al. (2020a), Jacobson-Galán et al. (2020b), Neustadt et al. (2020), Dimitriadis et al. (2019a), Jones et al.

(2019), Li et al. (2019), Kilpatrick et al. (2018a), Kilpatrick et al. (2018b), Tartaglia et al. (2018).

Chapter 3

Swope Supernova Survey 2017a (SSS17a), the Optical Counterpart to a Gravitational Wave Source

3.1 Introduction

Merging binary compact objects such as black holes (BHs) and neutron stars (NSs) are expected to be gravitational wave (GW) sources in the 10–10^4 Hz frequency range Thorne (1987) that can be observed using interferometers. The Laser Interferometer Gravitational-wave Observatory (LIGO) recently used this method to detect several binary BH (BBH) mergers Abbott et al. (2016c,e, 2017b). These discoveries have unveiled a population of relatively massive black holes, tested General Relativity, and led to insights regarding stellar evolution and binary populations Abbott et al. (2016a,d). Although it is unlikely that BBH systems produce a

luminous electromagnetic (EM) signature, detecting an EM counterpart to a GW event would greatly improve our understanding of the event by providing a precise location and insight into the merger products. Unlike BBH mergers, binary NS (BNS) mergers are expected to produce gravitationally unbound radioactive material that is visible at optical and infrared wavelengths (a kilonova) Li & Paczyński (1998); Metzger et al. (2010); Roberts et al. (2011); Barnes et al. (2016) and perhaps relativistic jets seen as short gamma-ray bursts (SGRBs) Lee & Ramirez-Ruiz (2007); Berger (2014). BNS mergers should produce transient, temporally coincident GWs and light. This has many advantages in comparison to detecting GWs alone, such as possibly constraining the nuclear equation of state, measuring the production of heavy-elements, studying the expansion of the Universe, and generating a clearer picture of the merger event Freiburghaus et al. (1999); Lattimer & Prakash (2000); Dalal et al. (2006).

3.2 GW170817 and the One-Meter Two-Hemispheres Collaboration

On 2017 August 17, LIGO/Virgo detected a strong GW signal consistent with a BNS merger, GW170817 LIGO/Virgo collaboration (2017a). A preliminary analysis of the GW data suggested that the two component masses were small enough to be a BNS system. This event had a low false-alarm rate of 1 per 10,000 years, a 90-percent chance of being localized to an area of 31 deg^2 (Figs. 1 & 2), and a distance of $D = 40 \pm 8$ megaparsecs (Mpc) LIGO/Virgo collaboration (2017a,b). Contemporaneously, the *Fermi* and INTErnational Gamma-Ray Astrophysics Laboratory (INTEGRAL) gamma-ray telescopes detected a SGRB both spatially and tempo-

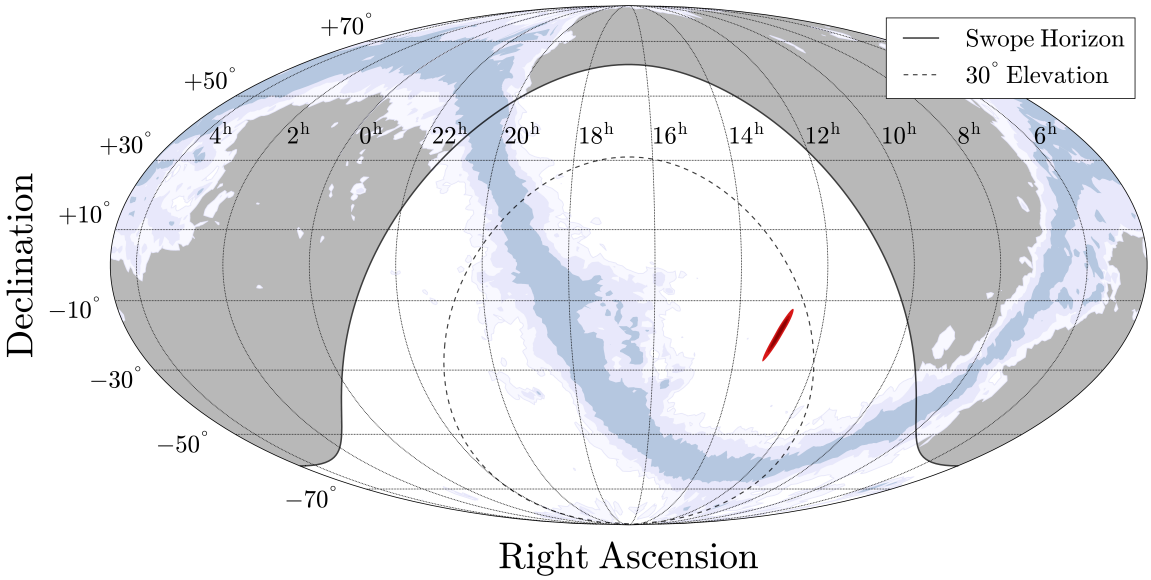

Figure 3.1 **Gravitational-wave localization of GW170817.** The outer edge of the red region represents the 90th-percentile confidence region as extracted from the revised `BAYESTAR` probability map. Also shown is the Milky Way in blue for context, with the outermost blue contour corresponding to V-band extinction $A_V = 0.5$ mag. The thick solid line represents the horizon as seen from the Swope telescope on 2017 August 17 at 23:33 UT, the time we observed SSS17a. The dotted line represents an elevation above the horizon of 30° (corresponding to an airmass of 2.0).

rally coincident with the GW event, GRB170817A. However, the *Fermi*/INTEGRAL localization area was larger than the LIGO/Virgo localization area GBM-LIGO (2017); INTEGRAL (2017).

Our One-Meter, Two-Hemisphere (1M2H) collaboration uses two 1-m telescopes, the Nickel telescope at Lick Observatory in California and the Swope telescope at Las Campanas Observatory in Chile, to search for EM counterparts to GW sources. Our strategy involves observing previously catalogued galaxies whose properties are consistent with the GW data to search for new sources. This strategy is particularly effective for nearby events with a small distance uncertainty, which reduces the surface density of viable targets Gehrels et al. (2016). We observe in either i' or i band filters (Nickel and Swope, respectively) because those are the reddest bands available on those telescopes and theoretical models predicted that kilonova light curves would be particularly red Barnes et al. (2016).

As the center of the localization region was in the Southern hemisphere and relatively close to the Sun, the Nickel telescope could not observe the GW170817 localization region. For GW170817, we were able to also use both Magellan telescopes as part of the search [see (XX) for details], allowing a multi-wavelength campaign covering giH bands. At the time of the trigger, the local time in Chile was 9:41 am (when the Sun was above the horizon), so observations could not begin for more than 10 hours. Because of the GW position, the majority of the 90-percentile localization region was expected to only be accessible for the first 2 hours after civil twilight that evening (Fig. 1).

3.3 Detection of SSS17a

Using a catalog of nearby galaxies and the three-dimensional (3D) GW localization of GW170817 (see Section 3.4), we created a prioritized list of galaxies in which the source of the GW event could reside (Table S1). Our prioritization algorithm includes information about the stellar mass and star-formation rate of the galaxy. We examined the positions of the 100 highest-priority galaxies to see if multiple galaxies could fit in a single Swope image (field of view of 29.7 arcminutes × 29.8 arcminutes), so that we could cover the probable locations as efficiently as possible. We were able to combine 46 galaxies in a total of 12 images (Fig. 2). The remaining galaxies on the initial list were sufficiently isolated to require their own images. We designed an observing schedule that first observed the 12 positions covering multiple galaxies, followed by individual galaxies in order of their priority while they were approximately 19.5 degrees above the horizon (corresponding to an airmass of 3.0).

Starting at 23:13 UT, when nautical twilight ended (Sun > 12 degrees below the horizon), 45 minutes after sunset, and ten hours after the GW trigger, we began observing the GW170817 localization region with an i-band filter. The 60-second exposures had a point-source limiting magnitude of 20.0 mag, corresponding to an absolute magnitude M_i of −13.0 mag at a distance of $D = 40$ Mpc (uncorrected for foreground Milky Way extinction). We immediately transferred, reduced, and examined each image by eye. In the ninth image (Fig. 3), which was initiated at 23:33 UT and contained two high-priority targeted galaxies, we detected an $i = 17.476 \pm 0.018$ mag source that was not present in archival imaging (Fig. 4). We designate the source as Swope Supernova Survey 2017a (SSS17a); it is located at right ascension $13^{\rm h}09^{\rm m}48^{\rm s}.085 \pm 0.018$, declination $-23°22'53''.343 \pm 0.218$ (J2000 equinox). SSS17a is offset

10.6″ (corresponding to 2.0 kpc at 40 Mpc) from the nucleus of NGC 4993, an S0 galaxy at a redshift of 0.009680 Jones et al. (2009) and a Tully-Fisher distance of 40 Mpc Freedman et al. (2001). NGC 4993 was the twelfth most likely host galaxy based on our algorithm, with a 2.2% probability of being the host galaxy (see Table S1).

After confirming that SSS17a was not a previously known asteroid or supernova, we triggered additional follow-up observations Drout et al. (2017); Pan et al. (2017); Shappee et al. (2017) and disseminated our discovery through a LIGO-Virgo Collaboration (LVC) Gamma-ray Coordination Network (GCN) circular [One-Meter Two-Hemisphere (1M2H) collaboration (2017), see (XX) for details]. We quickly confirmed SSS17a in a Magellan image performing a similar galaxy-targeted search [Simon et al. (2017), (XX)]. Subsequent observations by other teams also confirmed the presence of the new source [see **?** for a complete list]. We observed an additional 45 fields after identifying the new source, acquiring 54 images over 3.5 hours and covering 95.3% of the total probability (as determined by our algorithm) and 26.9% of the two-dimensional localization probability. Comparing to Swope images obtained 18–20 days after the trigger, we found no transient objects other than SSS17a in either set of images. Most galaxies are about $\sim 7'$ from the edge of a Swope image (1/4 the size of the field of view), corresponding to $\sim$80 kpc at 40 Mpc. For these regions covered by our images, we can exclude another luminous transient from being associated with GW170817 at the 95.3% confidence level [e.g., (XX)]. The combination of all available data further indicates that SSS17a is physically associated with GW170817 (probability of a chance coincidence is 9.4×10^{-6}) Foley (2017); Siebert et al. (2017).

Our observations were made with a 1-m telescope with an approximately quarter square degree field-of-view camera. This is in contrast to the strategy of using wide-field cameras, often

on larger-aperture telescopes to observe the entire localization region, unguided by the positions of known galaxies Smartt et al. (2016); Soares-Santos et al. (2016). While wide-field imagers might be necessary to discover an EM counterpart in a larger localization error region or in a low-luminosity galaxy, such instrumentation was not necessary for the case of GW170817/SSS17a. Nearly every optical observatory has an instrument suitable for our strategy; even some amateur astronomers have sufficient instrumentation to perform a similar search. If SSS17a is typical of future EM counterparts to LIGO/Virgo GW discoveries, telescope location and observational strategy – not aperture or field of view – will be the most important factors for EM counterpart discovery.

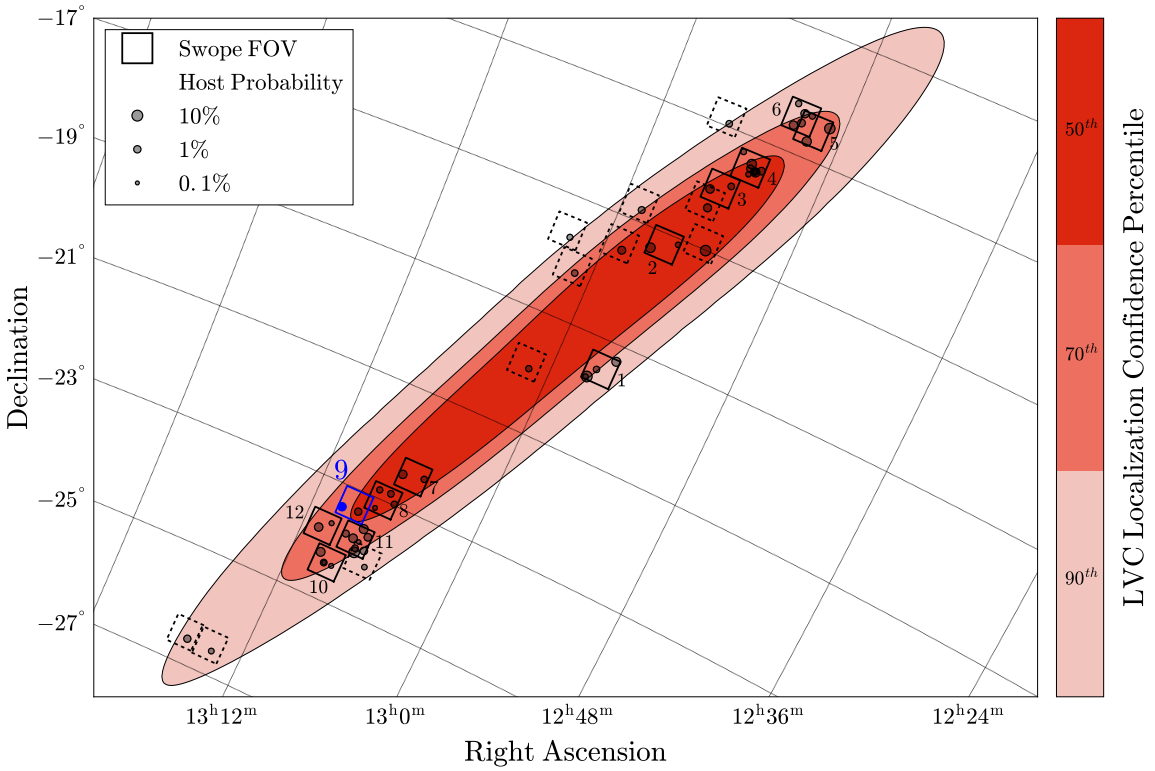

Figure 3.2 **Sky region covering the 90th-percentile confidence region for the location of GW170817.** The 50th, 70th, and 90th-percentile contours are shown, with contours extracted from the same probability map as Fig. 1. Grey circles represent the locations of galaxies in our galaxy catalog and observed by the Swope telescope on 2017 August 17-18 to search for the EM counterpart to GW170817. The size of the circle indicates the probability of a particular galaxy being the host galaxy for GW170817. The square regions represent individual Swope pointings with the solid squares specifically chosen to contain multiple galaxies (and labeled in the order that they were observed) and the dotted squares being pointings which contained individual galaxies. The blue square labeled '9' contains NGC 4993, whose location is marked by the blue circle, and SSS17a.

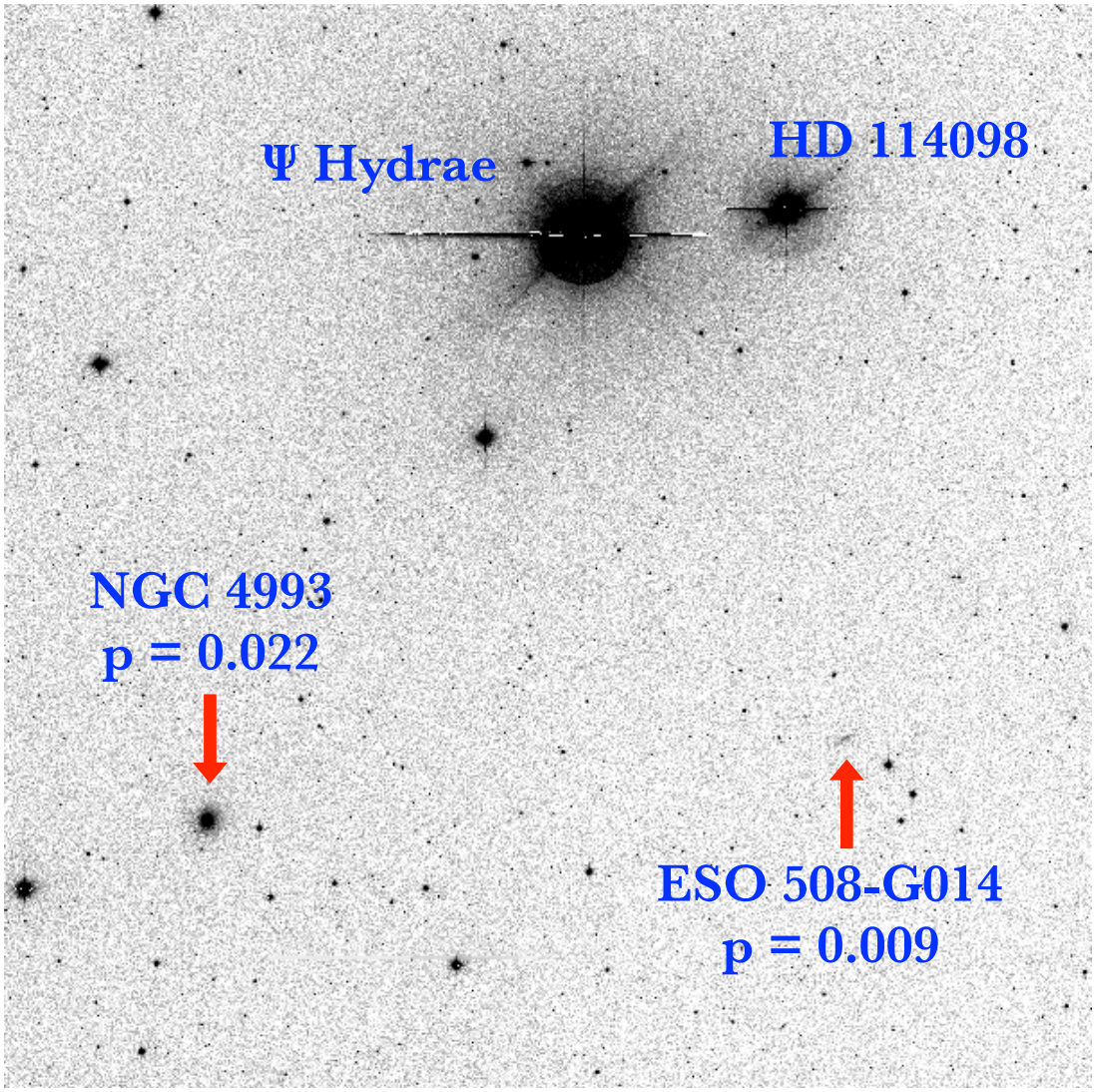

Figure 3.3 **Full-field Swope telescope i-band image containing NGC 4993 (Field 9 in Fig. 2).** The bright stars Ψ Hydrae and HD 114098 are labeled. The galaxies NGC 4993 and ESO 508-G014, which had probabilities of hosting GW170817 of 0.022 and 0.009 (see Supplemental Information), respectively, are labeled and marked with red arrows.

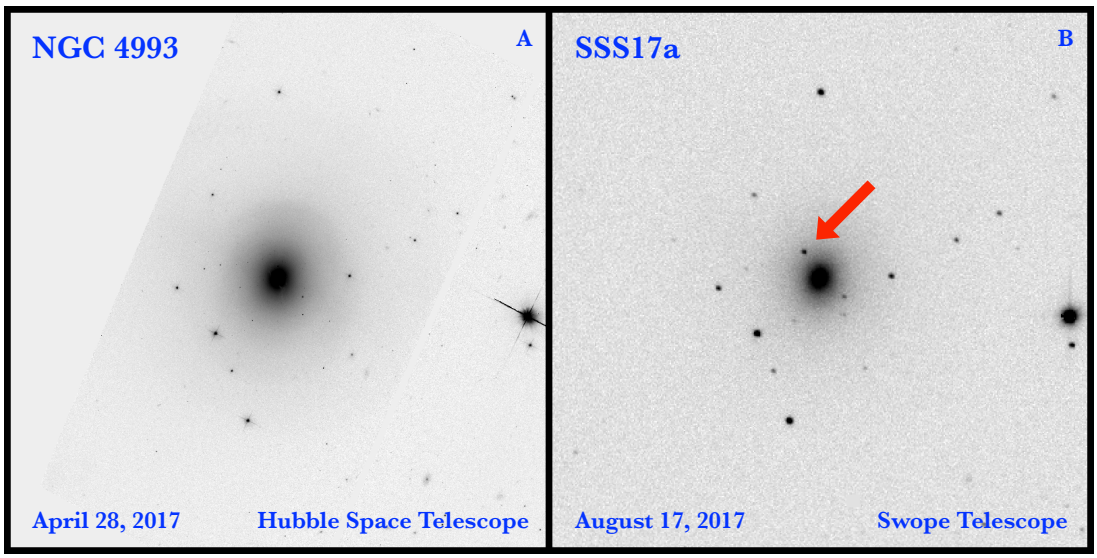

Figure 3.4 **3′ × 3′ images centered on NGC 4993 with North up and East left.** *Panel A*: *Hubble Space Telescope* F606W-band (broad V) image from 4 months before the GW trigger Foley et al. (2017); Pan et al. (2017). *Panel B*: Swope image of SSS17a. The i-band image was obtained on 2017 August 17 at 23:33 UT by the Swope telescope at Las Campanas Observatory. SSS17a is marked with the red arrow. No object is present in the *Hubble* image at the position of SSS17a Foley et al. (2017); Pan et al. (2017).

3.4 Materials and Methods

3.4.1 Galaxy Prioritization and Scheduling Algorithms

To improve the chances of detecting an EM counterpart to a GW source, we generate a prioritized list of targets, which we then attempt to combine into as few images as possible, and then produce an observing schedule to be executed by an on-site observer.

We start with a catalog of nearby galaxies specifically created for the purpose of targeted-galaxy GW searches White et al. (2011). The catalog contains 53,161 galaxies, is nearly complete to 40 Mpc (in terms of stellar mass), and still has high completeness to 100 Mpc. In addition to positions and distances, the catalog includes B-band magnitudes, from which we calculate a B-band luminosity that is a proxy for some combination of total stellar mass (more massive galaxies are more luminous) and star-formation rate (SFR; bluer galaxies are more vigorously forming stars). Both are useful for EM searches of GW sources since more massive galaxies have more BNS systems and the theoretical merger rate depends on the SFR Phinney (1991); Belczynski et al. (2002).

Our algorithm depends on the three-dimensional localization probability maps produced by LVC. In the case of GW170817, we used the revised `BAYESTAR` map LIGO/Virgo collaboration (2017b); Singer & Price (2016). This map contains a two-dimensional (plane of the sky) probability and a distance (and distance uncertainty) for pixels in a Hierarchical Equal Area isoLatitude Pixelization (HEALPix) map. Since GW170817 had an associated SGRB GBM-LIGO (2017); INTEGRAL (2017), which might imply a face-on system and thus a larger distance LIGO/Virgo collaboration (2017b), we assumed a single distance for every pixel of the

probability map with an inflated uncertainty, $D = 43 \pm 12$ Mpc.

For each galaxy in the catalog, we calculate a B-band luminosity proxy, $\tilde{L}_B$ (uncorrected for Milky Way extinction),

$$\tilde{L}_B = D_{\rm gal}^2 10^{-0.4 m_B}, \tag{3.1}$$

where $D_{\rm gal}$ is the catalog distance for a galaxy and m_B is its B-band magnitude.

Combining the two-dimensional location, distance, and galaxy luminosity, we obtain our final probability:

$$P_{\rm gal} = k^{-1} \times \tilde{L}_B \times P_{\rm 2D} \times \left(1 - {\rm erf}\left(\frac{|{\rm D_{gal}} - {\rm D_{LVC}}|}{\sigma^2_{\rm D,\ gal} + \sigma^2_{\rm D,\ LVC}}\right)\right), \tag{3.2}$$

where $P_{\rm gal}$ is the probability that a particular galaxy hosts the GW event, k is a normalization factor such that all probabilities sum to 1, $P_{\rm 2D}$ is the two-dimensional probability for a particular galaxy, $D_{\rm gal}$ and $\sigma_{D,\ {\rm gal}}$ are the distance and distance uncertainty for the galaxy, and $D_{\rm LVC}$ and $\sigma_{D,\ {\rm LVC}}$ are the distance and distance uncertainty for the GW source.

We then attempted to schedule the 1000 highest-probability galaxies for observations with the Swope telescope, the Magellan Clay telescope with the LDSS-3 imaging spectrograph and the Magellan Baade telescope with the FourStar near-infrared camera Persson et al. (2013). Using all three telescopes for the search enabled us to cover a range of optical and near-IR wavelengths over which a counterpart could be detected. Our scheduling algorithm takes an input of object positions, using the computed probabilities as priorities, and takes into account observational constraints such as the total observing time for each object (exposure plus over-

head) to produce a schedule. The algorithm maximizes a merit function based on a total net priority that includes the object's observing constraints in addition to its computed probability, and it attempts to place the highest net-priority targets at each target's lowest airmass. For the GW170817 search, all exposure times were identical and every target was setting, which reduced the algorithm to scheduling the highest-probability unobserved targets above our airmass limit of 3 at any given time.

Using our scheduling algorithm, we were able to schedule $\sim$ 100 galaxies with non-negligible probability, indicating roughly the number of observations we could perform before all high-probability galaxies set below our airmass limit. We then examined the positions of the 100 highest-probability galaxies to determine if multiple galaxies could be observed simultaneously. We visually examined the galaxy positions and were able to group 46 galaxies into 12 separate telescope pointings, improving our efficiency by a factor of 3.8 for the grouped galaxies, and 52% for the 100 highest-priority galaxies.

We added special targets corresponding to the positions of the multi-galaxy fields and assigned them a high (and equal) priority to guarantee that they would be observed. By including the multi-galaxy fields, we freed up time to observe 34 additional high-probability galaxies. After swapping galaxies for multi-galaxy fields covering those same galaxies in our target list, we recomputed an observing schedule. We did not attempt to further optimize the pointings.

Table 3.1 contains a list of observed galaxies, their probabilities, and the order of observation for each telescope.

Table 3.1. Observation Schedule

Galaxy	R.A.	Decl.	Probability	Observation Number		
				Swope	LDSS-3	FourStar
NGC 4830	12:57:27.9	-19:41:29.0	0.086207	1	2	1
NGC 4970	13:07:33.7	-24:00:31.0	0.083333	11	3	9
NGC 4763	12:53:27.2	-17:00:19.0	0.077519	13	4	2
IC 3799	12:48:59.7	-14:23:57.0	0.073529	5	5	3
PGC 044234	12:57:00.5	-17:19:13.0	0.044248	2	6	4
NGC 4756	12:52:52.6	-15:24:48.0	0.037037	4	7	5
PGC 043424	12:50:04.7	-14:44:01.0	0.034014	5	8	6
ESO 575-G029	12:55:59.7	-19:16:08.0	0.028818	1	9	
ESO 508-G010	13:07:37.8	-23:34:44.0	0.027855	11	10	
PGC 043664	12:52:25.6	-15:31:02.0	0.026316	4	1	7
ESO 508-G019	13:09:51.7	-24:14:22.0	0.025773	10	11	
NGC 4993	**13:09:47.7**	**-23:23:02.0**	**0.021463**	**9**	**12**	**11**
IC 4197	13:08:04.3	-23:47:49.0	0.021368	11		
ESO 508-G024	13:10:45.9	-23:51:56.0	0.020243	12		
PGC 043966	12:54:49.5	-16:03:08.0	0.019531	3		
IC 3831	12:51:18.6	-14:34:25.0	0.019531	6		
ESO 575-G055	13:06:39.9	-22:27:21.0	0.018762	7		
NGC 4724	12:50:53.6	-14:19:55.0	0.018116	5, 6		
PGC 043908	12:54:28.9	-16:21:03.0	0.015152	14		
PGC 044500	12:58:45.6	-17:32:35.0	0.013812	15		
IC 3827	12:50:52.2	-14:29:31.0	0.012453	5, 6		
NGC 4968	13:07:05.8	-23:40:37.0	0.012225	11		
PGC 043625	12:52:05.4	-15:27:30.0	0.011403	4		
IC 4180	13:06:56.5	-23:55:01.0	0.010776	11		10
PGC 043720	12:52:51.1	-15:29:30.0	0.009615	4	1	7
ESO 508-G014	13:08:32.3	-23:20:50.0	0.009174	9		
ESO 508-G033	13:16:23.3	-26:33:42.0	0.009091	16		
PGC 797164	13:08:42.5	-23:46:33.0	0.007634	11		
PGC 044478	12:58:34.4	-16:48:16.0	0.007246	17		
PGC 043662	12:52:29.4	-15:29:58.0	0.006536	4	1	7
ESO 508-G015	13:09:18.9	-24:23:05.0	0.006211	10		8
PGC 043808	12:53:33.9	-15:52:44.0	0.006061	3		
ESO 508-G004	13:06:52.6	-22:50:30.0	0.005952	8		
PGC 183552	13:07:37.7	-23:56:18.0	0.005848	11	3	9, 10
PGC 044021	12:55:19.3	-14:57:00.0	0.005780	18		
PGC 169673	13:06:19.4	-22:58:49.0	0.005747	8		
IC 0829	12:52:33.0	-15:31:00.0	0.005682	4	1	7
ESO 575-G047	13:01:09.2	-18:11:52.0	0.005556	19		
ESO 575-G035	12:57:02.7	-19:31:05.0	0.005319	1		
ESO 575-G053	13:05:04.9	-22:23:02.0	0.005102	7		
ESO 575-G048	13:01:26.8	-19:57:53.0	0.004762	20		
ESO 508-G011	13:07:44.9	-22:51:28.0	0.004608	8		
NGC 4726	12:51:32.4	-14:13:16.0	0.004525	6		
IC 3822	12:50:22.7	-14:19:18.0	0.004425	5, 6		
PGC 045006	13:02:25.9	-17:40:47.0	0.004149	21		
PGC 043823	12:53:42.3	-15:16:56.0	0.003401	4		
PGC 046026	13:14:17.7	-26:34:58.0	0.003390	22		
PGC 043663	12:52:27.4	-15:31:07.0	0.003195	4	1	7
ESO 508-G003	13:06:24.0	-24:09:51.0	0.002950	23		
PGC 043711	12:52:48.9	-15:35:21.0	0.002695	4		7
PGC 044312	12:57:32.7	-19:42:01.0	0.002660	1	2	1
PGC 044023	12:55:20.4	-17:05:47.0	0.002639	2		

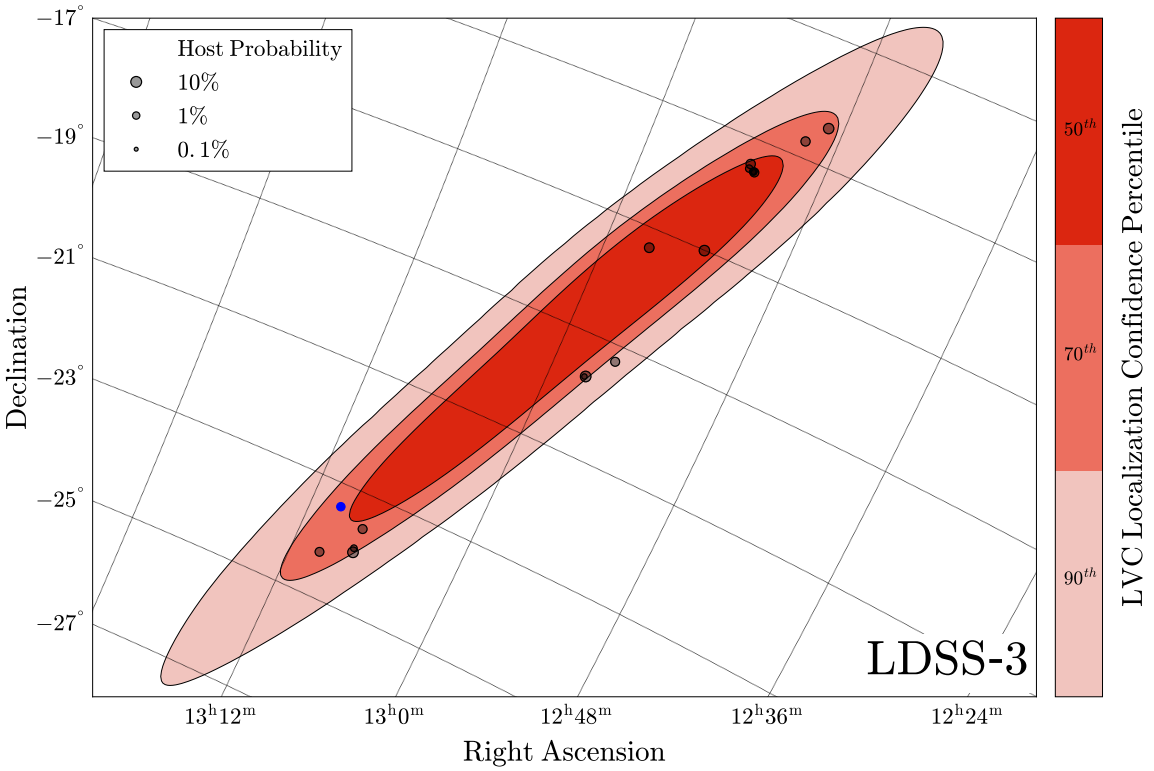

Figure 3.5 Same as Fig. 3.3, except displaying the galaxies observed by Magellan Clay/LDSS-3. NGC 4993 is marked by the blue circle.

While NGC 4993 was included in a multi-galaxy field, skipping this step would have delayed our imaging of NGC 4993 by only ∼6 minutes. That is, NGC 4993 was in the ninth image obtained, but was the twelfth-highest probability galaxy.

We applied the same algorithms to produce observing schedules for Magellan Clay/LDSS-3 and Magellan Baade/FourStar. Maps displaying the locations of galaxies observed by these telescopes are shown in Fig. S1 & S2, respectively.

Table 3.1 (cont'd)

Galaxy	R.A.	Decl.	Probability	Observation Number		
				Swope	LDSS-3	FourStar
NGC 5124	13:24:50.3	-30:18:27.0	0.002340	24		
NGC 5051	13:16:20.1	-28:17:09.0	0.002290	25		
ESO 508-G020	13:09:59.8	-23:42:52.0	0.002045	12		
PGC 045565	13:08:42.0	-24:22:58.0	0.001905	10		8
PGC 803966	13:07:30.9	-23:10:14.0	0.001736	8		
NGC 5078	13:19:50.1	-27:24:36.0	0.001630	26		
ESO 444-G012	13:20:50.2	-29:28:47.0	0.001580	27		
ESO 444-G026	13:24:29.0	-30:25:54.0	0.001560	28		
6dF J1309178-242256	13:09:17.7	-24:22:56.0	0.001520	10		8
Abell 1664-11	13:07:34.1	-23:48:54.7	0.001420	11		10
NGC 5114	13:24:01.7	-32:20:38.0	0.001300	29		
NGC 5135	13:25:44.0	-29:50:01.0	0.001260	30		
ESO 444-G021	13:23:30.6	-30:06:51.0	0.001250	31		
NGC 5048	13:16:08.4	-28:24:38.0	0.001160	32		
NGC 5193	13:31:53.5	-33:14:04.0	0.001100	33		
ESO 383-G005	13:29:23.6	-34:16:17.0	0.000937	34		
NGC 5140	13:26:21.7	-33:52:07.0	0.000914	35		
2MASX J13245297-3020059	13:24:53.0	-30:20:05.0	0.000429	36		
ESO 444-G019	13:23:06.3	-32:14:41.0	0.000328	37		
IC 4296	13:36:39.1	-33:57:57.0	0.000290	38		
ESO 221-G035	14:16:04.4	-52:36:31.0	0.000188	39		22
ESO 221-G030	14:10:41.1	-52:11:03.0	0.000171	40		23
ESO 175-G002	14:08:36.0	-53:21:10.0	0.000149	41		
ESO 383-G027	13:35:04.9	-35:16:09.0	0.000141	42		
ESO 324-G033	13:32:27.3	-38:10:06.0	0.000103	43		13
ESO 383-G047	13:37:50.6	-36:03:01.0	0.000077	44		
ESO 324-G044	13:38:06.2	-39:50:25.0	0.000066	45		12
ESO 221-G020	13:58:23.1	-48:28:34.0	0.000060	46		
PGC 141857	14:10:33.5	-52:19:02.0	0.000055	47		14
PGC 2800412	14:17:10.0	-55:37:12.0	0.000051	48		15
PGC 141859	14:20:23.5	-55:04:07.0	0.000051	49		16
PGC 166335	14:16:02.0	-53:42:59.0	0.000043	50		18
NGC 5365A	13:56:39.5	-44:00:33.0	0.000038	51		17
PGC 463082	14:03:29.3	-50:46:38.0	0.000037	52		19
PGC 166323	14:04:34.1	-52:41:50.0	0.000035	53		20
ESO 175-G005	14:17:47.0	-52:49:54.0	0.000033	54		21

Note. — A list of observed galaxies, their probabilities, and the order of observation for each telescope.

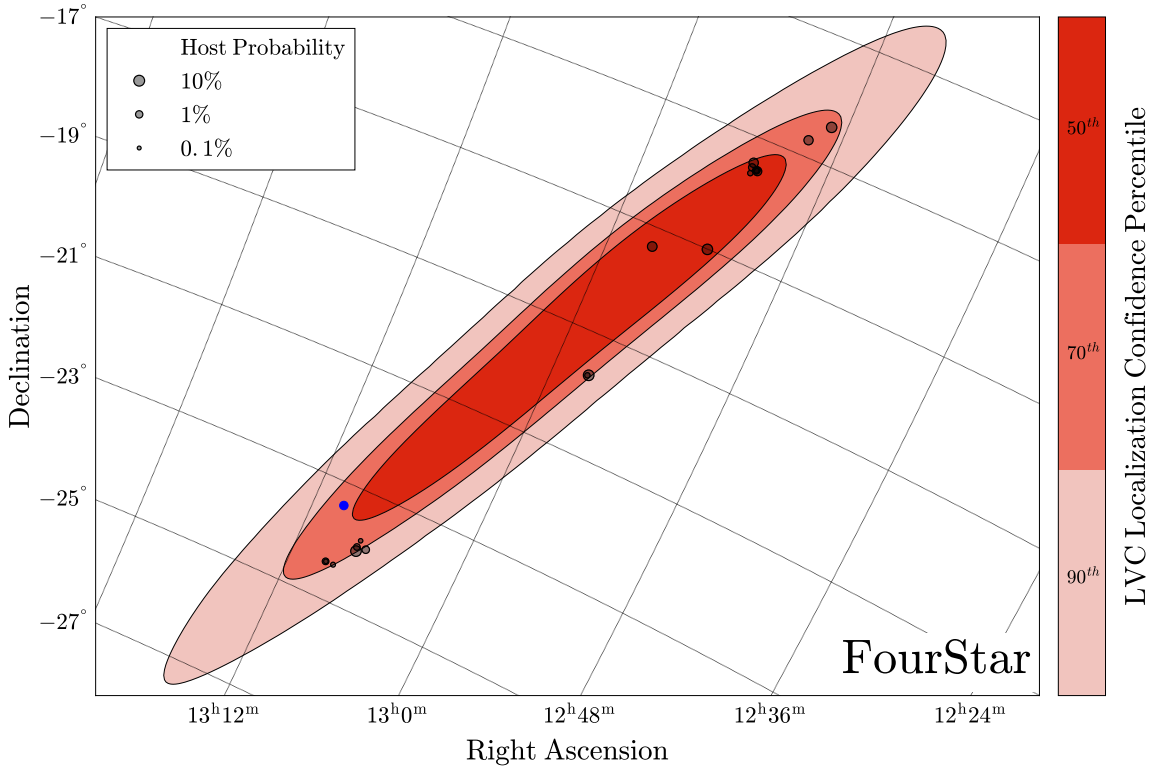

Figure 3.6 Same as Fig. 3.3, except displaying the galaxies observed by Magellan Baade/FourStar. NGC 4993 is marked by the blue circle.

3.4.2 Initial Transient Search

In preparing to search the LIGO/Virgo localization region for potential optical counterparts, we obtained template images of our galaxy fields from the National Optical Astronomy Observatory (NOAO) public archive[27]. Our preference was to obtain deep template images covering as many galaxies in our sample over as wide an area as possible and in a similar photometric band to the Swope i filter. Therefore, we searched the NOAO archive for Dark Energy Camera (DECam) Diehl et al. (2008) r- and i-band images covering as large a region as many of our galaxy fields as possible.

With the DECam reference images, we immediately identified the 100 highest-probability galaxies using `ds9` Joye & Mandel (2003) region files. As each Swope field was observed, we reduced the images using a reduction pipeline (described below). We then loaded each file into `ds9` to visually inspect the galaxies associated with each region.

Transient discovery by visual inspection is heavily biased toward bright, isolated sources, and so we used multiple kinds of scaling to inspect sources around each galaxy. This process included inspection of faint sources in the outskirts of each galaxy using typical linear scaling and sources deeply embedded in each galaxy with significantly higher clip values in order to resolve faint, nuclear sources. As we inspected each image, we blinked them rapidly with the DECam images in order to identify any differences between the images. Using this method, we were able to visually inspect a single image every $\sim$ 1 minute, which was appreciably faster than the total time allocated to expose on each field, read out the instrument, and slew to each successive field. However, accounting for image reductions, we visually inspected the initial images

[27] http://archive.noao.edu/

roughly 20 minutes after they were obtained.

The image containing SSS17a was the ninth image obtained, reduced, and inspected. As we demonstrate in Figs. 3 & 4, this field contained only two galaxies and the transient source was immediately apparent upon comparison with template imaging.

After the identification of this source at 23:59 UT (Fig. 3.8), we queried the Minor Planet Center[28] and Transient Name Server[29] databases to confirm that SSS17a was not a known asteroid or SN. Upon confirmation that SSS17a was an unknown source, our priorities immediately changed to characterization through follow-up observations. After additional observations, we continued our search to observe the remaining galaxies in our list. The fields observed are presented in Figure 3.4.1.

3.4.3 Astrometry

We determined the location of SSS17a from the centroid of our point-spread function (PSF) fit in the discovery i band image and the world-coordinate system (WCS) solution derived for that image. The astrometric uncertainty associated with the location of SSS17a is the 1-σ uncertainty on the PSF centroid and on the WCS solution added in quadrature. Our total astrometric uncertainty for SSS17a, which was detected at 17.476 mag in a relatively bright galaxy, was about $0.23''$.

[28] https://minorplanetcenter.net
[29] https://www.wis-tns.org/

3.4.4 Swope Photometry

Subsequent to discovery, we imaged the site of SSS17a in $BVgri$ bands with the Swope telescope from 2017 August 17-24, at which point it became too faint to detect in 30 minute i band images. After that time, we imaged the same field with long exposure times (20–60 minute) in order to construct deep templates for difference imaging.

We performed standard reductions on all of our Swope imaging using `photpipe` Rest et al. (2005), a well-tested pipeline used in the Swope Supernova Survey and several major time-domain surveys (Rest et al. 2014, e.g., Pan-STARRS1). We used `photpipe` to correct the Swope images for bias, flat-fielding, cross-talk, and overscan. We performed astrometric calibration and corrections for geometric distortion in `photpipe` by resampling each image onto a corrected grid with `SWarp` Bertin et al. (2002), then applied a WCS derived from the locations of stars in the 2MASS Point Source Catalog Skrutskie et al. (2006). We used `photpipe` to perform difference imaging with `hotpants` Alard (2000); Becker (2015), which uses a spatially varying convolution kernel to match the image and template PSF before image subtraction. As an example, we display the discovery image after image subtraction in Fig. S3. Finally, we performed photometry using `DoPhot`, which is optimized for PSF photometry on the difference images Schechter et al. (1993). Our $BVgri$ photometry was calibrated using Pan-STARRS1 (PS1) standard stars observed in the same field as SSS17a and transformed into the Swope natural system using Supercal transformations Scolnic et al. (2015).

The Swope photometry is presented in Fig. S4 and listed in Table S1.

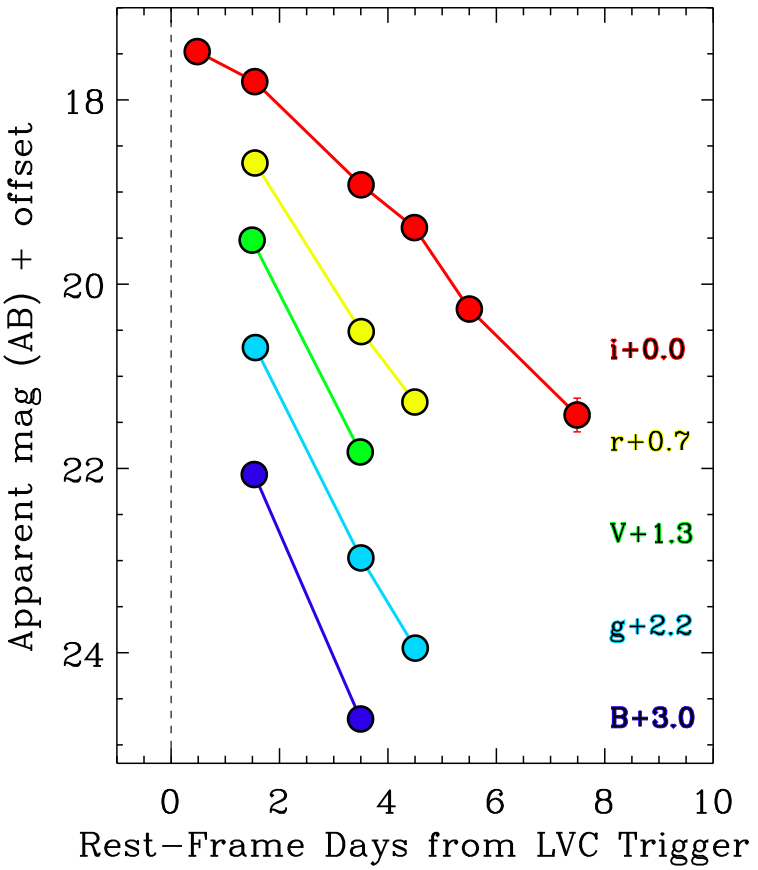

Figure 3.7 *BVgri* light curves of SSS17a. These data are analyzed in detail in Drout et al. (2017); Kilpatrick et al. (2017); Murguia-Berthier et al. (2017).

Table 3.2 Swope Photometry of SSS17a

Time since LVC Trigger	Filter	AB Magnitude (Uncertainty)
0.4529	i	17.476 (018)
1.4663	V	18.222 (041)
1.5057	B	19.066 (037)
1.5153	i	17.802 (020)
1.5187	r	17.985 (018)
1.5263	g	18.488 (124)
3.4608	V	20.521 (115)
3.4666	B	21.719 (126)
3.4728	g	20.771 (049)
3.4761	i	18.922 (047)
3.4791	r	19.815 (089)
4.4600	i	19.386 (045)
4.4680	r	20.579 (125)
4.4759	g	21.750 (104)
5.4735	i	20.270 (116)
7.4612	i	21.420 (183)

3.4.5 Extensive Transient Search

From 2017 September 4-7, we obtained follow-up 120 second i-band images of all fields observed with the Swope telescope on 2017 August 17. We performed difference imaging in the same manner using `photpipe` to search for new optical transients that had either faded since 2017 August 17, or appeared over the 18–20 day interval from the first to second epoch of observation. Apart from SSS17a, we did not detect any transients in any of our Swope fields.

We calculated a 5-σ limiting magnitude for each Swope image by examining sources with background fluxes within 10% of the median sky background. We then calculated the signal-to-noise ratio for each of those sources as estimated from the count rate and 1-σ uncertainty in the count rate. We fit a cubic spline to the signal-to-noise ratio versus magnitude and estimated the magnitude at which the signal-to-noise ratio was equal to 5.0. This 5-σ limit was typically

around 20.0 mag in the 60 second images from 2017 August 17, and 20.8 mag in the 120 second images from 2017 September 4-7.

Treating this 5-σ limit as a bolometric magnitude at the distance of NGC 4993, we would expect to detect all sources down to $M = -13.0$ to -12.2 mag. This limiting magnitude rules out the presence of most supernovae, even those observed within hours Foley et al. (2012); Pan et al. (2015); Shappee et al. (2016) or weeks after explosion Li et al. (2011). Very low-luminosity transients such as classical novae and intermediate luminosity red transients Mould et al. (1990) are faint enough to be missed by our optical survey, but neither of these classes of sources are thought to be strong sources of GW emission.

Our choice of filter was also designed to target EM emission associated with predictions from kilonova models, which are expected to have very high optical opacities and thus very red colors Li & Paczyński (1998). If the theoretical predictions were incorrect and the intrinsic color of EM counterparts are blue, it is still unlikely that any source would be so blue to be detected in a bluer band (e.g., g) and not i. SSS17a is well-fit by kilonova models Drout et al. (2017); Kilpatrick et al. (2017), but with an added component that is hot ($> 10,000$ K) within hours of the LVC trigger and cooled rapidly over several days.

3.4.6 1M2H Slack Conversation

At the time of the GW170817 alert, D. Coulter, R. Foley, and M. Siebert were at the Dark Cosmology Centre in Copenhagen, Denmark, while C. Kilpatrick and C. Rojas-Bravo were in Santa Cruz, California. Meanwhile, B. Shappee, J. Simon, and N. Ulloa were at Las Campanas Observatory with M. Drout supporting from Pasadena, California. Both because of

the multiple locations and for its speed, we used Slack to communicate. In Figs. S5–S17, we present our conversation, which includes the timeline of our evolving strategy and discovery of SSS17a. All times displayed are Pacific Daylight Time.

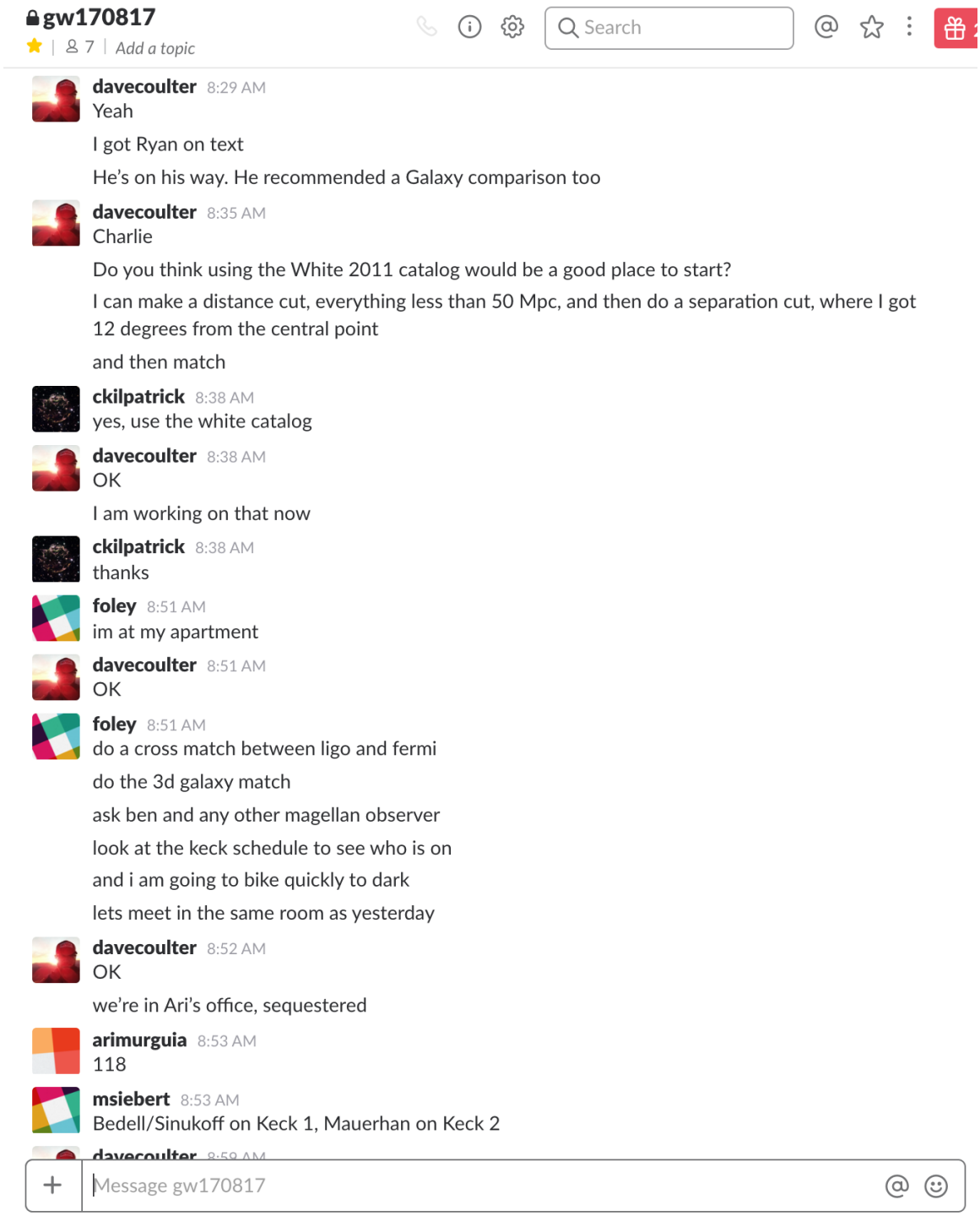
gw170817
7
Add a topic
Search
davecoulter 8:29 AM
Yeah
I got Ryan on text
He's on his way. He recommended a Galaxy comparison too
davecoulter 8:35 AM
Charlie
Do you think using the White 2011 catalog would be a good place to start?
I can make a distance cut, everything less than 50 Mpc, and then do a separation cut, where I got 12 degrees from the central point
and then match
ckilpatrick 8:38 AM
yes, use the white catalog
davecoulter 8:38 AM
OK
I am working on that now
ckilpatrick 8:38 AM
thanks
foley 8:51 AM
im at my apartment
davecoulter 8:51 AM
OK
foley 8:51 AM
do a cross match between ligo and fermi
do the 3d galaxy match
ask ben and any other magellan observer
look at the keck schedule to see who is on
and i am going to bike quickly to dark
lets meet in the same room as yesterday
davecoulter 8:52 AM
OK
we're in Ari's office, sequestered
arimurguia 8:53 AM
118
msiebert 8:53 AM
Bedell/Sinukoff on Keck 1, Mauerhan on Keck 2
Message gw170817

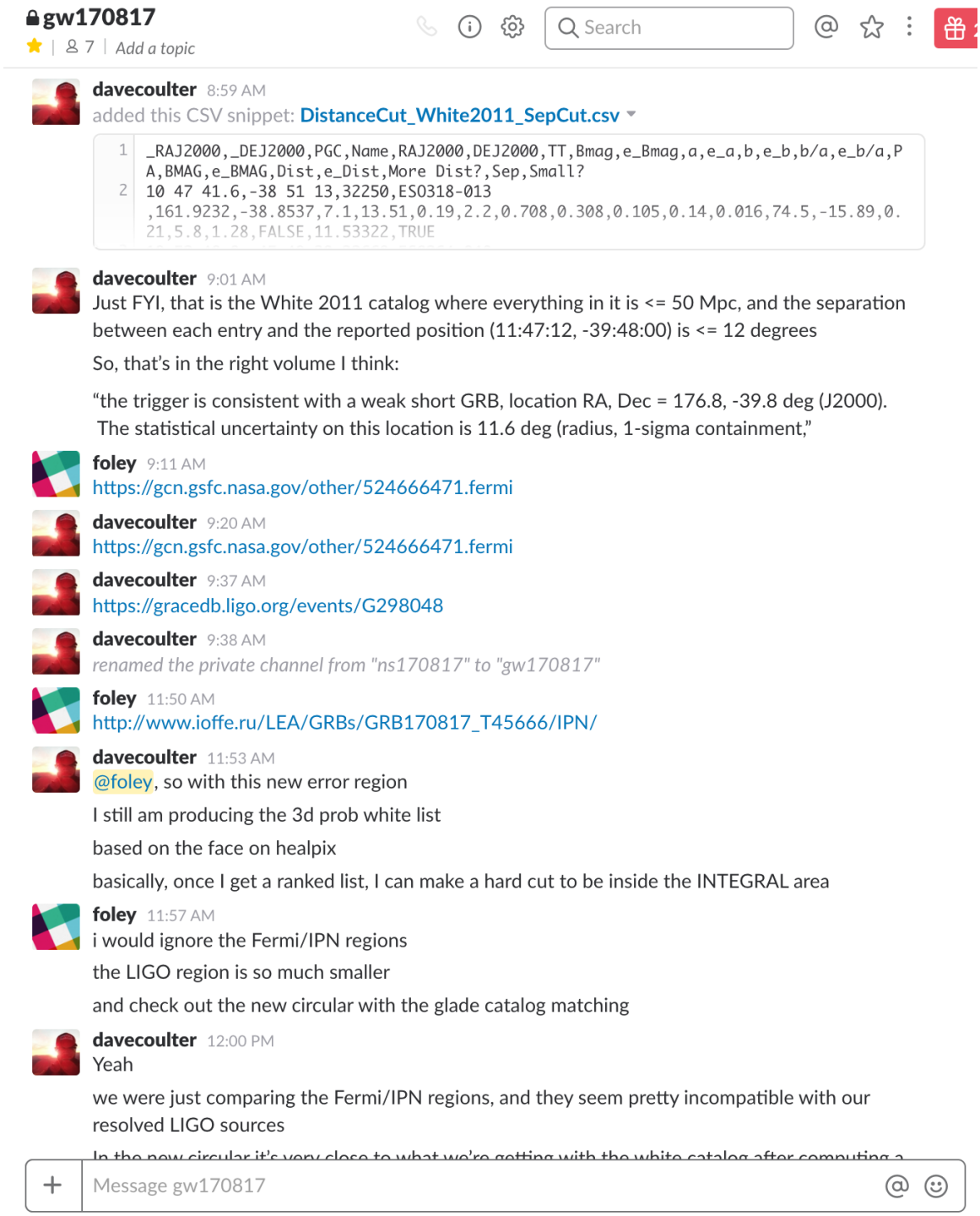
gw170817
7
Add a topic
Search
davecoulter 8:59 AM
added this CSV snippet: DistanceCut_White2011_SepCut.csv
1 _RAJ2000,_DEJ2000,PGC,Name,RAJ2000,DEJ2000,TT,Bmag,e_Bmag,a,e_a,b,e_b,b/a,e_b/a,PA,BMAG,e_BMAG,Dist,e_Dist,More Dist?,Sep,Small?
2 10 47 41.6,-38 51 13,32250,ESO318-013,161.9232,-38.8537,7.1,13.51,0.19,2.2,0.708,0.308,0.105,0.14,0.016,74.5,-15.89,0.21,5.8,1.28,FALSE,11.53322,TRUE
davecoulter 9:01 AM
Just FYI, that is the White 2011 catalog where everything in it is <= 50 Mpc, and the separation between each entry and the reported position (11:47:12, -39:48:00) is <= 12 degrees
So, that's in the right volume I think:
"the trigger is consistent with a weak short GRB, location RA, Dec = 176.8, -39.8 deg (J2000). The statistical uncertainty on this location is 11.6 deg (radius, 1-sigma containment,"
foley 9:11 AM
https://gcn.gsfc.nasa.gov/other/524666471.fermi
davecoulter 9:20 AM
https://gcn.gsfc.nasa.gov/other/524666471.fermi
davecoulter 9:37 AM
https://gracedb.ligo.org/events/G298048
davecoulter 9:38 AM
renamed the private channel from "ns170817" to "gw170817"
foley 11:50 AM
http://www.ioffe.ru/LEA/GRBs/GRB170817_T45666/IPN/
davecoulter 11:53 AM
@foley, so with this new error region
I still am producing the 3d prob white list
based on the face on healpix
basically, once I get a ranked list, I can make a hard cut to be inside the INTEGRAL area
foley 11:57 AM
i would ignore the Fermi/IPN regions
the LIGO region is so much smaller
and check out the new circular with the glade catalog matching
davecoulter 12:00 PM
Yeah
we were just comparing the Fermi/IPN regions, and they seem pretty incompatible with our resolved LIGO sources
In the new circular it's very close to what we're getting with the white catalog after computing a
Message gw170817

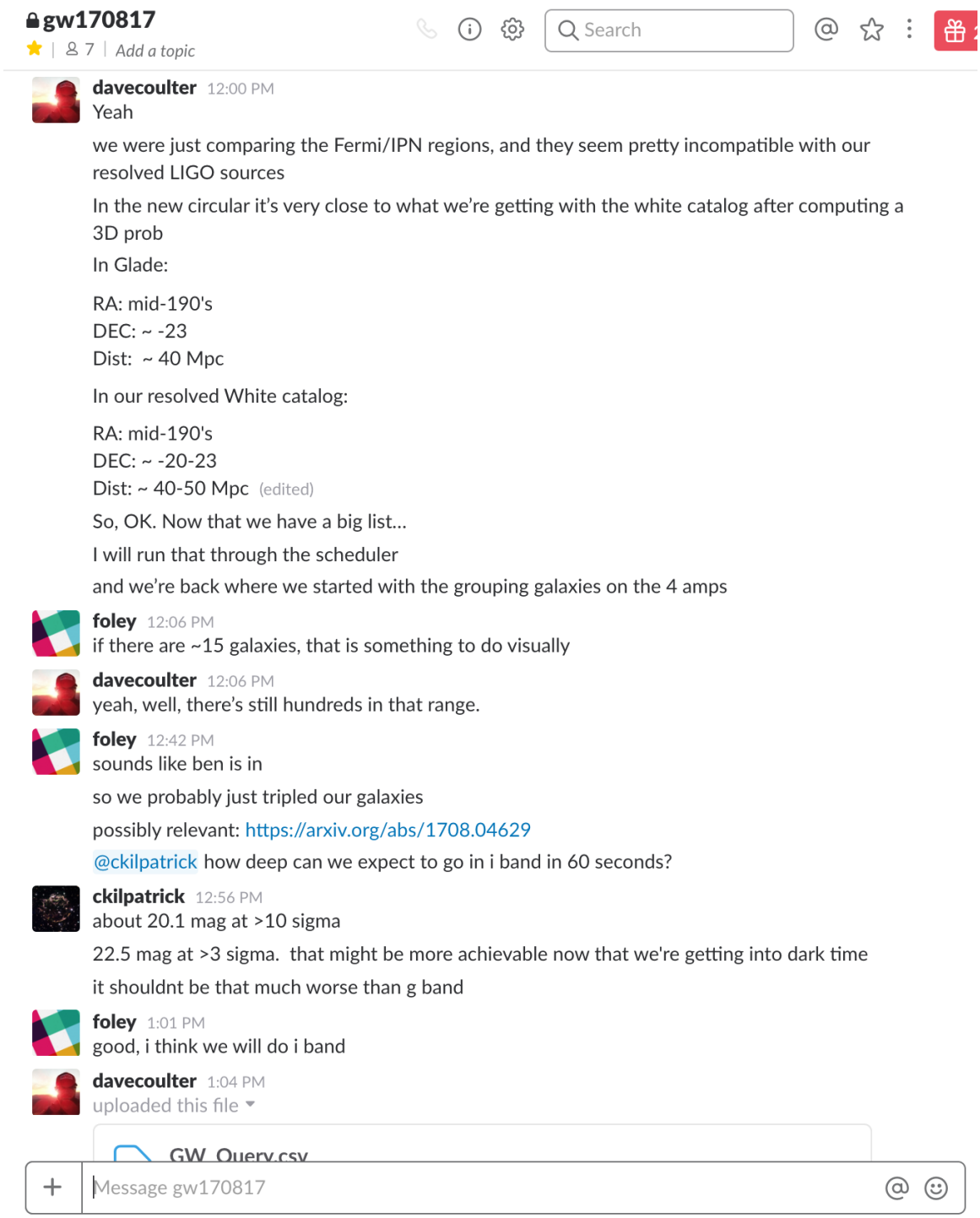
gw170817
7
Add a topic
Search
davecoulter 12:00 PM
Yeah
we were just comparing the Fermi/IPN regions, and they seem pretty incompatible with our resolved LIGO sources
In the new circular it's very close to what we're getting with the white catalog after computing a 3D prob
In Glade:
RA: mid-190's
DEC: ~ -23
Dist: ~ 40 Mpc
In our resolved White catalog:
RA: mid-190's
DEC: ~ -20-23
Dist: ~ 40-50 Mpc (edited)
So, OK. Now that we have a big list...
I will run that through the scheduler
and we're back where we started with the grouping galaxies on the 4 amps
foley 12:06 PM
if there are ~15 galaxies, that is something to do visually
davecoulter 12:06 PM
yeah, well, there's still hundreds in that range.
foley 12:42 PM
sounds like ben is in
so we probably just tripled our galaxies
possibly relevant: https://arxiv.org/abs/1708.04629
@ckilpatrick how deep can we expect to go in i band in 60 seconds?
ckilpatrick 12:56 PM
about 20.1 mag at >10 sigma
22.5 mag at >3 sigma. that might be more achievable now that we're getting into dark time
it shouldnt be that much worse than g band
foley 1:01 PM
good, i think we will do i band
davecoulter 1:04 PM
uploaded this file
GW_Query.csv
Message gw170817

gw170817

7 | Add a topic

Search

davecoulter 1:04 PM
uploaded this file

GW_Query.csv
8MB CSV

foley 1:35 PM
uploaded and commented on this file

lc_mv_m.pdf
PDF

> this is a plot of a kilonova model at 200 Mpc
> the luminosity might be optimistic, but if true, it would be around 17 at 50 Mpc

foley 1:35 PM
thats i = 17

at +1 day

@ckilpatrick we are about 2 hours from starting observations — it would be good to talk about reductions

the most important thing is to get things to a place where we can blink things

and we should try to do that on the ~1 minute timescale

so we can keep up with the data stream

if that means looking at the individual chips, thats fine

we can even look at raw data if necessary

but since all of the data might be hard for us to access, you (and cesar?) might have to do things more manually

but we should get reference images ready now

dss works, and you can download them directly in ds9

but i think there are decam images, and those would be better

ckilpatrick 1:44 PM
ok, do you want me to download reference images and upload them or are you going to do that?

foley 1:44 PM
once things set in chile (nobody can get a spectrum), we can go to a slower version

it depends on what you think is going to be tractable

if only people in santa cruz can search, then you should just download

but maybe @msiebert can get you a link

Message gw170817

gw170817

7 | *Add a topic*

Search

ckilpatrick 1:45 PM
what's the total area of the region you're searching?

foley 1:45 PM
if you can quickly upload data to somewhere we can grab it, we can also search
for the real time, we will just look at the big galaxies, blinking, looking for obvious things
this is really just to get something in case we can get a spectrum
we have both magellans at our disposal
theres also a gemini south program

ckilpatrick 1:47 PM
ok, I can just sit on this
we'll get everything ready on our end

foley 1:47 PM
great
so if you can do bias subtraction/flattening/stitching in <1 minute, that might be good to do
and we should process things even if we are looking at the raw data
we will do a more careful job after all of the data are taken
on a separate note, i know photpipe has been set up to reduce imacs data
we should talk to ben about his plans for reducing/searching the data

ckilpatrick 1:50 PM
ok, I'll set that up
where is the new schedule? all I'm seeing right now is the 3 minute g band tiles
I thought we were doing the GRB field, and in i band
I dont know what fields we're doing right now

foley 1:53 PM
good point
we dont have that yet
but it is the ~10 deg^2 from the ligo circular

ckilpatrick 1:54 PM
are we doing g+i or just i band?

foley 1:54 PM
i think just i

ckilpatrick 1:54 PM
ok, I'll start downloading DECam data

foley 1:54 PM
unless the galaxy catalog is very small and we can do multiple passes

Message gw170817

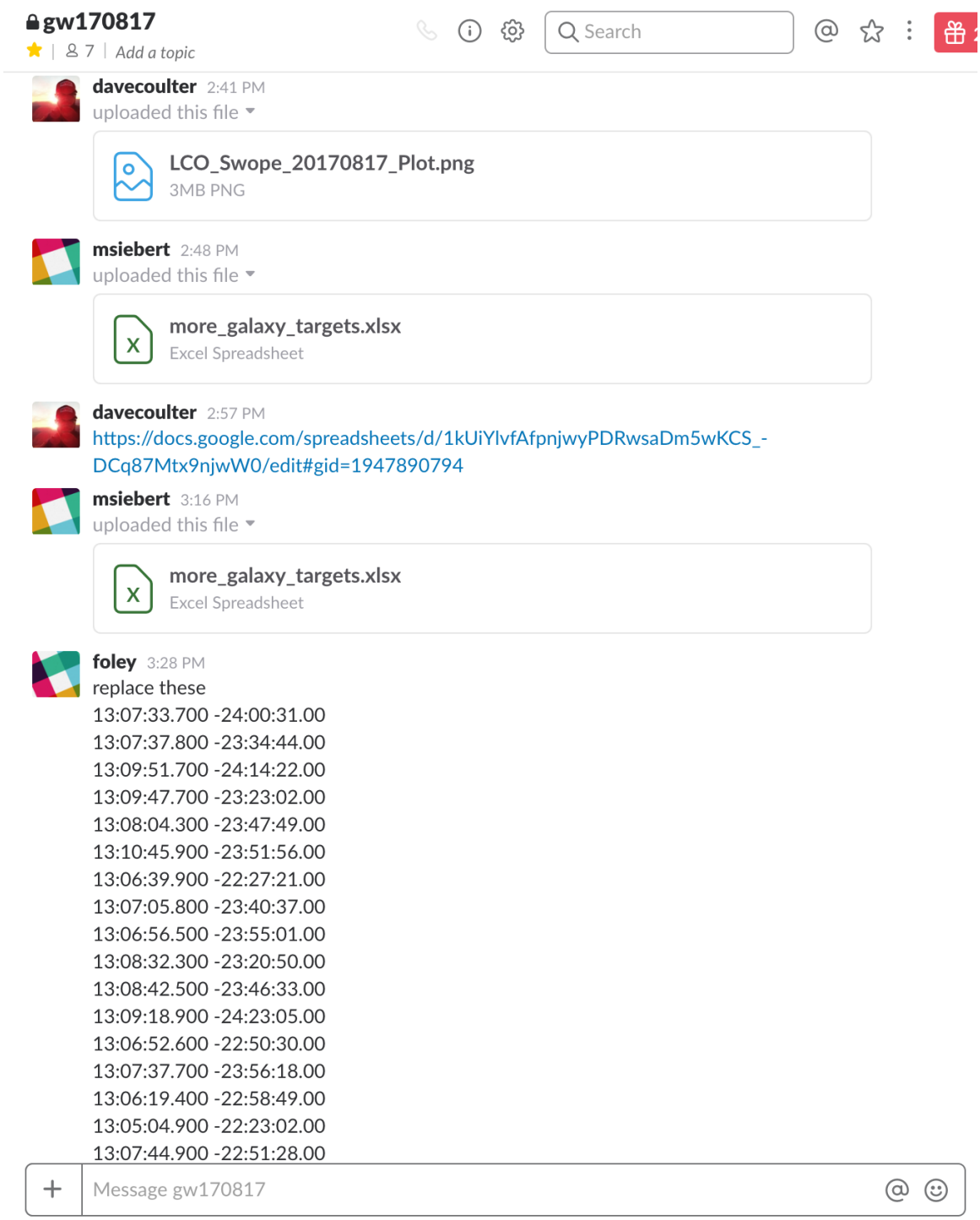
gw170817
7
Add a topic
Search
davecoulter 2:41 PM
uploaded this file
LCO_Swope_20170817_Plot.png
3MB PNG
msiebert 2:48 PM
uploaded this file
more_galaxy_targets.xlsx
Excel Spreadsheet
davecoulter 2:57 PM
https://docs.google.com/spreadsheets/d/1kUiYlvfAfpnjwyPDRwsaDm5wKCS_-DCq87Mtx9njwW0/edit#gid=1947890794
msiebert 3:16 PM
uploaded this file
more_galaxy_targets.xlsx
Excel Spreadsheet
foley 3:28 PM
replace these
13:07:33.700 -24:00:31.00
13:07:37.800 -23:34:44.00
13:09:51.700 -24:14:22.00
13:09:47.700 -23:23:02.00
13:08:04.300 -23:47:49.00
13:10:45.900 -23:51:56.00
13:06:39.900 -22:27:21.00
13:07:05.800 -23:40:37.00
13:06:56.500 -23:55:01.00
13:08:32.300 -23:20:50.00
13:08:42.500 -23:46:33.00
13:09:18.900 -24:23:05.00
13:06:52.600 -22:50:30.00
13:07:37.700 -23:56:18.00
13:06:19.400 -22:58:49.00
13:05:04.900 -22:23:02.00
13:07:44.900 -22:51:28.00
Message gw170817

gw170817

7 | Add a topic

Search

with
12:51:03.187 -14:24:04.47
12:49:57.432 -14:32:02.75
12:52:52.738 -15:28:43.23
12:54:11.615 -15:58:49.24
12:56:13.260 -17:11:07.76
12:56:46.736 -19:29:16.53

@ckilpatrick these will be the most important fields for searching
each has at least 2 galaxies, and a few have ~9

ckilpatrick 3:41 PM
ok, understood

foley 3:42 PM
added and commented on this Plain Text snippet: **gw_gal.reg**

```
1  # Region file format: DS9 version 4.1
2  global color=green dashlist=8 3 width=1 font="helvetica 10 normal roman" select=1
   highlite=1 dash=0 fixed=0 edit=1 move=1 delete=1 include=1 source=1
3  fk5
4  circle(12:57:27.9    ,-19:41:29.0,30")
```

> region file containing all of the galaxies on current schedule

foley 3:42 PM
there is a region file

you can just load that into any image and you should be able to see the galaxies that we care about

ckilpatrick 3:43 PM
thanks

foley 3:54 PM
replace
13:07:33.700 -24:00:31.00
13:07:37.800 -23:34:44.00
13:08:04.300 -23:47:49.00
13:07:05.800 -23:40:37.00
13:06:56.500 -23:55:01.00
13:08:42.500 -23:46:33.00
13:07:37.700 -23:56:18.00
13:08:42.000 -24:22:58.00
13:09:17.700 -24:22:56.00
13:07:34.100 -23:48:54.70

with

Message gw170817

gw170817

7 | Add a topic

Search

foley 4:04 PM
for clay,
replace
12:57:27.900 -19:41:29.00
12:52:25.600 -15:31:02.00
12:52:51.100 -15:29:30.00
12:52:29.400 -15:29:58.00
12:52:33.000 -15:31:00.00
12:52:27.400 -15:31:07.00
12:57:32.700 -19:42:01.00
13:07:33.700 -24:00:31.00
13:07:37.700 -23:56:18.00

with
12:52:38.937 -15:30:23.44
12:57:30.282 -19:41:53.01
13:07:36.044 -23:58:37.89

(that's everything)

ckilpatrick 4:14 PM
we're all set for the first few images here

foley 4:19 PM
fantastic

foley 4:21 PM
added and commented on this Plain Text snippet: **gw_gal.reg**

```
1  # Region file format: DS9 version 4.1
2  global color=green dashlist=8 3 width=1 font="helvetica 10 normal roman" select=1
   highlite=1 dash=0 fixed=0 edit=1 move=1 delete=1 include=1 source=1
3  fk5
4  circle(12:57:27.9    ,-19:41:29.0,30")
```

> updated region file

foley 4:21 PM
there are duplicates, but this includes all of the things @davecoulter added after we consolidated

@ckilpatrick @davecoulter it would be great if we could update individual galaxy coordinates so when we slew it falls in the center of a chip rather than in the middle of all 4 chips

davecoulter 4:24 PM
@ckilpatrick Do you have a script that can update a target coordinate with an offset to c3?

I can write one, but I don't want to make a mistake and slew off in the wrong direction

ckilpatrick 4:25 PM
no, you'll need to convert back and forth between sexagesimal and degree notation

Message gw170817

gw170817

7 | Add a topic

Search

ckilpatrick 4:25 PM
no, you'll need to convert back and forth between sexagesimal and degree notation

davecoulter 4:26 PM
OK

Honestly, I think it is safer for them to offset like normal

OK, we'll do that

foley 4:27 PM
@ckilpatrick when you get a chance, please verify that i didnt completely mess up those pointings and that we have multiple galaxies in those first pointings

ckilpatrick 4:28 PM
there are 4

galaxies

foley 4:28 PM
great!

ckilpatrick 4:28 PM
nothing im fields12

foley 4:29 PM
no transients, right?

ckilpatrick 4:29 PM
no transients

sorry, image is fine

foley 4:29 PM
fantastic

ckilpatrick 4:29 PM
but nothing I can see by eye

davecoulter 4:34 PM
uploaded this file

LCO_Swope_20170817_Plot.png
3MB PNG

ckilpatrick 4:38 PM
ok, nothing in fields10

there was a bug in fields11 that we just fixed, but we're going back to that one

nothing in fields11

ckilpatrick 4:59 PM
@foley found something

Message gw170817

gw170817

7 | *Add a topic*

Search

ckilpatrick 4:59 PM
@foley found something
sending you a screenshot

foley 4:59 PM
wow!

davecoulter 4:59 PM
!

ckilpatrick 4:59 PM
template

ckilpatrick 4:59 PM
uploaded this image: Screen Shot 2017-08-17 at 4.59.27 PM.png

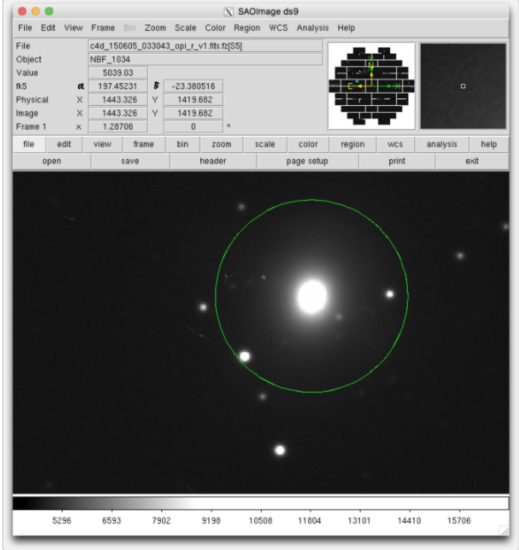

ckilpatrick 5:00 PM
us

ckilpatrick 5:00 PM
uploaded this image: Screen Shot 2017-08-17 at 4.59.53 PM.png

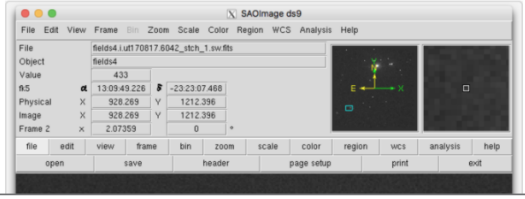

Message gw170817

gw170817

7 | *Add a topic*

Search

ckilpatrick 4:59 PM
uploaded this image: **Screen Shot 2017-08-17 at 4.59.27 PM.png**

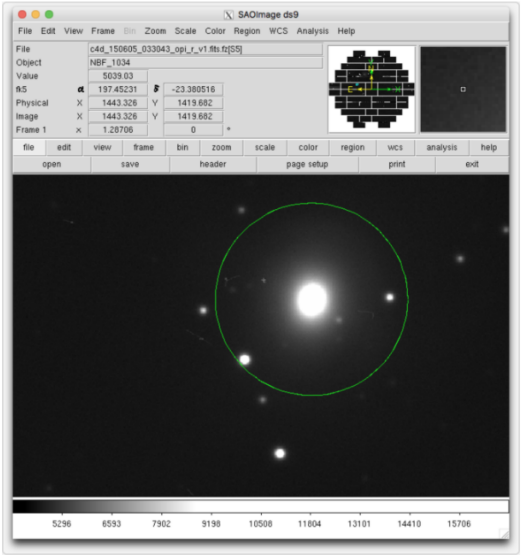

ckilpatrick 5:00 PM
us

ckilpatrick 5:00 PM
uploaded this image: **Screen Shot 2017-08-17 at 4.59.53 PM.png**

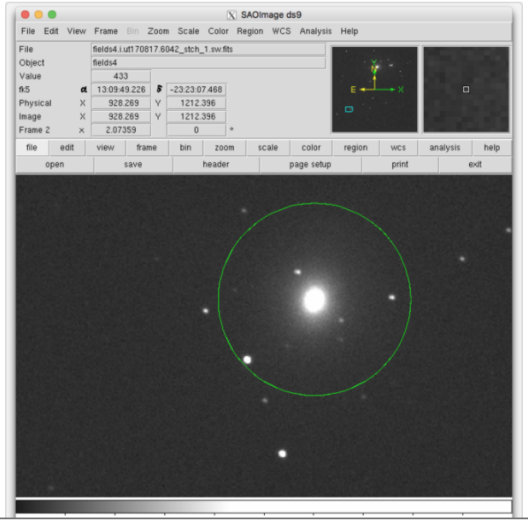

Message gw170817

gw170817

7 | Add a topic

Search

ckilpatrick 5:00 PM
uploaded this image: Screen Shot 2017-08-17 at 4.59.53 PM.png

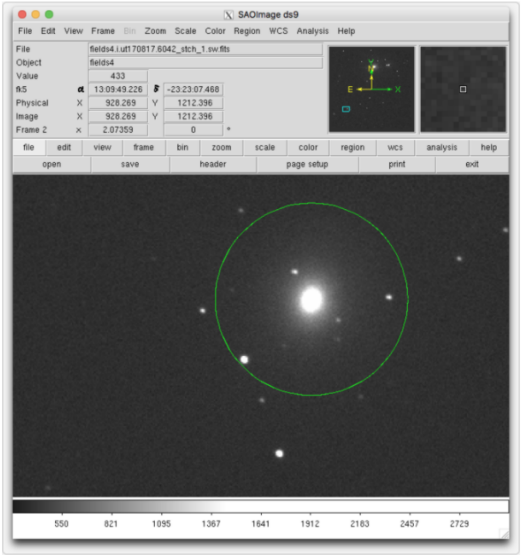

foley 5:00 PM
yep!

coorindates so we can check minor planet

and spectrum!

ckilpatrick 5:00 PM
13:09:47 -23:23:01

that's rough

let me tighten it up

13:09:48.089 -22:23:53.35

foley 5:02 PM
@ckilpatrick can you do the minor planet check?

ckilpatrick 5:02 PM
sorrty

-23:22:53.35

yes

nothing in MPC

@foley

foley 5:04 PM

Message gw170817

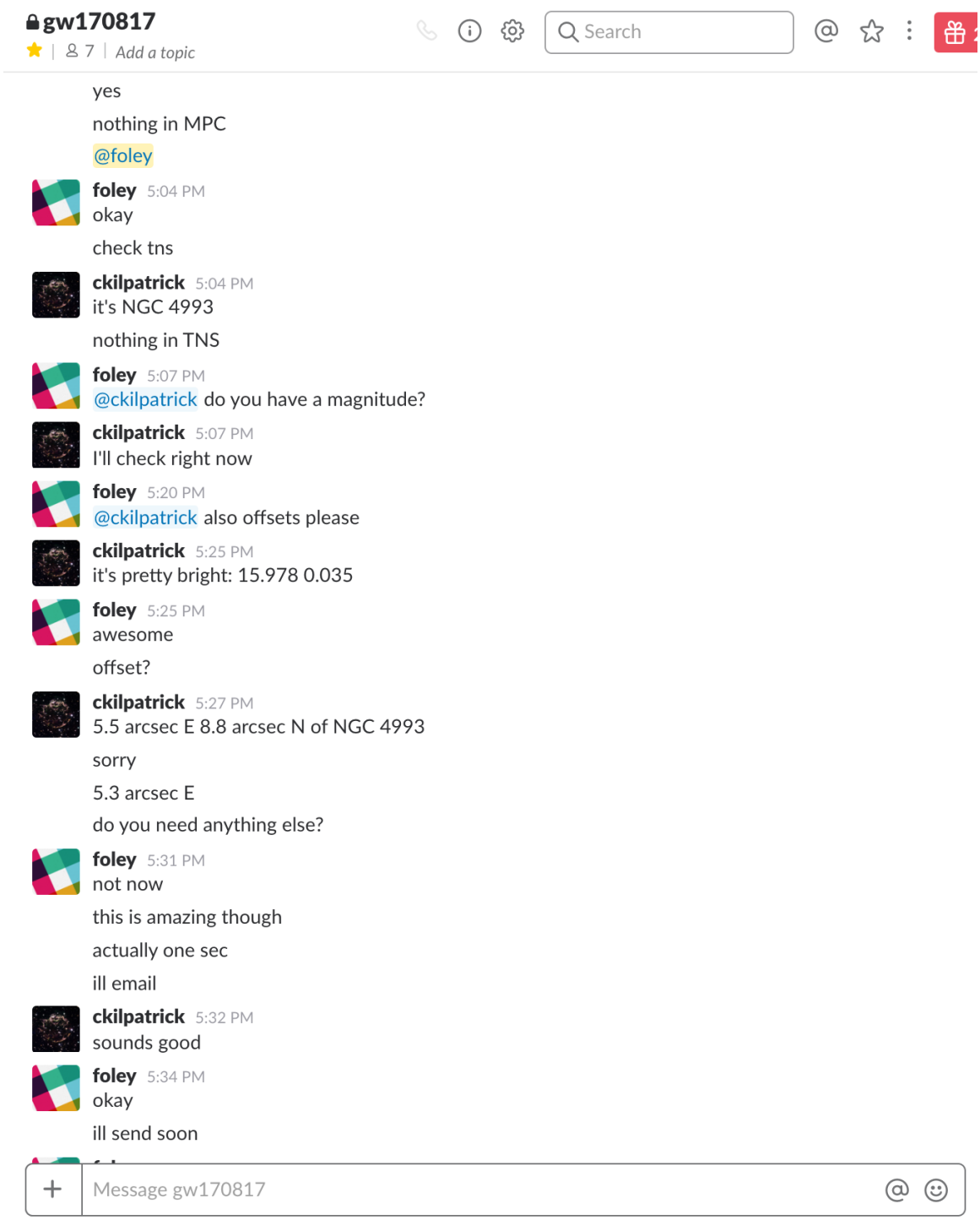

Figure 3.8 1M2H Slack conversation related to GW170817/SSS17a.

Chapter 4

The Gravity Collective: A Comprehensive Analysis of the Electromagnetic Search for the Binary Neutron Star Merger GW190425

4.1 Introduction

The mergers of neutron stars (NS) and black holes (BH) produce sufficiently strong gravitational waves (GWs) that they can be detected by modern interferometric instruments

such as the Laser Interferometer Gravitational Observatory (LIGO) and Virgo (Abbott et al. 2016c,e, 2017b,e,c). The majority of detected GW events involve binary black holes (BBHs; The LIGO Scientific Collaboration et al. 2021), systems that are naively expected to produce no electromagnetic (EM) emission. However, The LIGO-Virgo-KAGRA (LVK) collaboration has detected eight mergers of compact binaries where at least one component has a mass consistent with being a NS (e.g., a component ≤ 3 $M_\odot$; Abbott et al. 2021a; The LIGO Scientific Collaboration et al. 2021). In these cases, there is the potential for an electromagnetically luminous counterpart either as a short gamma-ray burst (sGRB) or a radioactive kilonova (KN; Li & Paczyński 1998; Shibata & Taniguchi 2006; Metzger et al. 2010).

A single GW event, GW170817 (Abbott et al. 2017a), was also observed in light as GRB 170817A (Goldstein et al. 2017; Savchenko et al. 2017) and SSS17a/AT 2017gfo (Coulter et al. 2017a). This event was the result of the merger of two roughly equal-mass NSs with component masses of $1.46^{+0.12}_{-0.10}$ and 1.27 ± 0.09 $M_\odot$ and a total mass of $2.73^{+0.04}_{-0.01}$ $M_\odot$. The ultraviolet (UV), optical, and infrared (IR; collectively denoted as UVOIR) data are consistent with a radioactively powered KN with 0.06 $M_\odot$ of ejecta that is rich in r-process material (Arcavi et al. 2017a; Cowperthwaite et al. 2017; Drout et al. 2017; Kasliwal et al. 2017; Kilpatrick et al. 2017; Smartt et al. 2017; Soares-Santos et al. 2017). The GRB and its afterglow, observed as a non-thermal component for several years (Haggard et al. 2017; Margutti et al. 2017; Alexander et al. 2018; Lyman et al. 2018; Margutti et al. 2018; Nynka et al. 2018; Pooley et al. 2018; Ruan et al. 2018; Troja et al. 2018; Fong et al. 2019; Hajela et al. 2019; Piro et al. 2019; Troja et al. 2019, 2020; Makhathini et al. 2021; Hajela et al. 2022; Kilpatrick et al. 2022a), are consistent with a structured jet with an opening angle of $\sim5^\circ$ pointed $\sim20^\circ$ from our line of sight.

Of the eight compact-binary mergers with a possible NS that the LVK has detected through its third observing run (O3), five have one component that is a BH (i.e., a neutron star-black hole merger, NSBH) and a mass ratio where the secondary component (if a NS) would be disrupted inside the event horizon, precluding electromagnetic emission similar to that of GW170817.

Besides GW170817, the only other BNS merger yet detected is GW190425 (Abbott et al. 2020c). GW190425 consisted of a $2.02^{+0.58}_{-0.34}$ and 1.35 ± 0.26 $M_\odot$ NS with a total mass of $3.4^{+0.3}_{-0.1}$ $M_\odot$, although it cannot be ruled out that either component was in fact a BH using only GW data. Unfortunately, GW190425 was a "single-detector" event, only observed by the LIGO Livingston detector. As a result, its initial (final) localization was constrained to $10,183$ deg^2 ($9,881$ deg^2) at 90% confidence, covering roughly one quarter of the sky. Additionally, its high total mass implies a KN that is fainter and redder than AT 2017gfo (Foley et al. 2020). Because a large fraction of the localization region was close to the Sun, no observatory could practically observe the entire localization region. Moreover, the size of the localization region and its extent over both hemispheres meant multiple telescopes were necessary to cover the maximum area possible.

Starting 15.5 hours after the trigger, we observed portions of the GW190425 localization region using four small-aperture telescopes as part of the One-Meter, Two-Hemispheres (1M2H) team. At the same time, several other teams, including GRANDMA, GROWTH, GOTO-4, SAGUARO, and others, began their own observing campaigns (Coughlin et al. 2019; Hosseinzadeh et al. 2019; Lundquist et al. 2019; Antier et al. 2020; Gompertz et al. 2020). Each facility has different capabilities in aperture, field of view, and location. Additionally, strategies

related to choosing pointings, filters, and cadence resulted in a heterogeneous, but vast data set. No candidate counterpart has been reported with high confidence in these data (though see Moroianu et al. 2023, for discussion of a low-significance fast radio burst counterpart), and the possible emission from a KN or sGRB has been limited by the multiple analyses from the above individual teams on their separate datasets.

A combined analysis will clearly result in better constraints than analyses of subsets of the full dataset. Here, we present our UVOIR search for an EM counterpart to GW190425 and combine those data with previously published data in Section 4.2. We find no viable optical counterparts in this combined dataset or reported counterparts from other facilities, and describe our candidate vetting process in Section 4.3. We introduce `Teglon`[30,31], a new, open-source tool for optimizing EM search and performing pixel-level upper limits calculations in Section 4.4 and Appendix 4.11. In Section 4.5, we demonstrate how `Teglon` transforms GW190425's localization, providing a boost in efficiency to small field of view (FOV) instruments. Using `Teglon`, we perform a sophisticated analysis of the limits of all observations that accounts for the recovery of artificial sources in each image (when available), line-of-sight extinction, the three-dimensional probability from GW data, and additional consideration for galaxy catalogs and their three-dimensional completeness, resulting in the most comprehensive KN, sGRB, and model-independent constraints on the UVOIR emission from GW190425 in Section 4.6. Finally, we discuss these results in the context of the LVK's current (i.e., fourth; O4) and future observing runs (O5+), and how future observational campaigns can adjust to improve our chances of discovering the next GW counterpart, along with a broader discussion of our analysis

[30] https://github.com/davecoulter/teglon_O4
[31] https://anathem.fandom.com/wiki/Teglon

methods and prospects for improving the localizations of GW events based on contextual data in Section 4.7.

Throughout this paper, we adopt a flat λCDM cosmology with the following parameters: $H_0 = 100h = 70$ km s^{-1} Mpc^{-1}, $\Omega_{\rm M} = 0.27$ and $\Omega_\lambda = 0.73$.

4.2 Observations

GW190425 (initially denoted as S190425z in Ligo Scientific Collaboration & VIRGO Collaboration 2019) was initially reported to have a `BAYESTAR` (Singer & Price 2016) 90% credible localization of $10,183$ deg^2 and luminosity distance of 155±45 Mpc. These were later refined to a final localization of $9,881$ deg^2 and luminosity distance of 159^{+71}_{-69} Mpc (Abbott et al. 2020c). Because of this large area, we consider any data across the sky relevant if obtained within two weeks of 25 April 2019, including targeted search data for GW190425 and S190426c, a purported NSBH merger with a final localization of 1,393 deg^2 and a luminosity distance of 377±45 Mpc (Abbott et al. 2021a). Therefore, we include targeted search imaging data from the One-Meter Two-Hemispheres (1M2H) Collaboration, from Gravity Collective (GC) partner Las Cumbres Observatory (LCO), and publicly reported limits through the Treasure Map (TM) application (Wyatt et al. 2020) for both GW190425 and S190426c in our analysis. This TM data includes limits for both GW events from the Zwicky Transient Facility (ZTF; Bellm et al. 2019b), the Gravitational-wave Optical Transient Observer 4 telescope (GOTO-4; Steeghs et al. 2022), the *Swift* Ultra-Violet/Optical Telescope (Roming et al. 2005), the MLS 10K CCD camera via the Catalina Sky Survey (CSS; Christensen et al. 2018), and the MMT Cam via the Fred Lawrence Whipple Observatory (Williams 2018). In addition to these targeted search data, we

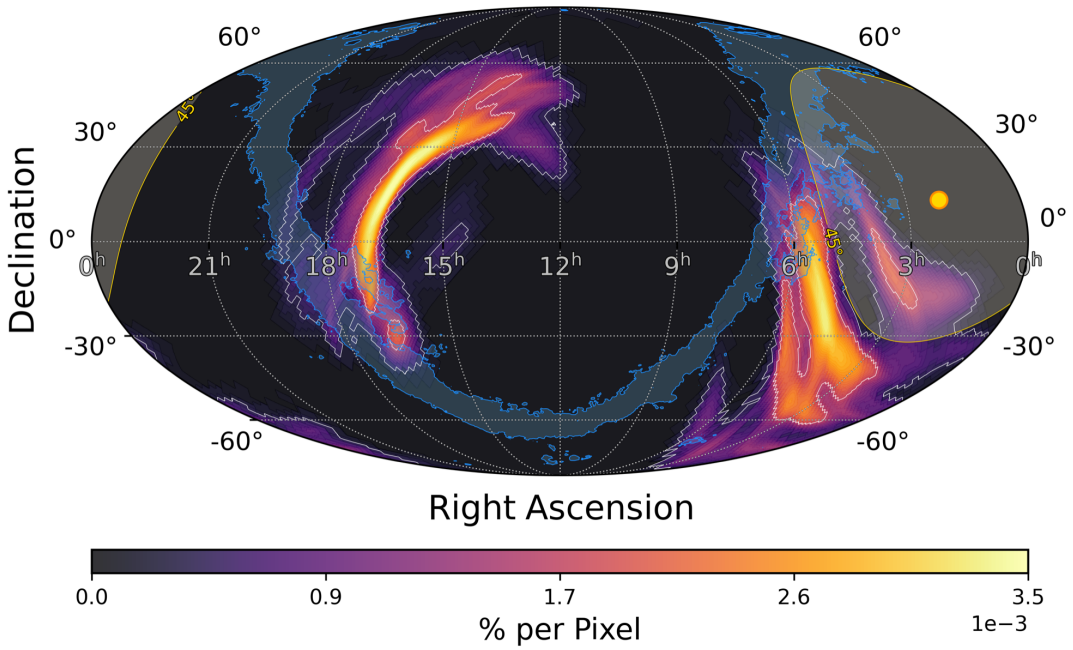

Figure 4.1 The LVC localization region for GW190425. Contours correspond to the 50th (2,400 deg^2) and 90th (9,881 deg^2) percentile region. In blue is the contour corresponding to the Milky Way r-band extinction of 0.5 mag. Near 3 hours of Right Ascension (R.A.) is the location of the Sun at sunset in Chile on April, 25th, 2019, with a Sun-separation contour of 45°.

also include untargeted imaging data across all 1M2H telescopes, collecting a total of 3,598 public and private pointings for this analysis, which cumulatively cover 36.78% of the two-dimensional (2D) probability and 39.58% of `Teglon`-redistributed probability (see Section 4.4 and 4.5) from the final maps presented in Abbott et al. (2020c).

4.2.1 One-Meter Two-Hemispheres Data

The One-Meter Two-Hemispheres (1M2H) Collaboration was established in 2017 and originally used two 1-m telescopes, the Nickel Telescope at Lick Observatory in California and the Swope Telescope at Las Campanas Observatory in Chile, to search for EM counterparts

to GW sources. In 2019 this collaboration was expanded to include the 0.7 m robotic Thacher telescope at the Thacher School Observatory in Ojai, CA (Swift et al. 2022), and the A Novel Dual Imaging Camera (ANDICAM; DePoy et al. 2003) on the SMARTS 1.3 m telescope at Cerro Tololo Interamerican Observatory, Chile. We present data from this collaboration for the first time and describe our reduction process and limits below.

ANDICAM

We observed galaxies in the localization region of GW190425 with the A Novel Dual Imaging Camera (ANDICAM; DePoy et al. 2003) on the SMARTS 1.3 m telescope at Cerro Tololo Interamerican Observatory, Chile. All observations were performed from 25–26 April 2019 as described in Table 4.10. ANDICAM enables simultaneous optical observations using a Fairchild charge-coupled device (CCD) array with a 10×10 arcmin^2 FOV and IR observations using a Rockwell HgCdTe array with a 3.3×3.3 arcmin^2 FOV. We searched the initial localization with the CCD and IR detectors to obtain I and H-band observations of 25 galaxies within the GW190425 90th percentile localization region and followed two optical candidates with a combined CCD + IR filter set of I, J, H, and K, respectively. All imaging for the CCD and IR detectors were reduced using `photpipe` (Rest et al. 2005), including bias-subtraction, dark corrections for the IR detector, and flat-fielding. The images were aligned using *Gaia* astrometric standards (Gaia Collaboration et al. 2021). We then performed photometry in each image using `DoPhot` (Schechter et al. 1993). Finally, the images were flux calibrated using Pan-STARRS DR2 photometric standards (Flewelling et al. 2020) transformed into I-band (following transformations in Jester et al. 2005) and 2MASS H-band standards (Skrutskie et al. 2006). We

obtained follow-up observations of each field to use as templates for subtraction from 5–11 June 2019. After processing each image using the methods mentioned above, we subtracted the reference images from our science frames using `hotpants` (Becker 2015). Final photometry for all transient sources in each difference image was obtained using a custom version of `DoPhot`.

Nickel

We observed galaxies in the localization region of GW190425 with the Direct 2k×2k ($6.8' \times 6.8'$) camera on the Nickel 1 m telescope at Lick Observatory, Mt. Hamilton, California. We performed targeted observations of candidate host galaxies in r-band from 26 April 2019 to 9 May 2019, and we include in our analysis untargeted $BVri$ observations in the same date range that are also within the GW190425 90th percentile localization region. All observations were reduced following the same procedure described above for ANDICAM CCD imaging, including image subtraction with templates obtained from 22 April 2018 to 10 May 2020 and forced photometry on all candidate optical counterparts using `DoPhot`.

Thacher

We observed GW190425 with the Andor 2k×2k camera (20.8' × 20.8') on the 0.7 m robotic Thacher telescope at the Thacher School Observatory in Ojai, CA (Swift et al. 2022). We include $griz$ follow-up data targeting the 90th percentile localization region of GW190425 obtained from 26 April 2019 to 4 May 2019. All imaging was reduced following the aforementioned methods and in Kilpatrick et al. (2021). We obtained template imaging of each field from 23 February 2019 to 6 August 2021. Our final observation list is given in Table 4.10.

Swope

We observed the localization region of GW190425 with the Direct 4k×4k camera (29.8' × 29.7') on the 1 m Swope telescope at Las Campanas Observatory, Chile. Our Swope observations consisted of targeted observations within the 90th percentile localization region of GW190425 in i-band obtained from 25 April 2019 to 9 May 2019 and untargeted $uBVgri$ observations within the same area and time frame. These data were reduced following the same ANDICAM/CCD procedures described above. We obtained template imaging from 16 August 2018 to 25 February 2020 to perform image subtraction in each frame and search for optical transients and generate forced photometry on known optical transients in each image.

SN 2019ebq and MOSFIRE

We obtained near-infrared (NIR) spectroscopy of the candidate counterpart to GW190425 SN 2019ebq on 2019 Apr 26, 14:32:11 UTC with the Multi-Object Spectrometer For Infra-Red Exploration (MOSFIRE; McLean et al. 2012) on the Keck I 10 m telescope. The spectrum was originally reported and described in Dimitriadis et al. (2019b). We reduced the spectrum following standard procedures using `spextool` and show the final reduced spectrum in Figure 4.2.1. Similar to findings in Dimitriadis et al. (2019b) and Nicholl et al. (2019), we classify this source as a SN Ib/c.

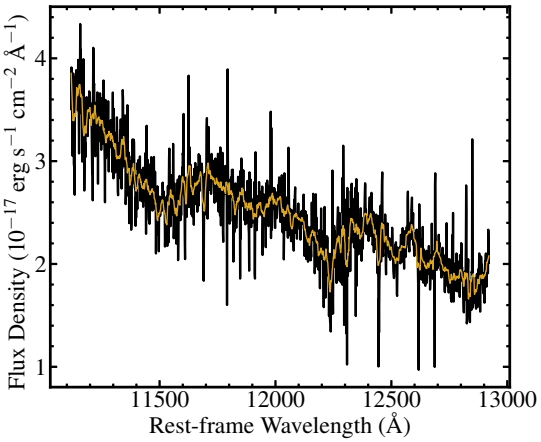

Figure 4.2 MOSFIRE NIR spectrum of SN 2019ebq, covering the J-band blueward of 12900 Å, obtained on 2019 Apr 26, 14:32:11 UTC on Keck I. The spectrum is consistent with a Type Ib/Ic supernova, and is therefore unrelated to the GW event (see 4.2.1; Dimitriadis et al. 2019b).

4.2.2 Gravity Collective Data

LCO

The Gravity Collective combines follow-up efforts by 1M2H and the Las Cumbres Observatory (LCO) Global Telescope network (Brown et al. 2013b), which includes fourteen 0.7-1 m telescopes distributed worldwide. LCO observed the localization region of both GW190814 and S190426c, with a galaxy-targeted search and prioritization strategy described in (Arcavi et al. 2017b). For both GW events, LCO obtained 773, 300 s exposures in *gri* using the Sinistro cameras (26' × 26' FOV) mounted on these telescopes (Keinan et al. (in prep.)). Image processing was performed by the LCO `BANZAI` pipeline (McCully et al. 2018), and limiting magnitudes were calculated using `LCOGTSNpipe` (Valenti et al. 2016). Sloan Digital Sky Survey (SDSS) (Abazajian et al. 2009), PS1 (Flewelling et al. 2020), or DECam (Abbott et al. 2018) template images were used in the science image bands to perform image subtraction using `PyZOGY`

(Zackay et al. 2016; Guevel & Hosseinzadeh 2017). The limiting magnitudes were calculated by calculating the Poisson noise due to the sky using the median absolute deviation of the entire image. The Poisson and read noise were combined, and the 3σ limiting magnitude (median limiting magnitude of 22.1 mag) was estimated by inverting the standard signal-to-noise (SNR) equation.

4.2.3 Public Data via Treasure Map

ZTF

ZTF is a 47 deg^2 FOV optical instrument on the Palomar 48-inch Schmidt telescope (Bellm et al. 2019b). We include 313 ZTF pointings reported to TM with a status of "completed" for GW events GW190425 and GW190426_152155, and whose image reduction process is outlined in (Coughlin et al. 2019). Pointings span g, r, and i-band, with a median r-band depth of $\approx$21.5 $m_{\rm AB}$. Within TM, each pointing includes the central coordinate of the field of view, filter, MJD of the observation, and limiting AB magnitude.

CSS

CSS operates the MLS 10K CCD camera on the Mt. Lemmon 1.5 m telescope, which has a $\sim$5 deg^2 FOV and that was used by the Searches after Gravitational Waves Using ARizona Observatories (SAGUARO) team to search for 17 GW events within O3 (Lundquist et al. 2019; Paterson et al. 2021). We include 61 pointings taken in an open filter to a median limiting mag of $\approx$21.3 $m_{\rm AB}$.

GOTO-4

The GOTO-4 telescope (Steeghs et al. 2022) is a prototype array of 4 telescopes with a combined FOV of ∼18 deg^2. The GOTO team searched for 29 gravitational wave event triggers in LIGO's third observing run (O3) (Gompertz et al. 2020), and we include 399 pointings that span g and V bands, with a median g-band depth of ≈19.8 $m_{\rm AB}$.

MMT

The 6.5 m MMT telescope at Fred L. Whipple Observatory in Arizona conducted a galaxy-targeted search with MMTCam for EM counterparts to both GW190425 and S190425c (Hosseinzadeh et al. 2019). We include 119 pointings in gi, with a median i-band depth of 21.9 $m_{\rm AB}$.

Swift

In O3, *Swift* searched 18 GW events using a galaxy-targeted approach (Evans et al. 2016), including GW190425 and S190426c, with the Ultra-Violet/Optical Telescope (Oates et al. 2021). These data include 1357 pointings for GW190425 and S190426c in u-band with a median limiting magnitude of 19.4 $m_{\rm AB}$. These data are particularly interesting as they cover a region of a parameter space which is unique given the other optical filters in this combined dataset.

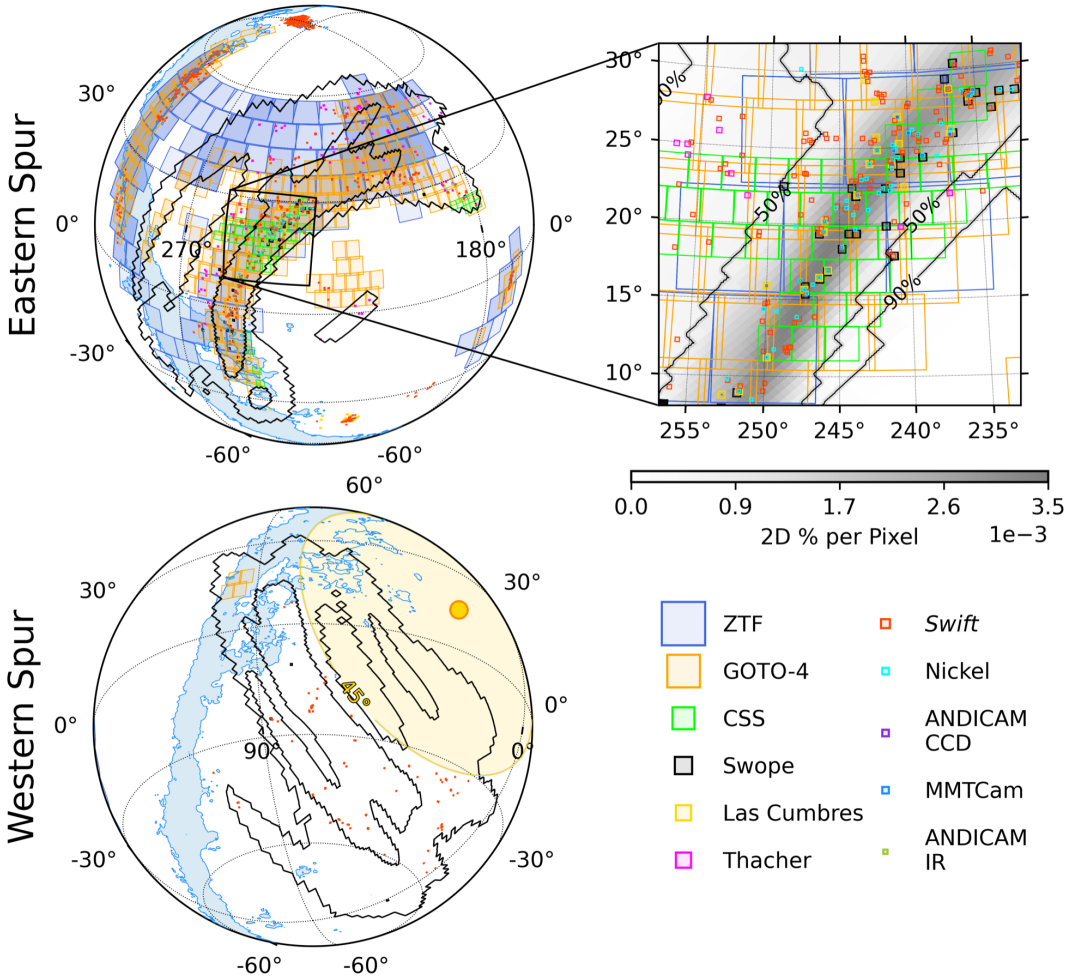

Figure 4.3 Visualization of the full EM search dataset for this work. In each orthographic projection, black contours correspond to the 50th/90th localization of GW190425, and Milky Way extinction is marked as a blue contour at $A_r = 0.5$ mag. Overplotted are all instrument FOVs: ZTF (dark blue), GOTO-4 (orange), CSS (lime green), Swope (black), Las Cumbres (yellow), Thacher (pink), *Swift* (red), Nickel (cyan), ANDICAM CCD (purple), MMTCam (light blue), and ANDICAM IR (dark green). *Upper Left* Close up of the Eastern Spur of probability as seen in Figure 4.1, R.A.$\in [95, 315]$ deg. Every instrument in our manifest has imaging in this hemisphere (3,270 total observations), covering 36.6% of the final LVC 2D probability. *Upper Right* A 12-deg radius zoom in on R.A. 245 deg, Declination (Decl.) +20 deg, showing a detailed view of the smaller FOV instruments. The grayscale gradient is the 2D probability of the localization, with the 50th/90th contours labeled. Many of these fields covered the same sky regions multiple times in the same filters and highlights an opportunity to coordinate EM follow-up efforts (see Section 4.7). *Lower Left* Close up of the Western Spur of probability as seen in Figure 4.1, R.A.$\in [0, 95]$ deg. Only GOTO-4, Swope, and *Swift* have observations in this hemisphere (328 total) due to this region being close to the Sun, contributing only 0.2% of the covered localization probability. A yellow Sun contour denotes a 45 deg separation that marks *Swift*'s pointing limits.

4.3 Candidates

4.3.1 1M2H Vetted Candidates

After subtracting templates from the ANDICAM, Nickel, Swope, and Thacher images, we identified candidate counterparts to GW190425 by searching for sources of positive emission in the difference images. We first ran `DoPhot` on the difference images, searching for sources detected at a signal-to-noise (S/N) threshold of $\geq 3\sigma$. We performed minimal filtering on the detected sources, particularly removing those where >30% of pixels inside the PSF aperture are negative or where >40% of pixels are masked. Apart from these cuts, we required only that a candidate transient is detected in a single image at our S/N threshold.

All candidates were then gathered by field into web pages with cutout images showing the candidate detection from every epoch, the scatter in candidate coordinates for each detection, and the difference light curve in terms of flux and magnitude. Members of the 1M2H collaboration all visually vet these web pages to rule out detections that appear consistent with artifacts such as a convolved cosmic ray, correlated noise across a bad section of each detector, dipole emission associated with a bright and poorly subtracted star, or a satellite or other moving object passing through the image frame.

We required that a candidate transient be flagged only by a single human vetter to elevate that source for our candidate analysis pipeline. Following analysis similar to Kilpatrick et al. (2021) and public candidates described below, we crossmatched the candidates to sources classified as stars by *Gaia* (point source score (PSS) >0.99 following the PSS value from Gaia Collaboration et al. 2021), were within $2''$ the location of a minor planet at the time of observation

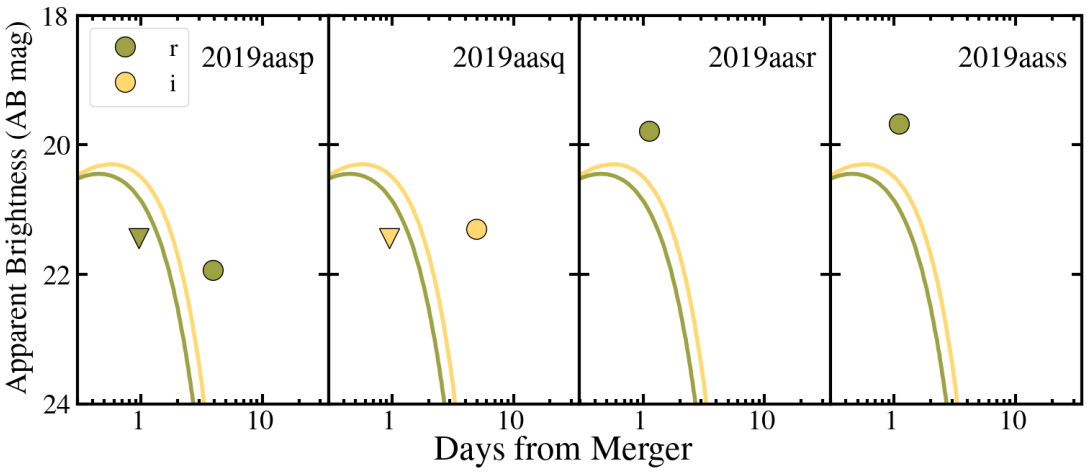

Figure 4.4 Photometry from the four candidate counterparts to GW190425 discovered within the localization region by 1M2H and described in Section 4.3.1. We show the time of detection as a circle in each panel, with green corresponding to r-band photometry and yellow corresponding to i-band photometry. For comparison, we overplot model kilonova light curves for a hypothetical event with ejecta mass 0.023 $M_{\odot}$, velocity 0.26 c, and an electron fraction $Y_e = 0.45$ as described in Section 4.6.1.

based on ephemeris from the Minor Planet Catalog[32], or were crossmatched to known, public transients in the Transient Name Server[33]. After these checks, we identified 4 novel candidate transients that were reported to TNS: AT 2019aasp, 2019aasq, 2019aasr, and 2019aass (Coulter et al. 2023b). These and all other candidate transients reported to TNS were then analyzed using methods described below. In Figure 4.4 we show photometry from candidates discovered by 1M2H in comparison to model kilonova light curves described in Section 4.6.1.

4.3.2 Public Candidates

We used our candidate analysis pipeline to vet candidate counterparts to GW190425 in the context of the final `bayestar` localization map, time discovered from merger, coincidence with likely stars or other known point sources and minor planets, spectral classification as

[32] https://minorplanetcenter.net
[33] https://www.wis-tns.org/

a transient type unlikely to be associated with a NS merger, association with a host galaxy outside the localization volume defined by the `bayestar` map, and photometric evolution that does not resemble a likely kilonova or afterglow counterpart. In general, these cuts follow the same methods described in Kilpatrick et al. (2021) and the examples implemented in Kilpatrick (2023). Here we summarize each step as:

1. Importation of candidates from our transient database `YSE-PZ` (Coulter et al. 2023a), which contains all transients and metadata contained in TNS.

2. We analyze only candidates discovered within the first 14 days after the coalescence time of GW190425 at 2019 April 25, 08:18:05 UTC as defined in Abbott et al. (2020c). Moreover, we only analyze candidates within the two-dimensional 95th percentile as defined by the final `bayestar` map of that event. These two initial cuts define our sample of 293 candidate counterparts analyzed in the remaining steps below.

3. We crossmatch to minor planets using the time of discovery and coordinates of each candidate and using the Minor Planet Checker[34]. Any source found within $2''$ of a known minor planet at the time of observation is ruled out. In total, 2 candidates were ruled out by this check.

4. We crossmatch to point sources within the *Gaia* (Gaia Collaboration et al. 2021) and Pan-STARRS DR2 catalogs (Flewelling et al. 2020). For *Gaia*, this involves checking for sources aligned within $2''$ of a source with point-source score >0.99, while for Pan-STARRS we check for candidates within $2''$ of a source classified as point-like by the PS1 detection

[34] https://cgi.minorplanetcenter.net/cgi-bin/checkmp.cgi

flagging algorithm[35]. 4 candidates were ruled out for coincidence with *Gaia* sources while no candidates were ruled out due to coincidence with Pan-STARRS sources.

5. For candidates with spectroscopic follow up, we rule out candidates with a spectral classification that is inconsistent with a kilonova or gamma-ray burst afterglow. For GW190425, this sample comprises sources classified in TNS as a cataclysmic variable (CV), SLSN, SN Ia, SN Ib, SN Ic, SN II, and SN IIn, which are known to arise from progenitor systems other than NS mergers. 32 candidates were ruled out based on their spectral classifications.

6. We rule out candidates with pre-merger activity within 2″ of the transient location based on a positive detection using forced photometry in the ASAS-SN (Kochanek et al. 2017). We did not rule out any candidates in this way.

7. We rule out candidates that are outside the 95th percentile localization volume defined by the final `bayestar` localization map and located in a host galaxy with a spectroscopic redshift from the NASA/IPAC Extragalactic Database (NED)[36] or a photometric redshift from the PS1-STRM (Beck et al. 2021), Photometric Redshifts for the Legacy Surveys (Legacy; Zhou et al. 2021), or 2MASS Photometric Redshift (2MRS; Bilicki et al. 2014) catalogs. In this way, we ruled out 82 candidates.

8. Finally, we rule out candidates with photometry whose absolute magnitude, decline rate, or color evolution appears inconsistent with kilonova or afterglow emission. The details of this calculation are described in Kilpatrick et al. (2021). At this stage, there remained 173 viable candidates, of which we ruled out 56 due to photometric evolution inconsistent

[35] https://outerspace.stsci.edu/display/PANSTARRS/PS1+Detection+Flags
[36] http://ned.ipac.caltech.edu/

with being a counterpart to GW190425. There remain 117 viable candidate counterparts. We leave a detailed analysis of these candidate counterparts and the viability of their association with GW190425 for future work.

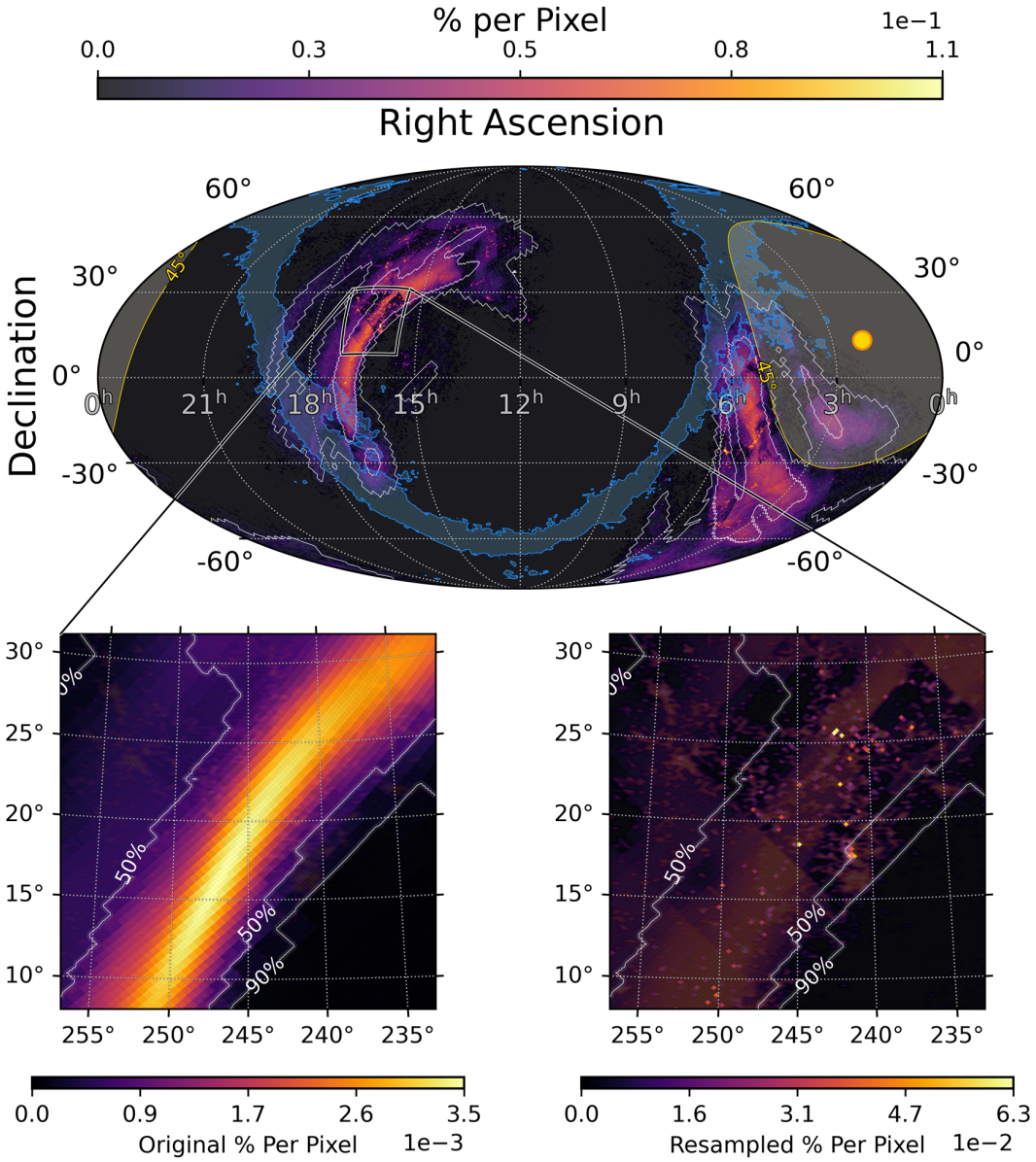

Figure 4.5 *Top* The localization map resampled by `Teglon`. At GW190425's distance, `Teglon` redistributes half of the total 2D probability to the highest probability galaxies (see Section 4.5). A 12-deg radius zoom panel is marked by a square centered on R.A. 245 deg, Decl. +20 deg. All other attributes are the same as Figure 4.1. *Bottom Left* For comparison, we show a zoom in of the original localization map with white contours denoting the original 50th/90th localization. Within the bounding box of R.A. $\in [235, 255]$ deg and Decl. $\in [10, 30]$ deg, there is $\sim$8.2% of the localization probability within $\sim$377 deg^2. *Bottom Right* The same zoom-in region with `Teglon`'s redistribution algorithm (matching the top plot). The same amount of probability ($\sim$8.2%) is covered in only $\sim$100 deg^2 increasing the coverage efficiency by a factor of $\sim$ 3.8.

4.4 Teglon

One effective method for localizing the EM counterparts to GW sources is to target the bright/massive galaxies residing in the locus of high probability within a GW localization volume (Kanner et al. 2012; Gehrels et al. 2016). This technique relies on two key factors: a galaxy catalog that is relatively complete at the ranges where GW sources are likely to be detected, and localization regions that are small enough to be efficiently searched with ground-based telescopes. To date, several catalogs have been used in GW follow-up (Kopparapu et al. 2008; White et al. 2011; Dálya et al. 2018, 2022; Cook et al. 2023), still they all specifically contain position, distance, and B-band magnitudes. B-band is used in particular because the rate of BNS mergers is expected to follow the rate of star formation (SFR) in the local universe, and B-band is a convolution of this SFR with a galaxy's total stellar mass (Phinney 1991; Belczynski et al. 2002). In 2017, this technique led to the discovery of the first optical counterpart, AT 2017gfo, (Coulter et al. 2017a) to a GW source, GW170817. GW170817 was the first-ever BNS merger detected in GWs and was localized to an area of 31 deg^2 and a luminosity distance of 40^{+8}_{-14} Mpc (Abbott et al. 2017a). In searching for this counterpart, 1M2H used the Gravitational Wave Galaxy Catalogue (GWGC), which at 40 Mpc is nearly 100% complete when compared to a Schechter galaxy luminosity function (Schechter 1976) for galaxies with a characteristic luminosity of ≤ -20.3 mag.

However, as the LVK has improved the GW network detection sensitivity (Abbott et al. 2016b), these catalogs and techniques have become less effective. In O3, the median BNS inspiral range was ∼108-135 Mpc (Abbott et al. 2021a). For BNS mergers with a total mass >2.8 $M_\odot$, or face-on mergers, the detection distance may be much larger. To this point,

GW190425 was a uniquely massive BNS merger at $3.4^{+0.3}_{-0.1}$ $M_\odot$, and was detected at a luminosity distance of 159^{+69}_{-71} Mpc (Abbott et al. 2020c). At this distance, the Galaxy List for the Advanced Detector Era (GLADE; Dálya et al. 2018) catalog is only ∼50% complete, meaning that a naive approach of simply targeting bright galaxies in the catalog would miss half of the galaxies in the volume. Despite this, as BNS detection ranges increase, the surface density of galaxies in projection increases so that any field of view should contain many galaxies (both cataloged and uncataloged). Naively, a pure tiling approach to searching for a counterpart is more effective at larger distances, but this picture is complicated by inhomogeneous galaxy catalog coverage. Intelligently trading off between these two approaches — to use our knowledge of where galaxies are to target them and to tile the localization region when we do not — motivates the creation of a new tool called `Teglon`. A detailed treatment of how `Teglon` transforms GLADE, implements its completeness weighting, and calculates its pixel-level upper limits is given in Appendix 4.11.

4.5 GW190425 Transformed By `Teglon`

`Teglon`'s EM search optimization depends on two properties: the B-band luminosity completeness of its volume pixels, or voxels, in the GW localization volume (see Appendix 4.11.1 and 4.11.2 for a complete description), and how much area that GW localization volume subtends on the sky in projection. Completeness is largely dictated by the average luminosity distance to an event; however, in regions of high galaxy catalog completeness (e.g., SDSS Stripe 82 (Annis et al. 2014) or the survey footprint of 2dF (Colless et al. 2001)), `Teglon`'s algorithm can still be effective at redistributing probability in the original GW localization to high-probability galaxies, thereby reducing the area an instrument needs to search. However, the area in projection of

a GW localization also matters — if the area subtended by a GW localization fits within the FOV of a search instrument, redistributing probability on scales smaller than the FOV would not change the search strategy. In the edge case of 0% completeness, or very small projected areas, `Teglon`'s optimization is identical to a pure tiling pattern of the high probability region.

The localization of GW190425 is a quintessential use case for `Teglon`. Because this event was only detected by the LIGO Livingston detector, its location was constrained to nearly a quarter of the sky ($9,881$ deg^2). However, despite this large area, the distance was relatively close at 159 Mpc (Abbott et al. 2020c). At this distance, the GLADE catalog is on average $\sim$50% complete, and therefore `Teglon` redistributed half of the localization probability to galaxies at the correct distance. This resampling reduces the 90th percentile localization to $6,674$ deg^2, a factor of ~ 1.5. Figure 4.5 shows the resulting localization, with insets that highlight this updated concentration of probability.

Table 4.1 shows a synoptic view of the effect `Teglon` has on the search efficiency increase, η, for each instrument in the dataset. η is markedly enhanced for detectors with FOVs ≤ 1 deg^2. In general, these instruments followed a galaxy-targeted approach, and due to the high completeness of GLADE with respect to GW190425's localization, the redistributed map provided by `Teglon` confirmed that these galaxies were in regions of the sky more likely to host the progenitor of the GW event. For this particular event, 3,402 of the original map pixels (≈ 178 deg^2) had their probability values boosted $\geq 10\times$ over their original values, and constitute 16% of the total probability in the map.

For this dataset, while all instruments have $\eta \geq 1.0$, instruments with FOVs ≥ 1 deg^2 saw diminishing returns due to the fact that their large footprint on the sky allowed them to

Table 4.1. GW190425 Search Synopsis

Search Instrument	FOV (deg^2)	# of Images	Total 2D Prob. $\sum_i P_{2D_i}(\%)$	Total Redistributed Prob.[a] $\sum_i P''_{2D_i}(\%)$	Efficiency Increase $\eta \equiv \sum_i \frac{P''_{2D_i}}{P_{2D_i}}$
ANDICAM IR	0.0015	21	0.04	0.46	11.36
MMTCam	0.0020	119	0.15	1.00	6.44
ANDICAM CCD	0.0111	27	0.06	0.62	10.39
Nickel	0.0438	138	0.19	0.92	4.98
Swift	0.0803	1357	0.72	3.84	5.32
Thacher	0.1200	186	0.09	0.42	4.54
Las Cumbres	0.1951	773	0.35	1.42	4.02
Swope	0.2459	204	0.59	1.87	3.19
CSS	4.9997	61	6.15	6.98	1.13
GOTO-4	18.1300	399	30.48	32.01	1.05
ZTF	46.7253	313	28.99	30.40	1.05
All Tiles	**5638**[b]	**3598**	**36.78**	**39.58**	**1.08**

Note. — A synopsis of `Teglon`'s effect on the community's combined EM search campaign for GW190425. `Teglon` strongly enhances η for instruments with FOVs ≤ 1.0 deg^2, see Section 4.5.

[a]See Appendix 4.11 for a full description.

[b]Total unique area covered by all observations.

simply tile the entire Western Spur of the localization (see Figure 4.3). Because of this, the survey footprint of these instruments encompassed both the pixels where probability was being concentrated and the voids left in between, resulting in η approaching unity. However, in the maximal case where a GW event subtends the entire sky but is detected at a distance where GLADE is 100% complete (e.g., at the distance of GW170817; 40 Mpc), `Teglon` would be useful for even the largest FOV instruments.

4.6 Model Comparisons

Based on the results of Section 4.3.2, we assume that there are no credible EM candidates for GW190425, and interpret the image depth for the data presented in Table 4.10 and in the Treasure Map (described in Section 4.2) as limits on a few classes of hypothetical EM

counterparts to a BNS merger. To make this physically meaningful, we assume (and in the case of the data in Table 4.10, *know*) that the data is homogeneous in that (1) each datum is the result of subtracting an in-band template image from the search image using the same instrument configuration, and (2) the reported depth of each image was computed by estimating the $\geq 3\sigma$ limiting magnitude from the difference image. We perform the joint model detection efficiency calculation, combining all reported epochs, depths, and filters, using the formalism described in Appendix 4.11.3. The maximum probability to detect any model is limited by the total amount of probability that the full dataset covers; therefore, we report our detection probability in two ways: (1) as the probability calculated by Equation 4.18, and (2) as a percent of the total amount of probability reported in Table 4.1, 39.58%, i.e., $X\%$ ($\frac{X}{39.58}\%$). This relative detection efficiency characterizes the effectiveness of the observations themselves, assuming they could have covered the entire localization region.

4.6.1 Kilonovae

In 2017, the discovery of the EM counterpart to GW170817, AT 2017gfo (Coulter et al. 2017a; Abbott et al. 2016f), demonstrated that KNe are radioactive transients whose UVOIR light curves are powered by the radioactive decay of freshly synthesized heavy elements (Drout et al. 2017). A KN light curve's peak luminosity, color, and evolution timescale, therefore, depend on the amount of mass the merger ejected, $M_{\rm ej}$, the ejecta's expansion velocity, $v_{\rm ej}$, and the ejecta's opacity, κ (Arnett 1982). The exact value of κ is driven by the atomic structure of the specific chemical species, but in general, elements with atomic mass A > 140 have many millions of bound-bound line transitions so that their opacities are $>10\times$ that of Fe. This high opacity

increases the photon diffusion timescale (and therefore the light curve evolution timescale), and shifts the emission from the UV/optical to the IR (Kasen et al. 2013). Surprisingly, observations of AT 2017gfo showed that multiple ejecta components of different compositions (i.e., opacities) were required to accurately model its light curves (Kilpatrick et al. 2017).

Building these heavy elements requires the rapid ("r-") neutron-capture process, or r-process (Burbidge et al. 1957), which in turn requires an enormous flux of neutrons to proceed. This neutron richness is quantified by Y_e, which is the ratio of electrons to nucleons in the ejecta. A $Y_e = 0.5$ is an equal mix of protons and neutrons, and $Y_e = 0.2$ has $4\times$ the number of neutrons to protons. Therefore, Y_e can be used as a proxy for κ, and we adopt the models of Metzger (2017), which are parameterized in ejecta mass $M_{\rm ej}$ in $M_\odot$, ejecta velocity $\beta_{\rm ej}$ in natural units, and electron fraction Y_e, to explore the limits this combined dataset places on this parameter space.

We consider two fiducial KNe models, a "blue" KN and a "red" KN, following the prescription in (Kilpatrick et al. 2021) that maps κ onto Y_e using the work from Tanaka et al. (2020). The blue KN models have $Y_e = 0.45$ and approximate the blue component opacity derived from AT 2017gfo's light curve evolution (Drout et al. 2017; Kilpatrick et al. 2017). The red KN has a $Y_e = 0.10$, assuming that any ejecta released by GW190425's merger would have been exceptionally neutron-rich due to its probable direct collapse to a BH (Foley et al. 2020). We generated in-band light curves for these two families of KNe models with $M_{\rm ej} \in [0.001, 0.5]$ $M_\odot$ and $\beta_{\rm ej} \in [0.001, 0.5]$, and show our estimated detection probabilities in Figure 4.6. We detect a blue, AT 2017gfo-like KN at 24.6% (62.0%) and are insensitive to a red, AT 2017gfo-like KN at 0.4% (1.0%). From these constraints, an immediate conclusion is that to be sensitive to

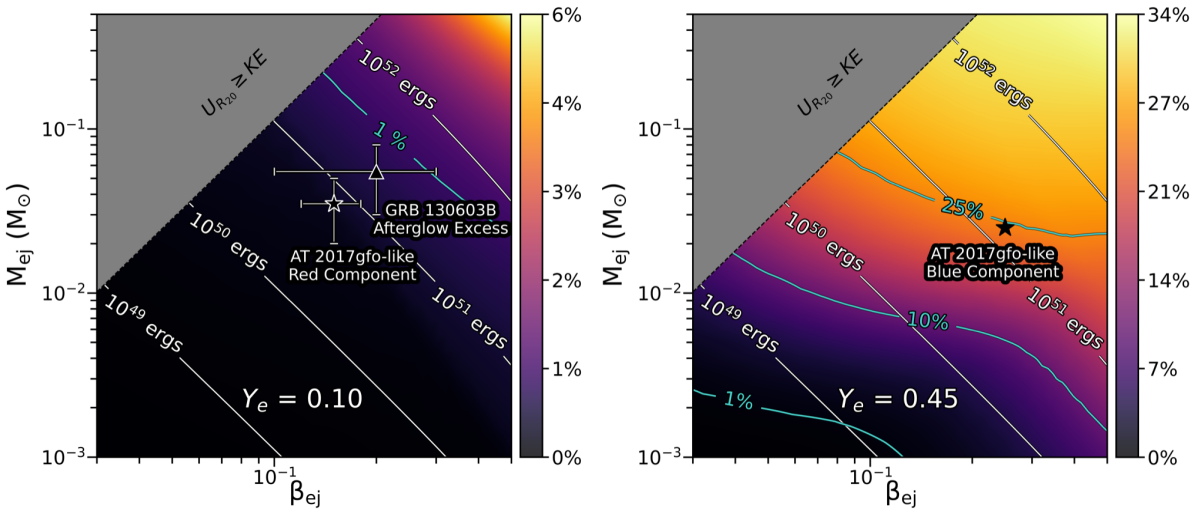

Figure 4.6 Detection probabilities for KNe models from Metzger (2017) as a function of ejecta mass ($M_{\rm ej}$ in $M_\odot$), ejecta velocity ($\beta_{\rm ej}$ in natural units), and electron fraction (Y_e). In the upper left corner of each plot, we have grayed out the region where the binding energy of the ejecta mass exceeds its kinetic energy assuming a stiff NS equation of state and an NS radius of 20 km. We show contours of equal probability in turquoise and contours of equal kinetic energy for the ejecta in white. Model values for AT 2017gfo-like components are taken from Kilpatrick et al. (2017). *Left* "Red" KNe models with $Y_e = 0.10$, overplotted with the putative KN counterpart to GRB130603B (Tanvir et al. 2013), and with AT 2017gfo's red component ($\beta_{\rm ej} = 0.15$, $M_{\rm ej} = 0.035\ M_\odot$) which we can not rule out at detection probability 0.4%. *Right* "Blue" KNe models with $Y_e = 0.45$, overplotted with AT 2017gfo's blue component ($\beta_{\rm ej} = 0.25$, $M_{\rm ej} = 0.025\ M_\odot$) which we rule out with 24.6% confidence.

more massive events (e.g., another GW190425-like or NSBH event), EM search teams should search in redder wavelengths with deeper limits. See Section 4.7 for a discussion on coordinating multi-band searches with `Teglon`.

4.6.2 sGRB

We adopt an sGRB afterglow model `JetFit` originally presented in Wu & MacFadyen (2018) and Wu & MacFadyen (2019) and used to model the afterglow light curve of GRB 170817A in the literature (e.g., Hajela et al. 2019, 2022; Kilpatrick et al. 2022a). For our fiducial model,

we adopt the general parameters from the best fit to the multi-wavelength GRB 170817A light curve in Hajela et al. (2022). These fixed parameters correspond to the electron energy fraction $\log \epsilon_e = -1$, the magnetic energy fraction $\log \epsilon_B = -5.17$, the spectral index of the electron distribution $p = 2.15$, the asymptotic Lorentz factor $\eta_0 = 8.02$, and the boost Lorentz factor $\gamma_B = 12$. We then vary the explosion energy E_0, the ambient density n, and the viewing angle $\theta_{\rm obs}$ to generate in-band light curves from our fiducial model. We consider a range of ambient densities in units of particles per cm^3, n $\in [10^{-6}, 10]$ cm^{-3}, and isotropic equivalent energy $E_{k,\rm iso} = 2E_0/(1 - \cos(\frac{1}{2\gamma_B})$ in units of 10^{51} ergs (FOE), $E_{k,\rm iso} \in [10^{-3}, 100]$ FOE, consistent with observed sGRB afterglows in Fong et al. (2015). Finally, we considered two viewing angles $\theta_{\rm obs} = 0$ and $\theta_{\rm obs} = 17°$ for an "on-axis" and "off-axis" model, but report only on our relatively insensitive on-axis limits because our off-axis models are substantially fainter. Our detection probability for a GRB 170918A-like model is 0.4×10^{-1}% (0.1%).

4.6.3 Generic Models

KNe and sGRB afterglows have extremely short rise times, and it is likely that ground-based discoveries catch only their decline (Arcavi et al. 2017a; Drout et al. 2017; Kilpatrick et al. 2017). Motivated by this, we include a generic class of empirical models parameterized by a peak absolute magnitude at the time of the merger, M_0, and a linear decline rate, ΔM, in units of mag day^{-1}, i.e.,

$$M(t) = M_0 - \Delta M(t - t_0). \tag{4.1}$$

where t is in days. We make these models agnostic in their emission mechanism and construct

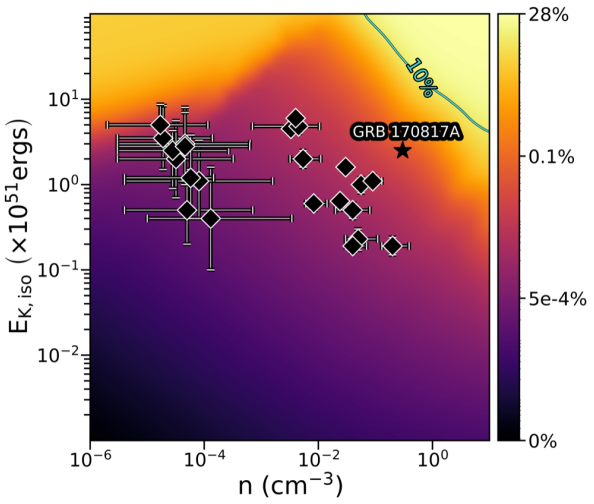

Figure 4.7 Limits on on-axis ($\theta_{\rm obs} = 0°$) sGRB models from Wu & MacFadyen (2018), as a function of isotropic kinetic energy ($E_{k,\rm iso}$ in FOE) and circumburst density (n in cm^{-3}). This dataset is relatively insensitive to these afterglow models, with a detection probability of a GRB 170817A-like model at 0.04% ($E_{k,\rm iso} = 2.5$ FOE, n= 0.3 cm^{-3} taken from Murguia-Berthier et al. (2017)).

their light curves with a flat spectral energy distribution (SED). We consider models that span a peak magnitude range $M_0 \in [-14, -20]$ mag and decline rates of $\Delta M \in [10^{-3}, 1.5]$ mag day^{-1} (in log space) to cover a parameter space that includes AT 2017gfo and several classes of well-known transients.

In Figure 4.8, we show our results, with parameters for AT 2017gfo representing an average of its decline across blue and red bands ($M \approx -16$ mag; $\Delta M \approx 0.7$ mag day^{-1}) and a collection of transient types overplotted in juxtaposition (referenced from Siebert et al. 2017). To the limits of this dataset's coverage, we confidently detect these well-known extragalactic transient types, reinforcing the results reported in Section 4.3. We rule out an AT 2017gfo-like model at 30.0% (75.9%) confidence.

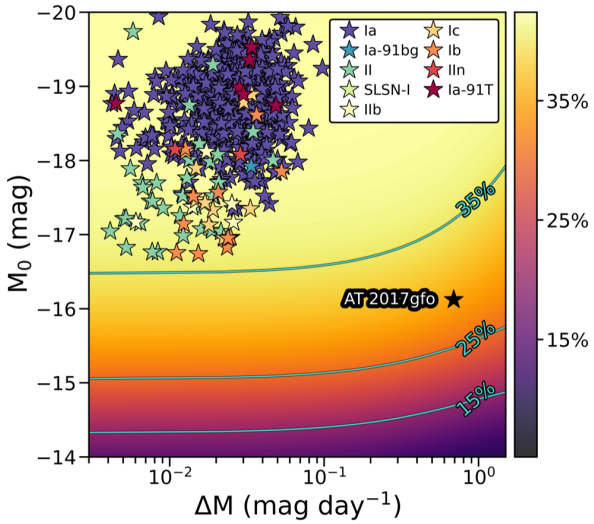

Figure 4.8 Limits on generic linear models parameterized by a peak absolute magnitude at the time of the merger (M_0 in mag), and a linear decline rate (ΔM in mag day^{-1}). Our models are agnostic in their emission mechanism and have a uniform SED. We overplot a range of well-known classes of transients taken from Siebert et al. (2017), as well as an average representation of AT 2017gfo ($M \approx -16$ mag, $\Delta M \approx 0.7$ mag day^{-1}; based on Siebert et al. 2017; Drout et al. 2017; Kilpatrick et al. 2017). We rule out an AT 2017gfo-like counterpart with 30.0% confidence.

4.7 Discussion & Conclusions

As the second BNS merger identified by the LVC, GW190425 had significantly different source properties from the first BNS event GW170817. In particular, the much larger total system mass of $3.4^{+0.3}_{-0.1}$ $M_\odot$ compared with $2.73^{+0.04}_{-0.01}$ $M_\odot$ (Abbott et al. 2017a) may lead to a significantly different EM counterpart (see Foley et al. 2020). Now that the LVK's O4 run is well underway, we are faced with a new paradigm for EM search: more distant events due to an increase in detector sensitivity, larger than expected localization areas due to Virgo's unexpected downtime, and an intrinsic diversity in BNS and NSBH systems leading to a range of EM counterparts. Therefore, it is likely that the search strategies that worked for GW170817 will have to be updated. To address these scenarios in O4 and beyond, we consider several

updates to `Teglon` which will enhance existing capabilities and add new ones. Here we explore our plan to optimize a network of telescopes engaged in a counterpart search, add new catalogs to `Teglon` to enable new types of counterpart searches, and consider combining different types of localization information and source properties from coincident sources such as FRBs, GRBs, and neutrino detections into `Teglon`.

4.7.1 EM Follow-up Network Coordination

If we sum the product of every pixel with the multiplicity of observations that cover it and divide that number by two — one epoch for a search image and one epoch for a template image — in principle, these observations could have uniquely covered $\sim 17,735$ deg^2, or roughly $1.8\times$ the final 90th percentile localization region. This fraction is even larger if we only consider the portions of the sky with no Sun constraint (i.e., the Eastern Spur of probability; see Figure 4.3). However, the EM community's follow-up strategy for GW sources is uncoordinated between observational teams, as evidenced by the search statistics shown in Table 4.1 — only $5,638$ deg^2 of localization area was uniquely searched. Furthermore, as seen in Figure 4.3, ZTF covered nearly the entire Eastern Spur of probability in $g + r$ over the course of the first 3 nights. Despite this, there were $\sim$ 900 other images taken of these same fields in the same filters within the same time period with 5 other instruments. In our analysis, these additional images offer little constraining power on the models that we consider. Despite the stroke of luck of GW170817 merging at a distance of 40 Mpc, and its counterpart AT 2017gfo discovered only $\sim$11 hours later, no KN was localized in O3 and the prospects for localizing one in O4 remain challenging. Increasing the coordination between follow-up facilities can drastically increase the

odds of rapidly and precisely localizing the next KN by leveraging `Teglon` to design strategies that can optimize our sensitivity to a range of counterpart models.

To address these challenges, in an upcoming enhancement `Teglon` will publish its redistributed localization map as a dynamic, real-time service that can be subscribed to by a network of telescopes. For a given GW event, each telescope within the network will be incorporated into a global queue that will query `Teglon` for the next best observation (i.e., the next highest probability observation). When an observation is scheduled, `Teglon` will decrement the probability in the pixels that are covered, and the following query for the next best observation will be dynamically updated. This coordination function will operate on a per-filter basis, allowing different passbands to be optimized independently. Finally, the pixel probability decrementation will be dynamic: `Teglon` will alter the probability proportional to a model-specific light curve as a function of filter. For instance, while KNe quickly decline in blue bands, they rise more slowly in red bands. For joint searches in blue and red filters, `Teglon` will restore probability to covered pixels at different rates to force successive observations back to regions of high 2D probability depending on what filter the search instrument is using. In this way, `Teglon` will optimize a network of search telescopes in both their spatial coverage and model sensitivity.

4.7.2 Specialized Catalog Additions - EM Counterparts to Binary Black Holes

The LVK is expected to detect 260^{+330}_{-150} binary black hole (BBH) mergers annually in O4[37], yet BBH mergers are by themselves not expected to directly produce luminous transients. However, the nuclei of galaxies are expected to host the densest populations of BH binaries,

[37] https://emfollow.docs.ligo.org/userguide/capabilities.html#summary-statistics

and for some of these binaries, they may be embedded in the disks of Active Galactic Nuclei (AGN). These environments can provide torques and tidal forces that can accelerate the pace of orbital decay (Bartos et al. 2017; Antoni et al. 2019; Gröbner et al. 2020) and lead to mergers in baryon-rich environments. For such systems, BBH mergers may trigger AGN flares; such a transient is proposed to explain the optical flare discovered 34 days after the GW detection of the BBH merger GW190521 (also known as S190521g; Graham et al. 2020; Abbott et al. 2020b, although see Ashton et al. (2020) for a rebuttal).

To facilitate the follow-up campaigns for BBHs, `Teglon` will be enhanced to include the AGN catalog from Secrest et al. (2015), which contains 1.4 million AGNs down to a faintness of $g = 26$ mag selected from the AllWISE catalog (Wright et al. 2010). This catalog is estimated to be complete for known AGNs to $\gtrsim 84\%$, and for all AGNs with $R < 19$ mag. Therefore, for AGNs with $z < 0.1$, the catalog is expected to be close to $> 90\%$ complete. This catalog will provide an alternative galaxy catalog weighting scheme to accentuate AGN hosts within the LVK volume.

4.7.3 FRB 190425A and Combining Coincident Sources within `Teglon`

While no optical counterparts were discovered in our follow-up or imaging from other efforts that appear consistent with a kilonova or GRB afterglow from GW190425 (Coughlin et al. 2019; Hosseinzadeh et al. 2019; Lundquist et al. 2019; Antier et al. 2020; Gompertz et al. 2020), Moroianu et al. (2023) reported the potential coincidence between FRB 190425A and GW190425 based on the former's detection inside the 90th percentile credible region of the latter and discovery of the FRB 2.5 hr after the GW190425 merger. Given their highly energetic

radio bursts, millisecond timescales, and the discovery of a FRB from the Galactic magnetar SGR J1935+2154 (CHIME/FRB Collaboration et al. 2020; Bochenek et al. 2020; Zhang 2022), FRBs are thought to arise from or in the immediate environments of magnetars (see, e.g., Margalit et al. 2019; Metzger et al. 2019; Lyutikov et al. 2020, for a discussion of various FRB emission models involving magnetars). Invoking the formation of a magnetar in the post-merger collapse of a BNS system (Zhang 2013; Most et al. 2018), FRBs may be credible radio counterparts to BNS mergers and combining observables from GW events and FRBs within `Teglon` can aid in rapid localization and identification of likely host galaxies (similar to the analysis in Panther et al. 2023).

While arcsecond-scale localization of FRBs is possible with interferometers such as ASKAP (Macquart et al. 2010), VLA (Law et al. 2018), and MeerKAT (Rajwade et al. 2022), the vast majority of FRBs are discovered with localizations of several deg^2 (including FRB 20190425A, e.g., by CHIME; CHIME/FRB Collaboration et al. 2021). At these angular scales, the `Teglon` algorithm is effective at selecting high-likelihood galaxies within the 2D localizations of both maps, for example by assuming that both the 2D localization provided by the LVK ($P_{\mathrm{2D,GW}}$) and the CHIME beam ($P_{\mathrm{2D,FRB}}$) represent independent estimates of the same source location and are combined into a single map ($P_{\mathrm{2D}_k} = P_{\mathrm{2D,GW}} \times P_{\mathrm{2D,FRB}}$, see Section 4.11.2). This assumption can be extended to any class of sources with localization on angular scales of degrees, indeed the LVK produces combined skymaps incorporating localization information from third parties such as GRBs and neutrino alerts[38].

`Teglon` can further benefit from FRB coincidences by incorporating distance con-

[38]See https://emfollow.docs.ligo.org/userguide/content.html.

straints based on the dispersion measure (DM) obtained directly from the FRB signal. This quantity correlates directly with the column of electrons along the line-of-sight to the FRB, which, combined with information on the density of electrons in the Milky Way, host galaxy environments, and the intergalactic medium, can constrain the distance to a FRB (Deng & Zhang 2014; Zhou et al. 2014; Macquart et al. 2020). In addition to multiple independent 2D localization constraints, the `Teglon` algorithm can accommodate multiple independent *volume* localizations by combining distance distributions within each map pixel, for example, replacing Equation 4.8 with a non-parametric distribution for each map pixel.

4.8 Software Utilized

`astropy` (Astropy Collaboration et al. 2013b), `DoPhot` (Schechter et al. 1993), `hotpants` (Becker 2015), `healpy` (Zonca et al. 2019b), `ligo.skymap` (Singer et al. 2016b,a), `PypeIt` (Prochaska et al. 2020b,a), `SExtractor` (Bertin & Arnouts 1996), `Treasure Map` (Wyatt et al. 2020), `Teglon` (Coulter 2021), `dustmaps` (Green 2018b).

4.9 Facilities Utilized

Keck:I (MOSFIRE), Nickel (Direct 2K), SMARTS 1.3m (ANDICAM), Swope (Direct 4K), Thacher (ACP).

4.10 Table of 1M2H Observations

Table 4.2. 1M2H UVOIR Imaging of the GW190425 Localization Region

Source[a]	α (J2000)	δ (J2000)	Exposure Time (s)	Date[b] (MJD)	Filter	Magnitude Limit[c] (3σ)
ANDICAM CCD	17:31:09.72	-08:27:14.40	900	58599.2453	I	21.60
ANDICAM CCD	16:52:07.06	-17:03:27.72	240	58599.2798	I	19.91
ANDICAM CCD	15:40:36.10	+28:30:30.60	240	58599.2895	I	20.24
ANDICAM CCD	15:41:53.64	+28:07:50.52	240	58599.2938	I	19.60
ANDICAM CCD	15:47:53.42	+25:43:31.80	240	58599.2984	I	21.06
ANDICAM CCD	15:56:03.36	+24:26:40.56	240	58599.3027	I	20.81
ANDICAM CCD	15:57:13.85	+25:48:54.36	240	58599.3074	I	20.87
ANDICAM CCD	16:02:59.59	+27:00:23.40	240	58599.3125	I	21.15
ANDICAM CCD	16:04:46.22	+24:16:31.08	240	58599.3175	I	20.92
ANDICAM CCD	16:09:05.81	+24:52:00.84	240	58599.3219	I	21.05
ANDICAM CCD	16:07:38.98	+22:20:19.32	240	58599.3263	I	21.03
ANDICAM CCD	15:59:51.17	+25:56:14.28	240	58599.3353	I	20.82
ANDICAM CCD	16:04:15.72	+24:48:32.76	240	58599.3396	I	20.93
ANDICAM CCD	16:14:57.24	+21:56:04.20	240	58599.3440	I	20.97
ANDICAM CCD	16:24:14.76	+20:10:47.64	240	58599.3486	I	20.97
ANDICAM CCD	16:04:56.28	+23:55:46.92	240	58599.3530	I	20.54
ANDICAM CCD	16:24:27.00	+19:28:41.88	240	58599.3575	I	20.92
ANDICAM CCD	16:19:29.18	+18:28:35.04	240	58599.3621	I	20.85
ANDICAM CCD	16:30:49.66	+16:14:47.40	240	58599.3666	I	20.93
ANDICAM CCD	16:23:10.90	+16:55:45.84	240	58599.3712	I	20.62
ANDICAM CCD	16:40:02.93	+15:52:47.64	240	58599.3757	I	20.76
ANDICAM CCD	17:13:21.60	-09:58:06.24	900	58599.3921	I	20.97
ANDICAM CCD	16:49:20.35	-17:38:53.16	240	58600.1619	I	21.34
ANDICAM CCD	16:53:04.61	-16:17:39.12	240	58600.1664	I	21.08
ANDICAM CCD	16:54:53.38	-16:57:16.20	240	58600.1710	I	21.04
ANDICAM CCD	16:50:52.92	-15:00:28.44	240	58600.1756	I	21.23
ANDICAM CCD	16:54:08.33	-07:38:20.04	240	58600.1803	I	21.37
ANDICAM IR	17:31:10.54	-08:26:56.04	30	58599.2012	K	14.28
ANDICAM IR	16:52:07.90	-17:03:09.36	30	58599.2797	H	14.27
ANDICAM IR	15:57:14.76	+25:49:12.36	30	58599.3073	H	14.37
ANDICAM IR	16:04:47.11	+24:16:48.72	30	58599.3174	H	14.00
ANDICAM IR	16:09:06.70	+24:52:18.84	30	58599.3218	H	14.81
ANDICAM IR	16:07:39.84	+22:20:37.32	30	58599.3262	H	14.58
ANDICAM IR	16:09:15.82	+25:42:51.84	30	58599.3307	H	15.03
ANDICAM IR	16:14:58.10	+21:56:21.84	30	58599.3439	H	14.78
ANDICAM IR	16:24:15.62	+20:11:05.64	30	58599.3486	H	15.25
ANDICAM IR	16:24:27.84	+19:28:59.88	30	58599.3575	H	14.54
ANDICAM IR	16:19:30.05	+18:28:52.68	30	58599.3620	H	15.17
ANDICAM IR	16:30:50.52	+16:15:05.40	30	58599.3666	H	14.45
ANDICAM IR	16:23:11.76	+16:56:03.84	30	58599.3711	H	14.53
ANDICAM IR	16:40:03.77	+15:53:05.64	30	58599.3756	H	13.67
ANDICAM IR	17:13:22.42	-09:57:48.24	30	58599.4030	H	14.62
ANDICAM IR	17:13:22.44	-09:57:48.24	30	58599.4140	J	14.65
ANDICAM IR	16:49:21.22	-17:38:34.80	30	58600.1619	H	15.05
ANDICAM IR	16:53:05.42	-16:17:21.12	30	58600.1664	H	15.25
ANDICAM IR	16:54:54.22	-16:56:58.20	30	58600.1709	H	14.98
ANDICAM IR	16:50:53.74	-15:00:10.08	30	58600.1756	H	14.58
ANDICAM IR	16:54:09.12	-07:38:02.04	30	58600.1803	H	15.09
Nickel	13:54:45.17	+44:46:44.76	600	58599.1986	r	21.09
Nickel	13:54:45.22	+44:46:44.40	600	58599.2059	i	20.44
Nickel	14:32:30.31	+55:45:11.52	600	58599.2297	r	21.28
Nickel	14:32:30.36	+55:45:11.16	600	58599.2371	i	20.33

Table 4.2 (cont'd)

Source[a]	α (J2000)	δ (J2000)	Exposure Time (s)	Date[b] (MJD)	Filter	Magnitude Limit[c] (3σ)
Nickel	14:36:47.74	+34:17:57.48	180	58599.2458	r	20.61
Nickel	13:20:49.78	+43:58:05.16	180	58599.2498	r	20.72
Nickel	15:31:39.43	+40:52:21.36	180	58599.2538	r	20.01
Nickel	15:13:21.19	+30:57:59.40	180	58599.2575	r	20.50
Nickel	15:29:23.45	+28:19:00.84	180	58599.2615	r	20.32
Nickel	15:32:42.10	+28:22:30.72	180	58599.2656	r	20.37
Nickel	16:02:36.14	+37:21:59.40	180	58599.2695	r	20.63
Nickel	15:40:43.94	+28:18:02.16	180	58599.2731	r	20.44
Nickel	15:40:32.18	+28:31:15.96	180	58599.2764	r	18.89
Nickel	15:41:49.63	+28:08:30.48	180	58599.2802	r	20.31
Nickel	15:43:52.90	+28:31:59.16	180	58599.2847	r	20.49
Nickel	15:47:31.75	+26:04:25.32	180	58599.2928	r	20.48
Nickel	15:47:49.20	+25:44:19.32	180	58599.2968	r	20.40
Nickel	15:50:17.64	+26:26:21.84	180	58599.3015	r	20.06
Nickel	15:51:54.96	+24:21:03.96	180	58599.3058	r	20.13
Nickel	15:57:09.43	+25:49:45.12	180	58599.3096	r	19.23
Nickel	15:58:46.87	+26:08:47.04	180	58599.3141	r	20.21
Nickel	15:55:58.66	+24:27:32.40	180	58599.3179	r	19.97
Nickel	15:59:46.10	+25:57:05.04	180	58599.3218	r	22.71
Nickel	16:02:54.67	+27:01:13.80	180	58599.3254	r	19.77
Nickel	16:04:30.02	+25:12:05.76	180	58599.3297	r	20.10
Nickel	16:03:48.48	+25:01:21.00	180	58599.3343	r	20.07
Nickel	16:03:08.54	+24:23:10.32	180	58599.3382	r	20.79
Nickel	12:24:55.92	+28:34:15.96	180	58599.3422	r	19.91
Nickel	16:04:10.10	+24:49:27.48	180	58599.3464	r	20.77
Nickel	16:04:40.58	+24:17:26.52	180	58599.3501	r	19.81
Nickel	16:04:54.14	+23:40:17.04	180	58599.3580	r	20.71
Nickel	16:09:11.95	+24:52:57.36	180	58599.3659	r	18.51
Nickel	16:05:17.54	+22:31:18.48	180	58599.3696	r	20.78
Nickel	16:05:30.84	+22:12:00.72	180	58599.3731	r	19.88
Nickel	16:11:16.49	+23:58:45.48	180	58599.3768	r	20.57
Nickel	16:07:33.34	+22:21:26.64	180	58599.3809	r	18.90
Nickel	16:08:43.85	+22:03:24.84	180	58599.3854	r	19.82
Nickel	16:12:13.63	+23:00:59.04	180	58599.3896	r	19.63
Nickel	16:13:39.10	+22:56:00.24	180	58599.3938	r	20.38
Nickel	16:11:50.88	+20:56:20.04	180	58599.3982	r	20.00
Nickel	16:14:50.57	+21:57:14.40	180	58599.4020	r	20.19
Nickel	16:17:57.84	+21:34:09.84	180	58599.4060	r	20.14
Nickel	16:16:04.18	+20:37:46.56	180	58599.4105	r	19.85
Nickel	16:17:59.64	+21:05:00.24	180	58599.4149	r	20.31
Nickel	16:15:34.70	+19:39:15.48	180	58599.4189	r	20.29
Nickel	16:21:01.97	+21:05:29.76	180	58599.4226	r	20.30
Nickel	16:19:21.82	+18:29:51.72	180	58599.4270	r	20.51
Nickel	13:15:16.46	+37:37:39.36	600	58601.4778	i	20.18
Nickel	14:36:48.55	+34:17:42.36	180	58603.3436	r	20.51
Nickel	13:20:49.78	+43:58:05.52	180	58603.3479	r	20.31
Nickel	15:31:40.85	+40:52:05.16	180	58603.3512	r	19.35
Nickel	15:13:22.68	+30:57:46.80	180	58603.3548	r	20.06
Nickel	15:29:25.13	+28:18:47.88	180	58603.3577	r	19.95
Nickel	15:32:43.90	+28:22:18.84	180	58603.3605	r	20.08
Nickel	16:02:38.06	+37:21:49.68	180	58603.3634	r	20.05
Nickel	15:40:45.70	+28:17:52.08	180	58603.3662	r	20.18

Table 4.2 (cont'd)

Source[a]	α (J2000)	δ (J2000)	Exposure Time (s)	Date[b] (MJD)	Filter	Magnitude Limit[c] (3σ)
Nickel	15:40:33.96	+28:31:05.16	180	58603.3689	r	18.81
Nickel	15:41:51.36	+28:08:21.12	180	58603.3717	r	20.07
Nickel	15:43:54.43	+28:31:47.64	180	58603.3750	r	19.57
Nickel	15:47:33.36	+26:04:12.72	180	58603.3820	r	19.81
Nickel	15:47:51.10	+25:44:06.36	180	58603.3855	r	20.28
Nickel	15:50:19.51	+26:26:09.24	180	58603.3885	r	19.70
Nickel	15:51:56.76	+24:20:46.68	180	58603.3918	r	19.85
Nickel	15:57:11.38	+25:49:29.64	180	58603.3950	r	19.68
Nickel	15:58:48.86	+26:08:30.84	180	58603.3981	r	19.44
Nickel	15:56:00.67	+24:27:15.48	180	58603.4012	r	20.09
Nickel	15:59:48.62	+25:56:47.40	180	58603.4041	r	19.39
Nickel	16:02:57.19	+27:00:56.88	180	58603.4072	r	19.79
Nickel	16:04:32.52	+25:11:48.48	180	58603.4104	r	20.02
Nickel	16:03:51.07	+25:01:02.28	180	58603.4136	r	19.56
Nickel	16:03:11.02	+24:22:50.16	180	58603.4165	r	19.78
Nickel	12:24:57.79	+28:34:09.84	180	58603.4197	r	19.34
Nickel	16:04:12.24	+24:49:00.48	180	58603.4231	r	20.50
Nickel	16:04:42.55	+24:16:58.80	180	58603.4258	r	20.02
Nickel	16:04:55.80	+23:39:47.52	180	58603.4314	r	20.46
Nickel	16:09:02.26	+24:52:32.52	180	58603.4369	r	17.77
Nickel	16:05:19.08	+22:30:50.04	180	58603.4396	r	20.07
Nickel	16:05:32.45	+22:11:31.92	180	58603.4434	r	18.10
Nickel	16:11:18.34	+23:58:14.88	180	58603.4462	r	19.98
Nickel	16:07:35.30	+22:20:57.12	180	58603.4489	r	18.82
Nickel	16:08:45.84	+22:02:56.76	180	58603.4520	r	19.20
Nickel	16:12:15.82	+23:00:30.24	180	58603.4546	r	19.03
Nickel	16:13:41.57	+22:55:31.44	180	58603.4573	r	20.02
Nickel	16:11:53.33	+20:55:53.40	180	58603.4606	r	19.52
Nickel	16:14:53.14	+21:56:44.16	180	58603.4636	r	19.36
Nickel	16:18:00.65	+21:33:41.04	180	58603.4665	r	19.35
Nickel	16:16:07.13	+20:37:16.32	180	58603.4699	r	19.48
Nickel	16:18:02.47	+21:04:29.64	180	58603.4730	r	19.95
Nickel	16:15:37.46	+19:38:44.16	180	58603.4766	r	19.81
Nickel	16:21:05.11	+21:05:00.96	180	58603.4795	r	19.73
Nickel	16:19:25.01	+18:29:17.52	180	58603.4829	r	20.00
Nickel	16:24:10.34	+20:11:32.28	180	58603.4860	r	19.58
Nickel	17:31:04.44	-08:26:16.80	600	58603.4979	r	19.00
Nickel	13:53:34.30	+40:16:23.88	330	58606.2303	B	19.68
Nickel	13:53:34.39	+40:16:26.40	240	58606.2345	V	19.60
Nickel	13:53:34.44	+40:16:29.28	270	58606.2377	r	19.59
Nickel	13:53:34.54	+40:16:30.72	300	58606.2412	i	19.60
Nickel	12:11:57.48	+24:08:15.00	60	58606.2743	B	19.90
Nickel	12:11:57.48	+24:08:16.08	60	58606.2765	r	20.20
Nickel	12:11:57.46	+24:08:16.44	60	58606.2776	i	20.05
Nickel	12:11:57.46	+24:08:16.44	60	58606.2776	i	20.08
Nickel	12:35:58.18	+27:56:03.12	600	58606.2887	r	19.87
Nickel	12:35:58.20	+27:56:03.12	600	58606.2960	i	19.79
Nickel	12:03:17.42	+44:31:58.44	600	58606.3238	r	20.49
Nickel	12:03:17.40	+44:31:58.44	600	58606.3311	i	19.97
Nickel	13:53:35.66	+40:16:33.24	330	58606.3414	B	20.94
Nickel	13:53:35.64	+40:16:33.60	240	58606.3456	V	20.63
Nickel	13:53:35.66	+40:16:33.60	270	58606.3488	r	20.91

Table 4.2 (cont'd)

Source[a]	α (J2000)	δ (J2000)	Exposure Time (s)	Date[b] (MJD)	Filter	Magnitude Limit[c] (3σ)
Nickel	13:53:35.62	+40:16:34.68	300	58606.3523	i	20.20
Nickel	13:05:48.05	+37:37:39.36	600	58606.4186	V	19.96
Nickel	13:05:48.07	+37:37:39.72	600	58606.4260	r	19.24
Nickel	13:05:48.07	+37:37:39.72	600	58606.4333	i	18.99
Nickel	16:24:30.77	+19:29:07.08	180	58606.4523	r	18.23
Nickel	16:23:14.71	+16:56:09.60	180	58606.4558	r	17.88
Nickel	16:25:41.30	+16:27:28.80	180	58606.4593	r	18.30
Nickel	16:27:22.82	+16:00:01.44	180	58606.4625	r	18.18
Nickel	16:28:55.37	+15:25:30.00	180	58606.4657	r	17.39
Nickel	16:30:52.68	+16:15:19.80	180	58606.4716	r	17.76
Nickel	16:29:38.62	+15:39:50.40	180	58606.4749	r	18.41
Nickel	16:30:04.97	+15:43:06.60	180	58606.4782	r	18.79
Nickel	16:31:37.97	+13:51:57.24	180	58606.4824	r	19.22
Nickel	16:37:09.86	+14:11:49.56	180	58606.4860	r	19.35
Nickel	16:40:42.74	+14:21:24.84	180	58606.4897	r	19.31
Nickel	16:37:37.54	+11:44:18.60	180	58606.4932	r	18.93
Nickel	16:39:28.87	+11:12:57.60	180	58606.4968	r	19.03
Nickel	16:43:08.59	+08:31:03.72	180	58606.5005	r	18.56
Nickel	16:46:24.86	+09:02:34.80	180	58606.5053	r	18.21
Nickel	16:49:36.70	+09:47:18.24	180	58606.5089	r	17.90
Nickel	12:11:51.29	+24:08:05.28	60	58612.2555	r	18.12
Nickel	12:11:51.29	+24:08:05.28	60	58612.2566	i	18.77
Nickel	12:03:10.99	+44:31:41.88	600	58612.3013	r	19.78
Nickel	12:03:10.99	+44:31:41.52	600	58612.3086	i	18.52
Nickel	16:31:32.21	+30:08:41.64	45	58612.3273	V	17.96
Nickel	16:31:32.23	+30:08:41.64	45	58612.3292	i	17.92
Nickel	16:32:19.03	+19:50:03.48	420	58612.4514	r	19.79
Nickel	16:32:19.03	+19:50:03.48	480	58612.4566	i	18.47
Nickel	17:30:24.29	-13:45:39.96	600	58612.4993	r	18.40
Nickel	17:30:24.26	-13:45:39.96	600	58612.5066	i	15.96
Swope	05:48:48.14	-25:21:50.04	180	58598.9937	i	21.01
Swope	16:48:15.84	-17:25:10.56	180	58599.1293	i	20.84
Swope	16:52:15.50	-16:55:18.48	180	58599.1326	i	20.76
Swope	16:52:07.51	-16:25:29.28	180	58599.1364	i	20.81
Swope	16:54:19.06	-16:52:38.28	180	58599.1402	i	20.91
Swope	16:51:47.52	-14:56:01.68	180	58599.1444	i	20.87
Swope	16:55:01.87	-09:57:58.68	180	58599.1478	i	20.99
Swope	17:01:30.14	-12:27:01.08	180	58599.1511	i	20.80
Swope	16:54:41.69	-07:28:57.36	180	58599.1549	i	20.65
Swope	16:56:39.65	-06:59:02.04	180	58599.1579	i	20.94
Swope	16:56:36.22	-06:29:16.44	180	58599.1613	i	20.70
Swope	16:58:31.01	-05:29:36.96	180	58599.1648	i	20.78
Swope	16:54:23.78	-03:30:23.40	180	58599.1688	i	20.61
Swope	16:56:21.77	-02:00:58.32	180	58599.1720	i	20.73
Swope	16:56:19.51	-01:31:10.20	180	58599.1754	i	20.95
Swope	17:04:24.62	-04:30:05.40	180	58599.1788	i	20.67
Swope	17:13:39.50	-09:51:43.92	300	58599.1827	r	21.47
Swope	17:13:39.50	-09:51:44.64	300	58599.1867	i	21.16
Swope	17:13:39.53	-09:51:43.92	300	58599.1908	g	21.68
Swope	17:31:27.60	-08:20:46.68	600	58599.1982	r	21.78
Swope	17:31:27.62	-08:20:47.40	600	58599.2061	i	21.45
Swope	17:31:27.62	-08:20:46.68	600	58599.2136	g	22.12

Table 4.2 (cont'd)

Source[a]	α (J2000)	δ (J2000)	Exposure Time (s)	Date[b] (MJD)	Filter	Magnitude Limit[c] (3σ)
Swope	16:04:33.07	+23:49:04.80	180	58599.2223	i	20.96
Swope	16:58:21.41	-02:00:43.20	180	58599.2258	i	21.27
Swope	16:52:24.98	+02:27:39.96	180	58599.2295	i	21.17
Swope	16:50:30.86	+04:26:55.32	180	58599.2326	i	21.14
Swope	16:04:43.13	+17:51:32.40	180	58599.2367	i	21.19
Swope	16:17:17.52	+19:21:08.64	180	58599.2402	i	21.11
Swope	16:15:10.08	+19:21:02.88	180	58599.2437	i	21.00
Swope	16:06:46.54	+19:50:55.32	180	58599.2469	i	20.98
Swope	16:15:19.03	+21:50:09.60	180	58599.2506	i	21.03
Swope	16:06:45.43	+22:19:55.20	180	58599.2538	i	20.98
Swope	16:02:26.26	+23:19:39.72	180	58599.2570	i	20.90
Swope	16:02:24.12	+24:19:08.40	180	58599.2602	i	21.09
Swope	15:55:52.44	+24:19:06.60	180	58599.2633	i	21.14
Swope	16:51:52.82	-14:55:45.84	180	58599.2672	i	21.35
Swope	15:46:56.30	+25:48:27.00	180	58599.2712	i	21.23
Swope	15:35:30.67	+27:17:55.32	180	58599.2745	i	21.11
Swope	15:42:06.12	+27:47:40.20	180	58599.2777	i	20.97
Swope	15:28:27.72	+28:17:34.80	180	58599.2820	i	21.08
Swope	15:32:58.22	+28:17:29.04	180	58599.2852	i	21.04
Swope	15:41:58.13	+28:17:28.68	180	58599.2881	i	21.06
Swope	15:46:01.42	+30:17:00.96	180	58599.2926	i	20.93
Swope	15:39:41.66	+28:17:26.16	180	58599.2961	i	21.12
Swope	15:48:41.38	+29:18:08.28	600	58599.3002	r	21.89
Swope	16:35:51.96	+22:27:47.88	600	58599.3119	r	22.12
Swope	16:55:16.87	+04:58:04.80	600	58599.3217	r	22.29
Swope	17:01:40.34	-06:53:32.64	600	58599.3429	r	22.00
Swope	17:10:21.26	+07:42:18.36	600	58599.3524	r	22.16
Swope	17:11:59.23	+09:54:34.56	600	58599.3627	r	22.20
Swope	16:25:41.09	+19:20:58.92	180	58599.3720	r	21.41
Swope	16:19:18.41	+18:20:56.40	180	58599.3758	r	21.44
Swope	16:23:22.03	+16:51:48.24	180	58599.3794	r	21.47
Swope	16:25:24.12	+16:22:05.16	180	58599.3828	r	21.44
Swope	16:29:28.56	+15:52:15.24	180	58599.3861	r	21.38
Swope	16:29:24.50	+15:22:18.84	180	58599.3891	r	21.52
Swope	17:20:08.66	-01:00:54.72	180	58599.3927	r	21.62
Swope	16:50:50.76	+07:55:32.52	180	58599.3965	r	21.46
Swope	16:46:55.97	+08:55:05.88	180	58599.3995	r	21.24
Swope	16:48:43.37	+06:25:56.28	180	58599.4034	r	21.50
Swope	16:44:47.59	+07:25:46.92	180	58599.4083	i	20.60
Swope	17:01:39.50	-06:53:53.16	600	58599.4128	i	21.84
Swope	17:01:38.38	-06:54:24.84	802	58599.4260	r	21.44
Swope	13:09:27.50	+28:22:41.88	450	58600.1866	B	21.83
Swope	13:09:27.50	+28:22:41.16	150	58600.1941	V	21.14
Swope	13:09:27.41	+28:22:41.52	150	58600.1982	g	21.84
Swope	13:09:27.46	+28:22:40.08	150	58600.2005	i	20.91
Swope	13:09:27.41	+28:22:40.80	150	58600.2028	r	21.31
Swope	17:05:34.56	+08:04:54.84	360	58600.2797	r	22.08
Swope	17:05:34.61	+08:04:54.12	360	58600.2844	i	21.64
Swope	17:05:34.58	+08:04:54.84	360	58600.2891	g	21.95
Swope	17:05:34.56	+08:04:55.56	600	58600.2939	u	21.49
Swope	17:05:34.37	+08:04:53.40	360	58600.3037	V	22.01
Swope	17:05:34.34	+08:04:54.12	570	58600.3090	B	22.37

Table 4.2 (cont'd)

Source[a]	α (J2000)	δ (J2000)	Exposure Time (s)	Date[b] (MJD)	Filter	Magnitude Limit[c] (3σ)
Swope	16:16:28.56	+22:21:58.32	1200	58601.3103	r	22.50
Swope	05:48:48.65	-25:21:59.40	180	58601.9885	i	20.74
Swope	12:12:20.28	+24:14:27.60	45	58602.1652	r	21.09
Swope	12:12:20.26	+24:14:25.80	45	58602.1662	i	20.46
Swope	12:12:20.18	+24:14:27.60	45	58602.1672	g	21.64
Swope	12:12:20.11	+24:14:29.04	300	58602.1682	u	21.25
Swope	12:12:20.14	+24:14:24.36	45	58602.1726	V	21.13
Swope	12:12:20.16	+24:14:25.80	120	58602.1737	B	21.99
Swope	15:48:44.62	+29:18:35.64	600	58602.2468	r	22.54
Swope	16:35:55.87	+22:28:16.68	600	58602.2563	r	22.59
Swope	16:55:19.58	+04:58:21.72	600	58602.2665	r	22.11
Swope	17:01:43.18	-06:53:18.96	600	58602.2860	r	20.91
Swope	17:10:23.95	+07:42:32.40	600	58602.3042	r	21.44
Swope	17:12:02.26	+09:54:52.56	600	58602.3150	r	21.84
Swope	17:13:47.50	-09:50:56.76	300	58602.3248	r	21.67
Swope	17:13:47.52	-09:50:57.12	300	58602.3288	i	20.95
Swope	17:13:47.50	-09:50:56.76	300	58602.3327	g	22.21
Swope	17:31:34.39	-08:20:18.60	600	58602.3392	r	22.23
Swope	17:31:34.42	-08:20:18.96	600	58602.3467	i	21.48
Swope	17:31:34.34	-08:20:18.24	600	58602.3541	g	22.67
Swope	16:25:41.38	+19:20:14.64	180	58602.3870	r	21.72
Swope	16:19:19.10	+18:20:38.76	180	58602.3907	r	21.64
Swope	16:23:23.35	+16:51:09.72	180	58602.3940	r	21.62
Swope	16:25:25.70	+16:21:21.60	180	58602.3973	r	21.51
Swope	16:29:29.38	+15:51:33.84	180	58602.4004	r	21.63
Swope	16:29:25.66	+15:21:34.92	180	58602.4037	r	21.47
Swope	17:20:09.79	-01:01:39.00	180	58602.4074	r	21.08
Swope	16:50:51.94	+07:54:58.68	180	58602.4111	r	21.74
Swope	16:46:57.19	+08:54:40.32	180	58602.4148	r	21.59
Swope	16:48:44.71	+06:25:23.88	180	58602.4184	r	21.72
Swope	16:44:48.84	+07:25:10.20	180	58602.4216	i	20.56
Swope	05:22:58.08	-11:23:30.12	600	58602.9589	r	21.39
Swope	05:22:58.15	-11:23:30.12	600	58602.9667	i	21.11
Swope	05:22:58.06	-11:23:29.04	600	58602.9742	g	22.72
Swope	12:12:25.44	+24:14:24.72	90	58603.0706	B	21.66
Swope	12:12:25.44	+24:14:23.28	45	58603.0721	V	21.08
Swope	12:12:25.42	+24:14:27.60	240	58603.0733	u	20.98
Swope	12:12:25.42	+24:14:25.80	45	58603.0767	g	21.63
Swope	12:12:25.44	+24:14:24.72	45	58603.0777	i	20.25
Swope	12:12:25.42	+24:14:25.44	45	58603.0787	r	20.79
Swope	13:09:32.93	+28:22:49.80	150	58603.1127	g	22.03
Swope	13:09:32.90	+28:22:49.44	150	58603.1172	r	21.31
Swope	16:48:25.25	-17:25:10.56	180	58603.1540	i	21.36
Swope	16:52:28.66	-16:55:21.00	180	58603.1576	i	20.87
Swope	16:56:32.86	-01:31:23.16	180	58603.1623	i	21.44
Swope	17:04:38.23	-04:30:09.36	180	58603.1675	i	21.44
Swope	16:58:32.11	-02:01:00.12	180	58603.1857	i	21.40
Swope	16:56:32.30	-02:00:54.36	180	58603.1888	i	21.44
Swope	16:54:36.96	-03:30:26.28	180	58603.1921	i	21.40
Swope	16:58:44.81	-05:29:35.16	180	58603.1955	i	21.44
Swope	16:56:48.94	-06:29:14.28	180	58603.1987	i	21.29
Swope	16:56:52.61	-06:59:01.68	180	58603.2019	i	21.31

Table 4.2 (cont'd)

Source[a]	α (J2000)	δ (J2000)	Exposure Time (s)	Date[b] (MJD)	Filter	Magnitude Limit[c] (3σ)
Swope	17:01:43.92	-12:26:56.76	180	58603.2057	i	21.19
Swope	16:54:56.40	-07:28:42.60	180	58603.2091	i	21.38
Swope	16:55:14.81	-09:57:52.92	180	58603.2126	i	21.45
Swope	16:52:01.56	-14:55:51.96	180	58603.2317	i	21.39
Swope	16:54:32.14	-16:55:17.40	180	58603.2349	i	21.23
Swope	16:52:19.70	-16:25:25.68	180	58603.2627	i	21.55
Swope	15:35:39.22	+27:17:56.76	180	58603.2673	i	21.35
Swope	15:28:36.22	+28:17:23.28	180	58603.2707	i	21.37
Swope	15:33:06.96	+28:17:26.52	180	58603.2739	i	21.37
Swope	15:39:51.67	+28:17:28.68	180	58603.2769	i	21.39
Swope	15:46:09.84	+30:16:49.80	180	58603.2802	i	21.33
Swope	15:42:05.02	+28:17:24.00	180	58603.2834	i	21.30
Swope	15:42:13.37	+27:47:34.44	180	58603.2867	i	21.32
Swope	15:47:05.74	+25:48:18.72	180	58603.2902	i	21.18
Swope	15:56:01.15	+24:19:01.20	180	58603.2936	i	21.09
Swope	16:02:33.74	+24:19:05.16	180	58603.2968	i	20.83
Swope	16:02:34.85	+23:19:22.80	180	58603.3035	i	20.43
Swope	16:06:56.62	+22:19:56.28	180	58603.3067	i	21.01
Swope	16:15:27.05	+21:49:48.72	180	58603.3100	i	21.15
Swope	16:06:57.34	+19:50:28.32	180	58603.3130	i	21.17
Swope	16:15:21.43	+19:20:57.48	180	58603.3162	i	21.09
Swope	16:17:28.32	+19:21:05.04	180	58603.3195	i	21.33
Swope	16:04:54.79	+17:51:38.52	180	58603.3227	i	21.27
Swope	16:50:43.61	+04:26:56.04	180	58603.3267	i	21.35
Swope	16:52:37.82	+02:27:38.52	180	58603.3298	i	21.29
Swope	12:12:22.56	+24:13:55.92	120	58608.1166	B	22.04
Swope	12:12:22.54	+24:13:56.28	45	58608.1186	V	21.19
Swope	12:12:22.56	+24:13:57.72	330	58608.1199	u	21.46
Swope	12:12:22.61	+24:13:56.28	45	58608.1242	g	21.73
Swope	12:12:22.66	+24:13:55.20	45	58608.1252	i	20.05
Swope	12:12:22.63	+24:13:55.92	45	58608.1261	r	20.92
Swope	17:05:37.73	+08:05:45.60	390	58608.2559	r	22.25
Swope	17:05:37.75	+08:05:45.24	390	58608.2609	i	21.56
Swope	17:05:37.75	+08:05:45.96	390	58608.2659	g	22.09
Swope	17:05:37.73	+08:05:46.68	600	58608.2710	u	22.07
Swope	17:05:37.70	+08:05:45.60	390	58608.2789	V	22.34
Swope	17:05:37.73	+08:05:45.24	480	58608.2840	B	22.89
Swope	23:50:58.32	-69:36:20.16	210	58608.4003	B	21.79
Swope	23:50:58.20	-69:36:19.08	60	58608.4032	V	20.91
Swope	23:50:58.54	-69:36:19.44	540	58608.4045	u	21.42
Swope	23:50:58.42	-69:36:19.44	60	58608.4113	g	21.51
Swope	23:50:58.32	-69:36:19.44	60	58608.4125	i	20.58
Swope	23:50:58.30	-69:36:19.44	60	58608.4137	r	21.18
Swope	12:12:22.51	+24:14:08.88	45	58609.1364	r	21.18
Swope	12:12:22.73	+24:14:08.88	45	58609.1373	i	20.58
Swope	12:12:22.68	+24:14:09.96	45	58609.1383	g	21.64
Swope	12:12:22.61	+24:14:11.76	240	58609.1394	u	20.81
Swope	12:12:22.63	+24:14:09.24	45	58609.1432	V	21.09
Swope	12:12:22.63	+24:14:09.60	45	58609.1442	B	21.00
Swope	13:09:26.06	+28:23:19.68	120	58609.1485	r	21.28
Swope	13:09:26.11	+28:23:18.96	120	58609.1504	i	20.92
Swope	13:09:26.06	+28:23:20.40	120	58609.1523	g	21.97

Table 4.2 (cont'd)

Source[a]	α (J2000)	δ (J2000)	Exposure Time (s)	Date[b] (MJD)	Filter	Magnitude Limit[c] (3σ)
Swope	13:09:26.02	+28:23:21.84	600	58609.1542	u	21.16
Swope	13:09:26.04	+28:23:20.04	120	58609.1618	V	21.07
Swope	13:09:26.04	+28:23:19.68	390	58609.1637	B	21.81
Swope	17:05:35.26	+08:05:27.60	390	58609.3391	r	20.04
Swope	17:05:35.28	+08:05:26.88	390	58609.3441	i	19.76
Swope	17:05:35.26	+08:05:27.96	390	58609.3491	g	21.03
Swope	17:05:35.21	+08:05:28.68	600	58609.3542	u	19.56
Swope	17:05:35.28	+08:05:27.60	390	58609.3621	V	19.82
Swope	17:05:35.23	+08:05:27.24	480	58609.3671	B	20.13
Swope	23:50:53.86	-69:34:40.80	90	58611.4195	r	18.51
Swope	23:50:53.88	-69:34:40.80	90	58611.4215	i	16.65
Swope	23:50:53.98	-69:34:40.80	90	58611.4233	g	19.64
Swope	23:50:53.76	-69:34:41.16	90	58611.4292	V	17.17
Swope	23:50:53.78	-69:34:41.52	240	58611.4310	B	17.34
Swope	17:05:36.50	+08:06:34.92	300	58612.3206	r	22.03
Swope	17:05:36.53	+08:06:34.20	300	58612.3250	i	21.52
Swope	17:05:36.48	+08:06:34.92	300	58612.3294	g	22.01
Swope	17:05:36.43	+08:06:36.00	600	58612.3337	u	21.72
Swope	17:05:36.38	+08:06:34.92	300	58612.3424	V	21.89
Swope	17:05:36.36	+08:06:35.28	600	58612.3467	B	22.63
Swope	23:50:48.05	-69:34:45.12	180	58612.4136	B	21.93
Swope	23:50:47.93	-69:34:44.76	60	58612.4166	V	21.21
Swope	23:50:48.41	-69:34:43.32	60	58612.4184	g	21.53
Swope	23:50:48.38	-69:34:42.96	60	58612.4199	i	20.40
Swope	23:50:48.36	-69:34:42.96	60	58612.4212	r	21.14
Swope	23:50:48.55	-69:34:43.68	510	58612.4227	u	21.16
Thacher	11:59:16.61	+21:05:57.48	180	58599.2363	r	18.50
Thacher	12:08:15.62	+25:15:54.72	180	58599.2414	r	17.93
Thacher	12:15:27.96	+23:52:45.84	180	58599.2488	r	18.68
Thacher	12:24:23.50	+28:43:48.36	180	58599.2539	r	18.77
Thacher	12:27:58.22	+26:59:51.72	180	58599.2565	r	18.16
Thacher	12:33:15.72	+29:46:09.12	180	58599.2592	r	18.90
Thacher	12:35:44.90	+26:59:51.00	180	58599.2618	r	18.67
Thacher	12:39:05.88	+27:41:25.44	180	58599.2644	r	17.96
Thacher	12:40:21.79	+29:25:22.80	180	58599.2669	r	18.31
Thacher	12:39:28.90	+29:04:36.84	180	58599.2695	r	18.53
Thacher	13:29:47.83	+47:11:25.80	300	58599.2754	g	19.63
Thacher	13:29:40.58	+47:11:23.64	300	58599.3087	z	18.59
Thacher	13:46:10.42	+56:47:25.80	180	58599.3201	r	18.63
Thacher	13:45:06.31	+55:45:05.04	180	58599.3227	r	18.18
Thacher	14:10:48.72	+55:24:12.96	180	58599.3280	r	19.22
Thacher	14:11:50.23	+55:03:25.92	180	58599.3306	r	19.19
Thacher	14:24:30.89	+55:45:00.00	180	58599.3385	r	18.43
Thacher	14:28:58.08	+54:01:03.72	180	58599.3411	r	18.31
Thacher	14:37:21.26	+46:44:32.64	180	58599.3468	r	18.81
Thacher	14:39:22.49	+46:44:33.72	180	58599.3494	r	19.53
Thacher	14:32:55.75	+53:19:32.88	180	58599.3519	r	18.70
Thacher	14:59:56.71	+43:16:40.08	180	58599.3625	r	19.32
Thacher	15:06:34.54	+40:30:22.32	180	58599.3677	r	19.30
Thacher	15:17:40.13	+42:35:07.44	180	58599.3757	r	18.80
Thacher	15:26:28.80	+48:28:31.80	180	58599.3810	r	18.89
Thacher	15:33:21.17	+44:39:50.76	180	58599.3863	r	18.97

Table 4.2 (cont'd)

Source[a]	α (J2000)	δ (J2000)	Exposure Time (s)	Date[b] (MJD)	Filter	Magnitude Limit[c] (3σ)
Thacher	15:49:53.50	+41:53:31.92	180	58599.3970	r	19.18
Thacher	16:16:55.13	+50:33:13.68	180	58599.4159	r	19.86
Thacher	16:21:07.46	+49:51:38.88	180	58599.4186	r	20.12
Thacher	16:25:01.34	+40:51:09.72	180	58599.4213	r	19.59
Thacher	16:30:43.78	+41:32:45.96	180	58599.4269	r	19.59
Thacher	16:32:01.34	+50:12:28.44	180	58599.4297	r	19.94
Thacher	16:29:18.10	+48:49:21.72	180	58599.4324	r	19.31
Thacher	16:46:10.70	+21:47:57.84	180	58599.4359	r	19.77
Thacher	16:51:03.79	+23:11:07.08	180	58599.4387	r	19.95
Thacher	16:55:03.43	+25:57:26.28	180	58599.4416	r	20.01
Thacher	16:59:01.87	+28:02:10.32	180	58599.4444	r	20.00
Thacher	17:03:32.74	+24:13:28.92	180	58599.4472	r	19.53
Thacher	17:06:53.76	+24:55:03.72	180	58599.4500	r	19.86
Thacher	17:03:50.09	+24:55:05.52	180	58599.4529	r	19.95
Thacher	17:16:38.40	+15:54:34.20	180	58599.4558	r	19.85
Thacher	17:14:49.54	+08:38:04.92	180	58599.4587	r	19.73
Thacher	17:23:47.52	+00:19:05.88	180	58599.4615	r	19.62
Thacher	17:28:05.38	+03:26:13.92	180	58599.4644	r	19.68
Thacher	17:32:15.34	+03:26:13.20	180	58599.4672	r	19.69
Thacher	17:34:58.54	+02:44:38.04	180	58599.4700	r	19.67
Thacher	17:35:33.94	-07:18:13.32	180	58599.4756	r	19.74
Thacher	17:28:24.55	-06:15:48.24	180	58599.4813	r	19.62
Thacher	17:31:14.98	+06:33:24.84	180	58599.4843	r	19.68
Thacher	17:28:54.67	+08:58:56.64	180	58599.4872	r	19.32
Thacher	17:27:14.06	+07:35:47.04	180	58599.4900	r	19.64
Thacher	17:27:25.92	+08:38:08.88	180	58599.4928	r	19.72
Thacher	17:22:24.05	-00:43:07.32	180	58599.4956	r	19.42
Thacher	16:59:29.26	+49:55:29.64	60	58604.4423	r	19.48
Thacher	16:43:03.24	+36:49:57.72	60	58604.4441	r	19.30
Thacher	16:02:48.72	+19:48:09.72	60	58604.4489	r	19.30
Thacher	15:15:52.61	+56:20:02.40	60	58604.4510	r	19.39
Thacher	15:09:45.34	+57:00:20.52	60	58604.4522	r	19.33
Thacher	15:06:27.98	+55:46:06.60	60	58604.4534	r	19.34
Thacher	15:48:42.29	+21:53:07.44	60	58604.4555	r	18.96
Thacher	15:15:02.23	+42:03:07.56	60	58604.4613	r	19.26
Thacher	15:01:07.90	+44:42:02.88	60	58604.4625	r	19.32
Thacher	13:56:02.50	+59:44:49.20	60	58604.4639	r	18.78
Thacher	13:55:12.00	+59:30:40.32	60	58604.4651	r	19.10
Thacher	13:46:55.80	+60:58:38.28	60	58604.4663	r	19.23
Thacher	14:05:08.90	+55:44:44.52	60	58604.4674	r	19.41
Thacher	14:07:07.94	+55:00:18.00	60	58604.4686	r	19.13
Thacher	14:02:08.21	+55:49:03.72	60	58604.4697	r	18.30
Thacher	13:53:29.90	+40:17:13.56	60	58605.3007	r	19.30
Thacher	13:56:20.28	+47:14:23.64	60	58605.3020	r	19.37
Thacher	13:50:52.56	+39:34:47.28	60	58605.3034	r	19.08
Thacher	14:02:53.86	+49:10:37.56	60	58605.3062	r	19.23
Thacher	14:05:16.66	+55:44:47.04	60	58605.3099	r	19.37
Thacher	14:07:15.50	+55:00:21.24	60	58605.3111	r	19.62
Thacher	14:02:15.77	+55:49:07.32	60	58605.3124	r	19.53
Thacher	13:56:10.78	+59:44:48.84	60	58605.3136	r	18.41
Thacher	13:55:19.87	+59:30:42.48	60	58605.3148	r	19.02
Thacher	13:47:03.89	+60:58:43.68	60	58605.3160	r	19.33

Table 4.2 (cont'd)

Source[a]	α (J2000)	δ (J2000)	Exposure Time (s)	Date[b] (MJD)	Filter	Magnitude Limit[c] (3σ)
Thacher	14:23:28.75	+01:44:01.32	60	58605.3204	r	18.70
Thacher	14:29:42.12	+03:14:28.68	60	58605.3240	r	18.86
Thacher	14:27:39.19	+41:15:44.28	60	58605.3273	r	19.36
Thacher	14:27:31.46	+46:09:03.96	60	58605.3285	r	19.41
Thacher	14:20:43.75	+39:41:52.80	60	58605.3299	r	19.21
Thacher	14:37:54.77	-00:23:26.88	60	58605.3317	r	18.79
Thacher	14:44:57.58	+01:57:45.72	60	58605.3359	r	18.62
Thacher	13:29:58.70	+47:16:11.64	60	58605.3441	r	19.51
Thacher	15:01:11.86	+44:42:09.72	60	58605.3552	r	19.49
Thacher	15:09:51.14	+57:00:14.40	60	58605.3566	r	19.19
Thacher	15:06:33.55	+55:46:03.00	60	58605.3579	r	19.47
Thacher	15:15:57.96	+56:19:56.64	60	58605.3591	r	19.44
Thacher	15:15:05.98	+42:03:13.68	60	58605.3605	r	19.35
Thacher	15:21:33.79	-07:22:10.92	60	58605.3624	r	18.76
Thacher	13:29:51.58	+47:11:53.88	60	58605.3693	r	19.27
Thacher	13:30:10.20	+46:40:25.32	60	58605.3705	r	18.72
Thacher	16:53:57.02	+39:45:32.04	45	58605.3918	V	18.95
Thacher	16:53:56.98	+39:45:32.04	45	58605.3925	V	19.00
Thacher	16:53:56.95	+39:45:32.04	45	58605.3932	V	18.92
Thacher	16:53:56.95	+39:45:32.40	45	58605.3939	V	19.00
Thacher	16:53:56.98	+39:45:32.40	45	58605.3946	V	18.99
Thacher	16:02:49.78	+19:47:44.52	60	58605.3988	r	19.21
Thacher	15:48:42.82	+21:52:45.84	60	58605.4015	r	18.91
Thacher	13:28:23.35	+46:35:40.20	60	58605.4050	r	19.30
Thacher	13:53:18.38	+33:30:23.76	60	58605.4074	r	18.88
Thacher	13:42:06.84	+35:39:18.72	60	58605.4114	r	19.31
Thacher	12:25:07.54	+54:30:31.68	60	58605.4153	r	19.36
Thacher	13:15:47.04	+42:01:51.96	60	58605.4167	r	19.43
Thacher	12:54:34.70	+46:31:59.52	60	58605.4178	r	19.40
Thacher	16:59:30.36	+49:55:32.16	60	58605.4290	r	19.44
Thacher	16:43:03.00	+36:49:58.08	60	58605.4557	r	19.04
Thacher	13:29:45.86	+47:11:32.64	300	58606.2833	g	19.47
Thacher	13:29:44.66	+47:11:35.52	300	58606.2941	r	20.23
Thacher	13:29:43.56	+47:11:36.24	300	58606.3051	i	19.66
Thacher	13:29:42.74	+47:11:34.80	300	58606.3160	z	18.43
Thacher	13:53:28.27	+40:16:40.44	120	58606.3302	g	19.50
Thacher	13:53:28.22	+40:16:40.44	120	58606.3317	g	19.40
Thacher	13:53:28.20	+40:16:40.08	120	58606.3333	g	19.38
Thacher	13:53:28.15	+40:16:40.44	120	58606.3349	r	19.69
Thacher	13:53:28.08	+40:16:40.44	120	58606.3364	r	19.64
Thacher	13:53:28.03	+40:16:40.44	120	58606.3380	r	19.66
Thacher	13:53:27.98	+40:16:40.08	120	58606.3396	i	19.36
Thacher	13:53:28.01	+40:16:40.08	120	58606.3412	i	19.22
Thacher	13:53:27.91	+40:16:39.72	120	58606.3427	i	19.28
Thacher	13:53:27.98	+40:16:39.72	120	58606.3443	z	17.98
Thacher	13:53:27.89	+40:16:39.72	120	58606.3459	z	17.96
Thacher	13:53:27.89	+40:16:39.72	120	58606.3474	z	17.94
Thacher	16:59:30.10	+49:55:32.52	60	58606.4294	r	19.56
Thacher	16:43:03.17	+36:50:03.12	60	58606.4325	r	19.61
Thacher	16:02:48.48	+19:48:05.76	60	58606.4346	r	19.35
Thacher	15:15:53.11	+56:20:04.92	60	58606.4379	r	19.49
Thacher	15:09:45.98	+57:00:23.04	60	58606.4391	r	19.39

Table 4.2 (cont'd)

Source[a]	α (J2000)	δ (J2000)	Exposure Time (s)	Date[b] (MJD)	Filter	Magnitude Limit[c] (3σ)
Thacher	15:06:28.49	+55:46:08.76	60	58606.4403	r	19.65
Thacher	15:48:42.34	+21:53:08.52	60	58606.4424	r	19.02
Thacher	15:15:02.14	+42:03:09.36	60	58606.4518	r	19.38
Thacher	15:01:08.04	+44:42:05.76	60	58606.4530	r	19.33
Thacher	13:56:02.33	+59:44:49.92	60	58606.4543	r	18.93
Thacher	13:55:11.90	+59:30:42.48	60	58606.4555	r	19.03
Thacher	13:46:55.75	+60:58:41.52	60	58606.4567	r	19.43
Thacher	14:05:08.90	+55:44:47.40	60	58606.4579	r	19.26
Thacher	14:07:07.87	+55:00:21.60	60	58606.4591	r	19.46
Thacher	14:02:08.06	+55:49:06.60	60	58606.4602	r	19.43
Thacher	14:00:38.26	+55:10:07.32	60	58606.4614	r	19.41
Thacher	14:04:58.03	+53:39:58.68	60	58606.4625	r	19.42
Thacher	14:27:26.02	+46:08:58.20	60	58606.4638	r	19.43
Thacher	14:06:18.19	+50:43:42.96	60	58606.4649	r	19.44
Thacher	14:02:46.73	+49:10:32.52	60	58606.4660	r	19.45
Thacher	14:27:34.30	+41:15:37.80	60	58606.4672	r	19.42
Thacher	13:56:13.39	+47:14:18.60	60	58606.4684	r	19.17
Thacher	14:20:40.82	+39:41:45.60	60	58606.4696	r	19.41
Thacher	11:39:24.36	+46:31:03.72	60	58607.2007	r	19.10
Thacher	11:46:00.12	+50:12:18.36	60	58607.2078	r	19.02
Thacher	11:57:39.77	+53:22:46.20	60	58607.2166	r	19.32
Thacher	12:10:02.02	+46:27:42.48	60	58607.2240	r	19.11
Thacher	12:16:15.07	+47:53:18.60	60	58607.2302	r	19.11
Thacher	13:15:51.67	+42:02:05.28	60	58607.2737	r	19.54
Thacher	12:54:38.78	+46:32:15.72	60	58607.2750	r	19.55
Thacher	13:30:14.88	+46:40:32.52	60	58607.2789	r	19.07
Thacher	13:30:03.00	+47:16:15.96	60	58607.2801	r	19.55
Thacher	13:50:50.71	+39:34:30.36	60	58607.2934	r	19.48
Thacher	13:53:31.49	+40:16:52.32	120	58607.2974	g	19.03
Thacher	13:53:31.08	+40:16:53.40	120	58607.2989	g	18.84
Thacher	13:53:30.77	+40:16:52.68	120	58607.3004	g	19.22
Thacher	13:53:30.58	+40:16:50.52	120	58607.3020	r	19.60
Thacher	13:53:30.19	+40:16:50.16	120	58607.3035	r	19.70
Thacher	13:53:29.88	+40:16:49.80	120	58607.3051	r	19.68
Thacher	13:53:29.64	+40:16:49.80	120	58607.3067	i	19.32
Thacher	13:53:29.42	+40:16:49.08	120	58607.3082	i	19.29
Thacher	13:53:29.23	+40:16:48.36	120	58607.3098	i	19.34
Thacher	13:53:29.02	+40:16:47.64	120	58607.3114	z	18.24
Thacher	13:53:28.87	+40:16:46.92	120	58607.3129	z	18.26
Thacher	13:53:28.75	+40:16:46.20	120	58607.3145	z	18.29
Thacher	14:23:28.85	+01:44:05.64	60	58607.3184	r	18.90
Thacher	14:29:42.19	+03:14:31.56	60	58607.3196	r	18.91
Thacher	14:37:54.98	-00:23:26.88	60	58607.3244	r	18.85
Thacher	14:40:58.06	-00:18:36.72	60	58607.3269	r	18.87
Thacher	14:27:30.65	+46:09:07.56	60	58607.3288	r	19.41
Thacher	14:27:37.61	+41:15:47.16	60	58607.3301	r	19.45
Thacher	14:44:57.72	+01:57:47.88	60	58607.3319	r	18.88
Thacher	14:07:13.18	+55:00:26.28	60	58607.3338	r	19.56
Thacher	14:05:14.16	+55:44:52.44	60	58607.3350	r	19.65
Thacher	14:02:13.22	+55:49:12.36	60	58607.3389	r	19.43
Thacher	15:09:50.95	+57:00:15.12	60	58607.3513	r	19.24
Thacher	15:06:33.31	+55:46:03.72	60	58607.3525	r	19.43

Table 4.2 (cont'd)

Source[a]	α (J2000)	δ (J2000)	Exposure Time (s)	Date[b] (MJD)	Filter	Magnitude Limit[c] (3σ)
Thacher	15:15:57.86	+56:19:57.00	60	58607.3538	r	19.37
Thacher	15:15:05.90	+42:03:17.28	60	58607.3551	r	19.42
Thacher	15:01:10.94	+44:42:14.04	60	58607.3564	r	19.37
Thacher	15:21:33.91	-07:22:08.76	60	58607.3596	r	18.83

Note. — We only include data that 1M2H acquired and reduced. For LCO data referred to in section 4.2, these data will be published in Keinan et al. (in prep.). For all other data, see the curated pointings on the Treasure Map (Wyatt et al. 2020).

[a]Imaging as described in section 4.2.

[b]MJD is taken from the center of the exposure time.

[c]In-band 3σ limit for the reported image as described in section 4.2 and section 4.6. All magnitudes are on the AB system (Oke & Gunn 1983).

4.11 `Teglon` Implementation

4.11.1 Galaxy Catalog & Completeness Calculation

In O3, 1M2H used the GLADE catalog of galaxies for EM search, follow-up, and analysis of GW events (Kilpatrick et al. 2021) because it is much more complete than the GWGC at the LVC O3 median BNS inspiral range, and completely subsumes the GWGC containing $\sim 3 \times 10^6$ galaxies, $\sim 3 \times 10^5$ quasars, and ~ 150 globular clusters. GLADE combines and cross-matches sources from the GWGC, the HyperLEDA catalog (Makarov et al. 2014), the 2 Micron All-Sky Survey Extended Source Catalog (Skrutskie et al. 2006), the 2MASS Photometric Redshift Catalog (Bilicki et al. 2014), and the DR12 Sloan Digital Sky Survey quasar catalog (Pâris et al. 2017). Within GLADE, there is a notable anisotropy in the spatial distribution of galaxies (see Fig. 1 in Dálya et al. 2018) caused by the clustering of the galaxies themselves, the lack of galaxies detected along the plane of the Milky Way, and an increase in the number density of galaxies associated with each component survey (HyperLEDA contributes ∼2.6M

sources alone). `Teglon` seeks to take advantage of this anisotropy, using it to inform where we should pivot our search strategy to galaxy targeting from localization tiling, and we introduce a spatially varying completeness metric to quantify it.

To compute this metric, we transformed the GLADE catalog from an ASCII text file into a MySQL database, where every column within the original GLADE catalog is represented as a field in the Galaxy table of the database. We then define an adaptive, all-sky grid using the Hierarchical Equal Area isoLatitude Pixelization (HEALPix)[39] (Górski et al. 2005b) sky-discretization method, both because LVC sky maps use that format to communicate distance and probability information (Singer & Price 2016; Singer et al. 2016b), and because the equal-area pixels within HEALPix allow us to partition the galaxies in the catalog in a uniform way. This grid is 3D, and we define volume pixels, or "voxels," as parallelepipeds where each voxel face in the plane of the sky is defined by a HEALPix pixel, and its radial edges extend out to the next voxel face (see Figure 4.9). We adapt the HEALPix resolution and distance between voxel faces so that each voxel contains an approximately equal co-moving volume, $\sim$1.5 Gpc^3. This 3D grid is bound within $D \in [0, 1200]$ Mpc, with pixel resolutions ranging from $N_{\rm side} = 2$ for the closest pixels, to $N_{\rm side} = 128$ for the most distant, resulting in 196,608 unique sight-lines through the database. Each galaxy within $D \leq 1.2$ Gpc is then registered to its enclosing voxel. Finally, for each $N_{\rm side} = 128$ sight-line, we ingest the Milky Way (MW) $E(B-V)$ reddening value using an "`SFD query`" (Schlegel et al. 1998) from the `dustmaps`[40] tool (Green 2018b), which can be converted into passband-specific extinction values derived from Schlafly & Finkbeiner (2011).

We wish to obtain a completeness scalar, C, where we define C as the quotient between

[39] https://healpix.sourceforge.io/
[40] https://dustmaps.readthedocs.io/en/latest/index.html

the luminosity density of the voxel divided by the expected luminosity density in the local universe. Each ith voxel is a unique combination of celestial position and distance, and so $C_i = C(\alpha_i, \delta_i, D_{L_i})$. To compute C_i, we retrieve j galaxies from the ith voxel and convert every jth galaxy's B-band magnitude, m_j, to a B-band luminosity using its distance, D_j (in Mpc), and B-band line of sight extinction, λ_j,

$$\mu_j = 5\log_{10}(D_j) + 25, \tag{4.2}$$

$$L_j = 10^{-0.4(m_j - \mu_j - \lambda_j)}. \tag{4.3}$$

Summing over j gives the total enclosed voxel luminosity. To conveniently compare these luminosities to the fiducial luminosity density calculated in Kopparapu et al. (2008), we adopt their unit of $L_{10} \equiv 10^{10} L_{B,\odot}$, where $L_{B,\odot} = 2.16 \times 10^{33}$ ergs/s, and $L_{B,\odot}$ is calculated using $M_{B,\odot} = 5.48$ from Binney & Tremaine (2008),

$$L_{10_i} = \frac{\sum_j L_j}{L_{B,\odot} \times 10^{10}}. \tag{4.4}$$

Dividing L_{10_i} by the ith voxel's volume, V_i, results in the ith voxel's B-band luminosity density, which in turn is divided by a blue luminosity density of $(1.98 \pm 0.16) \times 10^{-2} L_{10}$ Mpc^3 (Kopparapu et al. 2008) to obtain the "uncorrected" completeness value for that voxel. Because these completeness values are calculated based on an average blue luminosity density, nearby voxels ($D \leq 40$ Mpc) can fluctuate above 100% due to the local overdensity of galaxies around the MW. Furthermore, our 3D grid is coarsely binned at close-in distances, and directly adjacent

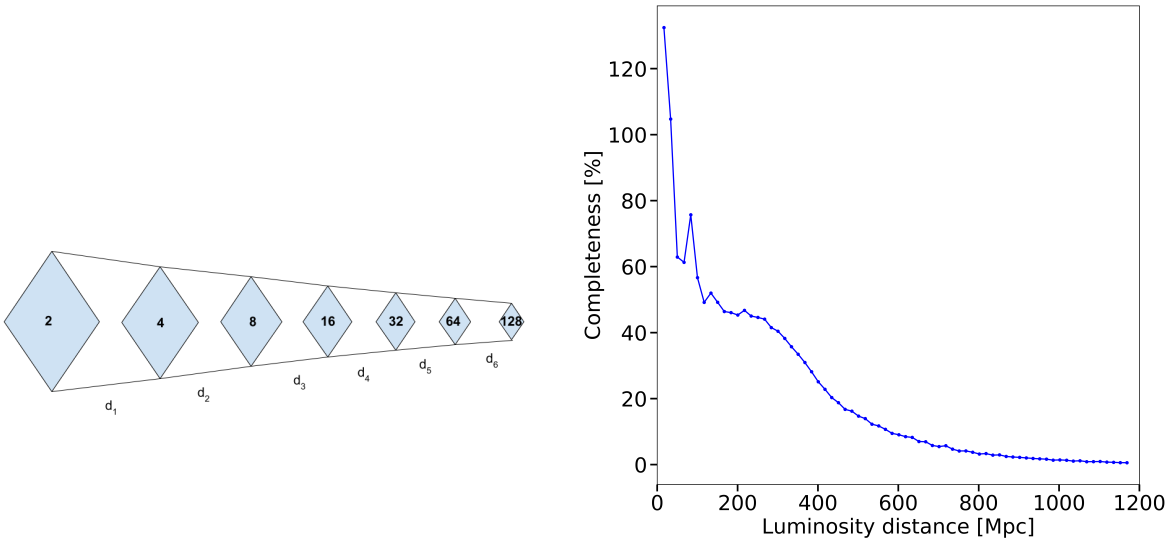

Figure 4.9 *Left* Simplified schematic of the resolution and distance steps through a sight-line in the `Teglon` sky pixel grid. *Right* For a given sight line, the uncorrected completeness values are calculated from the enclosed voxel blue luminosity.

pixels can have discontinuous completeness values which reflect this numerical effect. Since we wish to use these completeness values as weights in our search algorithm, we rectify these values in two ways: first, we cap the completeness at 1.0, and second, we use a Gaussian symmetric beam in the `healpy` library[41] (Zonca et al. 2019c; Górski et al. 2005c) with a 30-Mpc radius to smooth pixels at each distance step. The all-sky completeness map at the enclosing distance bin of GW190425 is shown in Figure 4.10.

4.11.2 Completeness-Weighted 2D Probability Redistribution

When the LVC detects a GW merger event that can be matched to a GW template, the LVC performs a rapid parameter estimation of the system, including a rapid reconstruction of the event's 3D position (Singer & Price 2016). This position posterior is sampled on an adaptive

[41] https://healpy.readthedocs.io/en/latest/index.html

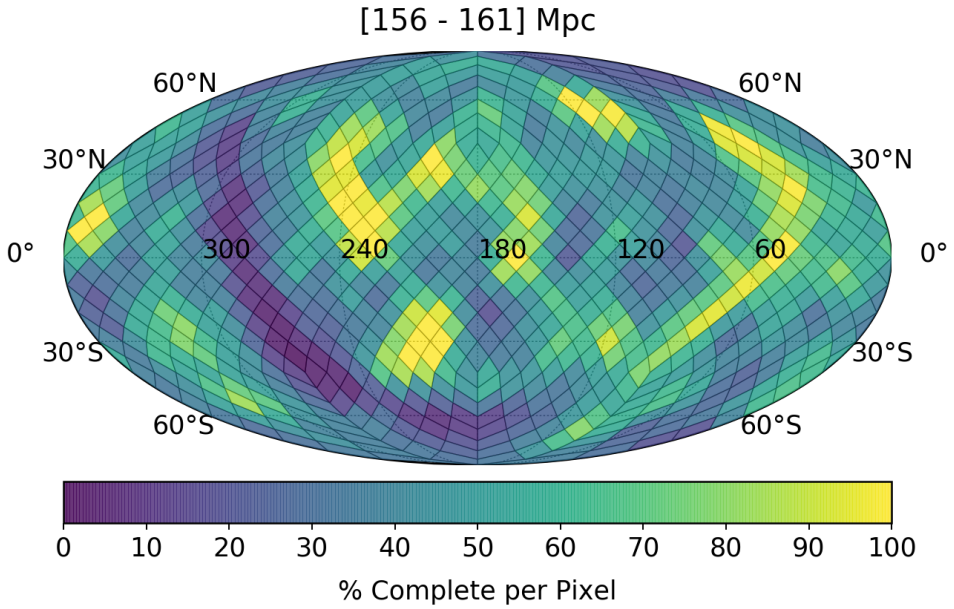

Figure 4.10 All sky completeness visualization from `Teglon` for the distance bin corresponding to GW190425's luminosity distance, $\sim$ 159 Mpc. The horseshoe-shaped feature of systematically lower completeness corresponds to the Milky Way.

HEALPix grid, which during O3, was flattened and broadcast to the scientific community. For these events, every pixel within the HEALPix map contains a distance distribution and a marginalized 3D probability projected onto that 2D pixel.

`Teglon` reads in such a localization map, and for a map with k pixels, retrieves each pixel's (Pix_k) mean distance, D_k, celestial position, (α_k, δ_k), and 2D probability, P_{2D_k}, and resolves these to a completeness weight, $C_k = C(\alpha_k, \delta_k, D_k)$. If this weight is 1.0, this is akin to 100% completeness, and we assume that all of those galaxies are registered within `Teglon`'s voxels. If the weight is 0.0, then the opposite is true. Therefore, `Teglon` *decrements* the pixel's 2D probability, P_{2D_k}, instead adding it to a running budget of probability that will be distributed over all of the galaxies in the database. The original kth pixel's probability is decremented to a new one, P'_{2D_k},

$$P'_{2\mathrm{D}_k} = P_{2\mathrm{D}_k} \times (1.0 - C_k)\,, \tag{4.5}$$

$$P_{\mathrm{gals}} = \sum_k (P_{2\mathrm{D}_k} \times C_k)\,. \tag{4.6}$$

`Teglon` distributes P_{gals} over all galaxies in the database according to the weighting scheme introduced in Coulter et al. (2017a), reproduced here for convenience[42]. First, each Pix_k contains g galaxies, and each galaxy has a luminosity distance, $D_{k,g}$, and an apparent B magnitude, $m_{k,g}$. Based on these quantities, we compute a luminosity weight, $\tilde{L}_{k,g}$, which is determined based on its luminosity distance,

$$\tilde{L}_{k,g} = D_{k,g}^2 10^{-0.4 m_{k,g}} \tag{4.7}$$

Each galaxy within a pixel also has a distance weight, $\tilde{D}_{k,g}$, calculated based on the difference between $D_{k,g}$ and D_k, where a large difference yields a smaller weight,

$$\tilde{D}_{k,g} = \left(1 - \mathrm{erf}\left(\sqrt{\frac{(\mathrm{D_{k,g}} - \mathrm{D_k})^2}{\sigma^2_{\mathrm{D_{k,g}}} + \sigma^2_{\mathrm{D_k}}}}\right)\right). \tag{4.8}$$

For each contained galaxy, Pix_k's original 2D probability, $P_{2\mathrm{D}_k}$, is also used as a weight. These weights are combined to produce the ranking for each galaxy, $W_{k,g}$, where n is a normalizing factor. The product of $W_{k,g}$ and P_{gals} is the fraction of probability assigned to the gth galaxy within the kth pixel, $P_{k,g}$,

[42]Note, we correct Equation 4.8 from Coulter et al. (2017a) Equation S2 to make the argument of the Error Function dimensionless

$$W_{k,g} = n^{-1} \times \tilde{L}_{k,g} \times P_{\mathrm{2D}_k} \times \tilde{D}_{k,g}, \tag{4.9}$$

$$P_{k,g} = W_{k,g} \times P_{\mathrm{gals}}. \tag{4.10}$$

Finally, for each Pix_k, all contained galaxy probabilities are summed with $P^{'}_{\mathrm{2D}_k}$ to produce the final pixel probability, $P^{''}_{\mathrm{2D}_k}$,

$$P^{''}_{\mathrm{2D}_k} = P^{'}_{\mathrm{2D}_k} + \sum_g P_{k,g}. \tag{4.11}$$

This transform redistributes the probability in the map proportional to each pixel's completeness and *concentrates* probability in regions that contain luminous galaxies within the GW-derived luminosity distance interval. This creates a new `Teglon`-version of the map that conserves the total probability in the original map,

$$\sum_k P^{''}_{\mathrm{2D}_k} = \sum_k P_{\mathrm{2D}_k} = 1.0. \tag{4.12}$$

4.11.3 Pixel-Level Upper Limits Calculations

`Teglon` leverages the HEALPix data format to compute model detection efficiencies at the pixel level. We model each instrument referenced in Section 4.2 as a collection of polygons, and together with the celestial coordinates of every pointing in Table 4.10, use the `healpy` library to return every pixel covered by these observations from the final localization map for GW190425.

To calculate an upper limit, we consider two types of quantities: those that are temporally invariant, and those that change with each observation. Section 4.11.2 describes the invariant properties, P''_{2D}, D, σ_D, and $E(B-V)$. Mutable properties are dependent on each image in our manifest: filter, λ; MJD, t; and limiting magnitude, $m(t,\lambda)$.

Considering the footprint of all images of filter λ at time t, there are i enclosed pixels; for each we can consider an arbitrary model light curve, $M(t,\lambda) = M_\lambda(t)$, and calculate the maximum distance $D_{i,M,\lambda}(t)$ that it could be detected in i given $m_i(t,\lambda) = m_{i,\lambda}(t)$,

$$\mu_{i,M,\lambda}(t) = m_{i,\lambda}(t) - M_\lambda(t) - A_{i,\lambda}, \tag{4.13}$$

$$D_{i,M,\lambda}(t)\ [\mathrm{Mpc}] = 10^{0.2\times(\mu_{i,M,\lambda}(t)-25)}, \tag{4.14}$$

where $\mu_{i,M,\lambda}(t)$ is the corresponding distance modulus. We use $D_{i,M,\lambda}(t)$ as a limit of integration on the pixel's distance distribution, normalizing by the resampled pixel's 2D probability, P''_{2D_i},

$$P_{i,M,\lambda}(t) = \frac{nP''_{\mathrm{2D}_i}}{\sigma_{D_i}} \int_0^{D_{i,M,\lambda}(t)} e^{-\frac{1}{2}\left(\frac{D-D_i}{\sigma_{D_i}}\right)} dD, \tag{4.15}$$

where $P_{i,M,\lambda}(t)$ is the ith imaged pixel's contribution to detecting $M_\lambda(t)$, and n is a normalizing constant such that Equation 4.15 integrates to P''_{2D_i} from $[0,\infty)$.

To calculate the combined detection efficiency of $M_\lambda(t)$ across all t for i, we take the complement of the product of the complements (i.e., the chances we detect the model in at least *one* epoch is equal to the complement of not detecting the model in *any* epochs). Summing over i yields the probability of detecting $M_\lambda(t)$,

$$P_{M,\lambda} = \sum_i P''_{\mathrm{2D}_i} \left[1 - \prod_t \left(1 - \frac{P_{i,M,\lambda}(t)}{P''_{\mathrm{2D}_i}} \right) \right]. \tag{4.16}$$

To combine the detection efficiency of multiple filters for a model, $M(\lambda)$, we sum the resampled 2D probability for all pixels covered by any observation,

$$P_{\mathrm{obs}} = \sum_i P''_{\mathrm{2D}_i}, \tag{4.17}$$

and repeat the process in Equation 4.16,

$$P_M = P_{\mathrm{obs}} \left[1 - \prod_\lambda \left(1 - \frac{P_{M,\lambda}}{P_{\mathrm{obs}}} \right) \right]. \tag{4.18}$$

Chapter 5

Summary and Future Directions

In this work I have discussed three projects that have helped to unlock the potential of real-time transients, as well as multimessenger astrophysics. In Chapter 2, I presented `YSE-PZ`, an open-source, portable, and well-documented transient survey management platform. `YSE-PZ` has been built to ingest public and private data from a variety of sources, and includes an API to allow both human- and machine-initiated jobs to retrieve transients, as well as transient and host photometry and spectra. `YSE-PZ` also provides a plethora of tools to allow humans to make better decisions in real-time to facilitate follow-up resource allocation, define scientific samples of interest (e.g., Aleo et al. 2022), and to act as a repository for on going survey data and metadata.

Rather than automating out human interaction, `YSE-PZ` focuses on accelerating and enhancing human decision making, and I showed how `YSE-PZ` enables three major on-going transient surveys: the Young Supernova Experiment (Jones et al. 2021), the Keck Infrared Transient Survey (Tinyanont et al., in prep), and the Swope Supernova Survey (Rojas-Bravo

et al., in prep). Together, YSE-PZ currently serves over 200 active users, holds over 130,000 transients, $> 5 \times 10^6$ photometric data points, and > 16000 spectra, and has supported > 30 scientific papers with more on the way (Fulton et al. 2023; Angus et al. 2022; Aleo et al. 2022; Davis et al. 2022; Ward et al. 2022; Kilpatrick et al. 2022b; Pastorello et al. 2022; Jacobson-Galán et al. 2022b; Tinyanont et al. 2022; Dimitriadis et al. 2022; Gagliano et al. 2022; Jacobson-Galán et al. 2022a; Dettman et al. 2021; Kilpatrick et al. 2021; Wang et al. 2021; Armstrong et al. 2021; Jencson et al. 2021; Barna et al. 2021; Jones et al. 2021; Hinkle et al. 2021; Holoien et al. 2020; Hung et al. 2020; Jacobson-Galán et al. 2020a,b; Neustadt et al. 2020; Dimitriadis et al. 2019a; Jones et al. 2019; Li et al. 2019; Kilpatrick et al. 2018a,b; Tartaglia et al. 2018).

Looking forward, YSE-PZ is continually being updated with new tools and new functionality. In a forthcoming update, YSE-PZ will use ParSNIP to classify transients[43], and the application itself is now being adapted for use in fast radio burst science by the Fast and Fortunate for FRB Follow-up research group[44]. Finally, although YSE-PZ is effective for the use cases that it currently supports, next-generation, high-volume transient surveys such as Vera C. Rubin Observatory Legacy Survey of Space and Time (LSST Science Collaboration et al. 2009a) will discover $\sim 10^5$ bone fide transients a year — almost an order of magnitude increase from our current transient ingestion rate. For YSE-PZ to stay capable, I will be working to leverage advances in machine learning approaches to automatic transient classification (e.g., Boone 2021; Burhanudin & Maund 2022), new messaging protocols like Apache Kafka[45], and citizen science platforms (e.g., Christy et al. 2022; Zevin et al. 2017) to further empower human-in-the-loop decision making at scale.

[43] https://parsnip.readthedocs.io/en/latest/
[44] https://sites.google.com/ucolick.org/f-4/home
[45] https://kafka.apache.org/

In Chapter 3, I presented the discovery of the first optical counterpart to a gravitational wave source, the KN SSS17a/AT 2017gfo. This discovery marked a new beginning of gravitational and electromagnetic astronomy, and lead to fundamental advances in the demographics of neutron stars (Abbott et al. 2019a), the maximum density of nuclear material (Capano et al. 2020), the speed of gravity (Baker et al. 2017), tests of general relativity in the strong field regime (Abbott et al. 2019b), and cosmology (Abbott et al. 2017d), among others.

In discovering SSS17a/AT 2017gfo and localizing it to its host galaxy, NGC 4993, we set the stage for conclusively showing that BNS mergers are prolific astrophysical sites for the synthesis of the r-process elements (Kilpatrick et al. 2017; Drout et al. 2017). Despite the rapid localization of AT 2017gfo, our team still took nearly 12 hours to locate it, and in that time critical information was lost about the complete nature of its early-time blue component (Arcavi 2018), or whether elements heavier than the lanthanides (i.e., the actinides $88 < \mathrm{Z} < 104$) were created. Finding the next counterpart will help address these gaps in our understanding, but also point to the fact that we must be even faster if we want to push into the critical first few hours of a KN's evolution.

Finally, In Chapter 4, I presented a new UVOIR search for the second-ever, BNS merger detected in GWs, GW190425. In our Gravity Collective search, we report on a novel, 31.5 deg^2 survey in $uBVgriIzJHK$, across four small-aperture telescopes as part of the One-Meter, Two-Hemispheres (1M2H) team. Despite an extensive search campaign by ourselves and the wider EM community, no counterpart was discovered.

Part of the reason for this was likely due to the astrophysics behind the remnant itself. GW190425's total system mass was much more massive than that of GW170817, and in fact,

more massive than any known BNS system in the Milky Way (Abbott et al. 2020c). Weighing in at a total system mass of $3.4^{+0.3}_{-0.1}\,M_{\odot}$, it is likely that this merger remnant exceeded the maximum mass of a NS, the Tolman–Oppenheimer–Volkoff mass, or M_{TOV} (Oppenheimer & Volkoff 1939; Tolman 1939). Current estimates for this mass must be bounded from below by the most massive known millisecond pulsar, J0740+6620 ($M_{\rm J0740} = 2.14^{+0.10}_{-0.09}$ M$_{\odot}$; Cromartie et al. 2020), and from above by the total mass of the remnant from GW170817 ($M_{\rm GW170817} = 2.74^{+0.04}_{-0.01}$ M$_{\odot}$; Abbott et al. 2017a) which is thought to have eventually collapsed into a BH. Currently this value resides in the range of $\lesssim$ 2.1—2.3 M$_{\odot}$ (Margalit & Metzger 2017; Shibata et al. 2017; Ruiz et al. 2018; Ai et al. 2020). Therefore, it is reasonable to assume that the remnant of GW190425 directly collapsed to a BH.

We considered the ramifications of this direct collapse — both in terms of the expected observables and in the expected nucleosynthesis. Both are linked, and we would expect such an EM counterpart to be very red, due to the fact that the the BH remnant itself would not be providing the neutrinos necessary to convert low Y_e material to higher Y_e material, and thus producing heavier isotopes with larger opacities that would shift most of the emission to the infrared. Therefore, this merger was unlikely to produce the same light elements inferred from AT 2017gfo's blue component, and perhaps even contributed to the formation of the actinides or possibly even "superheavey" isotopes (Z $\geq$ 104; Holmbeck et al. 2023).

In addition to the intrinsically low luminosity, red, and quickly evolving speculative KN associated with GW190425, finding this counterpart was challenging from the start from its enormous localization. To make the most of the data that did get taken, by our team and the entire EM community, I performed a joint meta-analysis of $\sim$ 3600 images to produce the best

constraints on a KN counterpart to GW190425 to date. To perform this analysis, I presented a new tool for the community called `Teglon`. At its heart, `Teglon` creates a novel interpolation between the galaxy-targeting strategies that were successful for localizing AT 2017gfo, and a tessellating, or "tiling" approach to covering large localizations with adjacent telescope FOVs. `Teglon` also has the benefit of resampling the LVK probability maps, concentrating probability proportional to the presence of cataloged galaxies at the right 3D position, and effectively boosting the performance of small FOV telescopes. Nevertheless, GW190425's location was constrained to nearly one quarter of the sky, with nearly half of its area too near the Sun for extensive ground-based follow-up, which resulted in the absolute limits placed on *any* counterpart model to be bounded by the localization coverage that the community was able to achieve (i.e., a `Teglon` resampled 39%). Despite this, we can rule out an AT 2017gfo-like blue KN to $\sim 25\%$.

We are now in the LVK's fourth observing run, and it has been nearly 6 years since the first optical counterpart to a GW source has been discovered. In the time since the discovery of AT 2017gfo, new NS-bearing GW events, like GW190425 and the NSBH mergers GW200105 and GW200115 (Abbott et al. 2021b) have opened the door to new and more diverse merger scenarios. To understand the full picture of NS-mergers, their nucleosynthetic products, and ultimately their imprint on the r-process abundances we observe in nature, it is required that we find more events and follow-up on them across the EM spectrum — especially in the near, mid, and far-infrared.

In the near term, approved Cycle 2 *JWST* programs, for which I am a Co-I, will provide invaluable opportunities to study the emission of the next KN in the infrared. IR spectra for AT 2017gfo did not go redder than $\sim 2.5\ \mu m$, and many broad spectral features remained

unidentified and did not perfectly match models (Tanvir et al. 2017; Pian et al. 2017; Chornock et al. 2017). Excitingly, we now have the possibility of obtaining an infrared spectrum out to 5 microns — which might unlock the exact elemental abundances of the ejecta that have hitherto remained a mystery. Furthermore, while AT 2017gfo's blue component was a surprise and may be conditional on the total system mass of the merger, the prediction that KNe always have a red component is robust. In NOIRLab's Semester 23B, I have been provisionally awarded a portion of the Science Verification time of the newly recommissioned NEWFIRM IR instrument installed on the Blanco 4 m telescope at the Cerro Tololo Inter-American Observatory to search for a BNS counterpart. NEWFIRM's field of view (FOV; ~ 0.22 deg^2) is large for NIR detectors, and together with `Teglon`, can realistically discover a KN to the LVK BNS horizon distance (~ 200 Mpc) in O4. Therefore, once NEWFIRM is fully online, it will be a vital resource that can be a KNe discovery engine regardless of a BNS mergers distance, viewing angle, (most) dust reddening, and lanthanide fraction. Despite KNe being intrinsically faint, the future for finding another KN, and answering fundamental questions about the original and abundances of the r-process elements, is bright.

Bibliography

Abadi M., et al., 2016, arXiv e-prints, p. arXiv:1603.04467

Abazajian K. N., et al., 2009, ApJS, 182, 543

Abbott B. P., et al., 2016a, Physical Review X, 6, 041015

Abbott B. P., et al., 2016b, Living Reviews in Relativity, 19, 1

Abbott B. P., et al., 2016c, Physical Review Letters, 116, 061102

Abbott B. P., et al., 2016d, Phys. Rev. Lett., 116, 221101

Abbott B. P., et al., 2016e, Physical Review Letters, 116, 241103

Abbott B. P., et al., 2016f, Astrophys. J. , 826, L13

Abbott B. P., et al., 2017a, Physical Review X

Abbott B. P., et al., 2017b, Phys. Rev. Lett., 118, 221101

Abbott B. P., et al., 2017c, Phys. Rev. Lett., 119, 141101

Abbott B. P., et al., 2017d, 4, 551, 85

Abbott B. P., et al., 2017e, ApJ, 851, L35

Abbott T. M. C., et al., 2018, ApJS, 239, 18

Abbott B. P., et al., 2019a, Physical Review X, 9, 011001

Abbott B. P., et al., 2019b, Phys. Rev. Lett., 123, 011102

Abbott B. P., et al., 2020a, Living Reviews in Relativity, 23, 3

Abbott R., et al., 2020b, Phys. Rev. Lett., 125, 101102

Abbott B. P., et al., 2020c, ApJ, 892, L3

Abbott R., et al., 2021a, Physical Review X, 11, 021053

Abbott R., et al., 2021b, ApJ, 915, L5

Ai S., Gao H., Zhang B., 2020, ApJ, 893, 146

Alard C., 2000, Astron. Astrophys. Suppl. Ser. , 144, 363

Aldering G., et al., 2002, in Tyson J. A., Wolff S., eds, Society of Photo-Optical Instrumentation Engineers (SPIE) Conference Series Vol. 4836, Survey and Other Telescope Technologies and Discoveries. pp 61–72, doi:10.1117/12.458107

Aleo P. D., et al., 2022, arXiv e-prints, p. arXiv:2211.07128

Alexander K. D., et al., 2018, ApJ, 863, L18

Angus C. R., et al., 2022, Nature Astronomy, 6, 1452

Annis J., et al., 2014, ApJ, 794, 120

Antier S., et al., 2020, MNRAS, 492, 3904

Antoni A., MacLeod M., Ramirez-Ruiz E., 2019, ApJ, 884, 22

Arcavi I., 2018, ApJ, 855, L23

Arcavi I., et al., 2017a, 4, 551, 64

Arcavi I., et al., 2017b, ApJ, 848, L33

Armstrong P., et al., 2021, MNRAS, 507, 3125

Arnett W. D., 1982, ApJ, 253, 785

Arnett W. D., Bahcall J. N., Kirshner R. P., Woosley S. E., 1989, ARA&A, 27, 629

Ashton G., Ackley K., Magaña Hernandez I., Piotrzkowski B., 2020, arXiv e-prints, p. arXiv:2009.12346

Astier P., et al., 2006, A&A, 447, 31

Astropy Collaboration et al., 2013a, A&A, 558, A33

Astropy Collaboration et al., 2013b, A&A, 558, A33

Astropy Collaboration et al., 2018, AJ, 156, 123

Baker T., Bellini E., Ferreira P. G., Lagos M., Noller J., Sawicki I., 2017, Phys. Rev. Lett., 119, 251301

Barbary K., et al., 2022, SNCosmo, Zenodo, doi:10.5281/zenodo.6363879

Barna B., et al., 2021, MNRAS, 501, 1078

Barnes J., Kasen D., Wu M.-R., Mart'inez-Pinedo G., 2016, preprint, (arXiv:1605.07218)

Barthelmy S. D., Butterworth P., Cline T. L., Gehrels N., Fishman G. J., Kouveliotou C., Meegan C. A., 1995, Ap&SS, 231, 235

Bartos I., Kocsis B., Haiman Z., Márka S., 2017, ApJ, 835, 165

Beck R., Szapudi I., Flewelling H., Holmberg C., Magnier E., Chambers K. C., 2021, MNRAS, 500, 1633

Becker A., 2015, HOTPANTS: High Order Transform of PSF ANd Template Subtraction, Astrophysics Source Code Library (ascl:1504.004)

Belczynski K., Kalogera V., Bulik T., 2002, Astrophys. J. , 572, 407

Bellm E. C., et al., 2019a, PASP, 131, 018002

Bellm E. C., et al., 2019b, PASP, 131, 018002

Berger E., 2014, ARA&A, 52, 43

Bertin E., Arnouts S., 1996, A&AS, 117, 393

Bertin E., Mellier Y., Radovich M., Missonnier G., Didelon P., Morin B., 2002, in Bohlender D. A., Durand D., Handley T. H., eds, Astronomical Society of the Pacific Conference Series Vol. 281, Astronomical Data Analysis Software and Systems XI. p. 228

Bilicki M., Jarrett T. H., Peacock J. A., Cluver M. E., Steward L., 2014, ApJS, 210, 9

Binney J., Tremaine S., 2008, Galactic Dynamics: Second Edition. Princeton University Press

Bloom J. S., et al., 2012, ApJ, 744, L17

Boch T., Fernique P., 2014, in Manset N., Forshay P., eds, Astronomical Society of the Pacific Conference Series Vol. 485, Astronomical Data Analysis Software and Systems XXIII. p. 277

Bochenek C. D., Ravi V., Belov K. V., Hallinan G., Kocz J., Kulkarni S. R., McKenna D. L., 2020, 4, 587, 59

Bokeh Development Team 2018, Bokeh: Python library for interactive visualization. https://bokeh.pydata.org/en/latest/

Bonnarel F., et al., 2000, A&AS, 143, 33

Boone K., 2021, AJ, 162, 275

Boubert D., Everall A., Holl B., 2020, MNRAS, 497, 1826

Bradley L., et al., 2022, astropy/photutils: 1.5.0, Zenodo, doi:10.5281/zenodo.6825092

Briceño C., Astronomical Event Observatory Network 2020, The NOIRLab Mirror, 1, 52

Brown T. M., et al., 2013a, PASP, 125, 1031

Brown T. M., et al., 2013b, PASP, 125, 1031

Burbidge E. M., Burbidge G. R., Fowler W. A., Hoyle F., 1957, Reviews of Modern Physics, 29, 547

Burhanudin U. F., Maund J. R., 2022, MNRAS,

CHIME/FRB Collaboration et al., 2020, 4, 587, 54

CHIME/FRB Collaboration et al., 2021, ApJS, 257, 59

Capano C. D., et al., 2020, Nature Astronomy, 4, 625

Chambers K. C., et al., 2016, arXiv e-prints, p. arXiv:1612.05560

Chollet F., others 2018, Keras: The Python Deep Learning library, Astrophysics Source Code Library, record ascl:1806.022 (ascl:1806.022)

Chornock R., et al., 2017, ApJ, 848, L19

Christensen E., et al., 2018, in AAS/Division for Planetary Sciences Meeting Abstracts #50. p. 310.10

Christy C. T., et al., 2022, PASP, 134, 024201

Colless M., et al., 2001, MNRAS, 328, 1039

Cook D. O., et al., 2023, arXiv e-prints, p. arXiv:2306.06271

Coughlin M. W., et al., 2019, ApJ, 885, L19

Coulter D. A., 2021, Teglon: A Pixel-level Gravitational Wave Search Optimization and Analysis Code, doi:10.5281/ZENODO.5683508, https://zenodo.org/record/5683508

Coulter D. A., et al., 2017a, Science, 358, 1556

Coulter D. A., et al., 2017b, Science, 358, 1556

Coulter D. A., et al., 2022, YSE-PZ: An Open-source Target and Observation Management System, Zenodo, doi:10.5281/zenodo.7278430

Coulter D. A., et al., 2023a, PASP, 135, 064501

Coulter D. A., Kilpatrick C. D., Foley R. J., 2023b, Transient Name Server Discovery Report,

2023-1610, 1

Cowperthwaite P. S., et al., 2017, ApJ, 848, L17

Cromartie H. T., et al., 2020, Nature Astronomy, 4, 72

Dalal N., Holz D. E., Hughes S. A., Jain B., 2006, Phys. Rev. D, 74, 063006

Dálya G., et al., 2018, MNRAS, 479, 2374

Dálya G., et al., 2022, MNRAS, 514, 1403

Davis K. W., et al., 2022, arXiv e-prints, p. arXiv:2211.05134

DePoy D. L., et al., 2003, in Iye M., Moorwood A. F. M., eds, Society of Photo-Optical Instrumentation Engineers (SPIE) Conference Series Vol. 4841, Instrument Design and Performance for Optical/Infrared Ground-based Telescopes. pp 827–838, doi:10.1117/12.459907

Dembinski H., et al., 2022, scikit-hep/iminuit: v2.17.0, Zenodo, doi:10.5281/zenodo.7115916

Deng W., Zhang B., 2014, ApJ, 783, L35

Dettman K. G., et al., 2021, ApJ, 923, 267

Dey A., et al., 2019, AJ, 157, 168

Diehl H. T., et al., 2008, in High Energy, Optical, and Infrared Detectors for Astronomy III. p. 702107, doi:10.1117/12.790053

Dimitriadis G., et al., 2019a, ApJ, 870, L1

Dimitriadis G., et al., 2019b, GRB Coordinates Network, 24358, 1

Dimitriadis G., et al., 2022, ApJ, 927, 78

Drake A. J., et al., 2009, ApJ, 696, 870

Drout M. R., et al., 2017, Science, 358, 1570

Evans P. A., et al., 2016, MNRAS, 462, 1591

Filippenko A. V., Li W. D., Treffers R. R., Modjaz M., 2001, in Paczynski B., Chen W.-P., Lemme C., eds, Astronomical Society of the Pacific Conference Series Vol. 246, IAU Colloq. 183: Small Telescope Astronomy on Global Scales. p. 121

Flewelling H. A., et al., 2020, ApJS, 251, 7

Foley 2017, GRB Coordinates Network, 21557

Foley R. J., et al., 2012, ApJ, 744, 38

Foley et al. 2017, GRB Coordinates Network, 21536

Foley R. J., et al., 2018, MNRAS, 475, 193

Foley R. J., Coulter D. A., Kilpatrick C. D., Piro A. L., Ramirez-Ruiz E., Schwab J., 2020, MNRAS, 494, 190

Fong W., Berger E., Margutti R., Zauderer B. A., 2015, ApJ, 815, 102

Fong W., et al., 2019, ApJ, 883, L1

Förster F., et al., 2021, AJ, 161, 242

Freedman W. L., et al., 2001, Astrophys. J. , 553, 47

Freiburghaus C., Rosswog S., Thielemann F.-K., 1999, Astrophys. J. , 525, L121

Frieman J. A., et al., 2008, AJ, 135, 338

Fulton M. D., et al., 2023, arXiv e-prints, p. arXiv:2301.11170

GBM-LIGO 2017, GRB Coordinates Network, 21506

Gagliano A., Narayan G., Engel A., Carrasco Kind M., LSST Dark Energy Science Collaboration 2021, ApJ, 908, 170

Gagliano A., et al., 2022, ApJ, 924, 55

Gaia Collaboration et al., 2021, A&A, 649, A1

Gal-Yam A., et al., 2014, 4, 509, 471

Gardner J. P., et al., 2006, Space Sci. Rev., 123, 485

Gehrels N., Cannizzo J. K., Kanner J., Kasliwal M. M., Nissanke S., Singer L. P., 2016, Astrophys. J. , 820, 136

Ginsburg A., et al., 2019, AJ, 157, 98

Goldstein D. A., et al., 2015, AJ, 150, 82

Goldstein A., et al., 2017, ApJ, 848, L14

Gompertz B. P., et al., 2020, MNRAS, 497, 726

Górski K. M., Hivon E., Banday A. J., Wandelt B. D., Hansen F. K., Reinecke M., Bartelmann M., 2005a, ApJ, 622, 759

Górski K. M., Hivon E., Banday A. J., Wandelt B. D., Hansen F. K., Reinecke M., Bartelmann M., 2005b, ApJ, 622, 759

Górski K. M., Hivon E., Banday A. J., Wandelt B. D., Hansen F. K., Reinecke M., Bartelmann M., 2005c, ApJ, 622, 759

Graham M., Plante R., Tody D., Fitzpatrick M., 2014, PyVO: Python access to the Virtual Observatory, Astrophysics Source Code Library, record ascl:1402.004 (ascl:1402.004)

Graham M. J., et al., 2020, Phys. Rev. Lett., 124, 251102

Green D. W. E., 2002, Central Bureau Electronic Telegrams, 1, 1

Green G., 2018a, The Journal of Open Source Software, 3, 695

Green G. M., 2018b, The Journal of Open Source Software, 3, 695

Gröbner M., Ishibashi W., Tiwari S., Haney M., Jetzer P., 2020, A&A, 638, A119

Guevel D., Hosseinzadeh G., 2017, Dguevel/Pyzogy: Initial Release,

doi:10.5281/zenodo.1043973

Haggard D., Nynka M., Ruan J. J., Kalogera V., Cenko S. B., Evans P., Kennea J. A., 2017, ApJ, 848, L25

Hajela A., et al., 2019, ApJ, 886, L17

Hajela A., et al., 2022, ApJ, 927, L17

Harris C. R., et al., 2020, 4, 585, 357

Hinkle J. T., et al., 2021, MNRAS, 500, 1673

Hirata K., et al., 1987, Phys. Rev. Lett., 58, 1490

Hodgkin S. T., et al., 2021, A&A, 652, A76

Holmbeck E. M., Barnes J., Lund K. A., Sprouse T. M., McLaughlin G. C., Mumpower M. R., 2023, ApJ, 951, L13

Holoien T. W. S., et al., 2020, ApJ, 898, 161

Holz D. E., Hughes S. A., 2005, ApJ, 629, 15

Hosseinzadeh G., et al., 2017, ApJ, 845, L11

Hosseinzadeh G., et al., 2019, ApJ, 880, L4

Howell D. A., Global Supernova Project 2017, in American Astronomical Society Meeting Abstracts #230. p. 318.03

Huber M., Carter Chambers K., Flewelling H., Smartt S. J., Smith K., Wright D., 2015, in IAU General Assembly. p. 2258303

Hung T., et al., 2020, ApJ, 903, 31

Hunter J. D., 2007, Computing in Science & Engineering, 9, 90

INTEGRAL 2017, GRB Coordinates Network, 21507

Jacobson-Galán W. V., et al., 2020a, ApJ, 898, 166

Jacobson-Galán W. V., et al., 2020b, ApJ, 898, 166

Jacobson-Galán W. V., et al., 2022a, ApJ, 924, 15

Jacobson-Galán W. V., et al., 2022b, ApJ, 932, 58

Jencson J. E., et al., 2021, ApJ, 920, 127

Jester S., et al., 2005, AJ, 130, 873

Jones D. H., et al., 2009, MNRAS, 399, 683

Jones D. O., et al., 2019, ApJ, 881, 19

Jones D. O., et al., 2021, ApJ, 908, 143

Joye W. A., Mandel E., 2003, in Payne H. E., Jedrzejewski R. I., Hook R. N., eds, Astronomical Society of the Pacific Conference Series Vol. 295, Astronomical Data Analysis Software and Systems XII. p. 489

Kanner J., Camp J., Racusin J., Gehrels N., White D., 2012, ApJ, 759, 22

Kasen D., Badnell N. R., Barnes J., 2013, Astrophys. J. , 774, 25

Kasliwal M. M., et al., 2017, Science, 358, 1559

Kasliwal M. M., et al., 2019, PASP, 131, 038003

Kenworthy W. D., et al., 2021, ApJ, 923, 265

Kilpatrick C. D., 2023, charliekilpatrick/candidates: candidates v1.0, doi:10.5281/zenodo.8172608, https://doi.org/10.5281/zenodo.8172608

Kilpatrick C. D., et al., 2017, Science, 358, 1583

Kilpatrick C. D., et al., 2018a, MNRAS, 473, 4805

Kilpatrick C. D., et al., 2018b, MNRAS, 481, 4123

Kilpatrick C. D., et al., 2021, ApJ, 923, 258

Kilpatrick C. D., et al., 2022a, ApJ, 926, 49

Kilpatrick C. D., Coulter D. A., Foley R. J., Piro A. L., Rest A., Rojas-Bravo C., Siebert M. R., 2022b, ApJ, 936, 111

Kochanek C. S., et al., 2017, PASP, 129, 104502

Kopparapu R. K., Hanna C., Kalogera V., O'Shaughnessy R., González G., Brady P. R., Fairhurst S., 2008, ApJ, 675, 1459

Kunkel W., et al., 1987, IAU Circ., 4316, 1

LIGO/Virgo collaboration 2017a, GRB Coordinates Network, 21509

LIGO/Virgo collaboration 2017b, GRB Coordinates Network, 21513

LSST Science Collaboration et al., 2009a, preprint, (arXiv:0912.0201)

LSST Science Collaboration et al., 2009b, arXiv e-prints, p. arXiv:0912.0201

Lattimer J. M., Prakash M., 2000, Phys. Rep. , 333, 121

Lattimer J. M., Schramm D. N., 1974, ApJ, 192, L145

Law N. M., et al., 2009, PASP, 121, 1395

Law C. J., et al., 2018, ApJS, 236, 8

Lee W. H., Ramirez-Ruiz E., 2007, New Journal of Physics, 9, 17

Li L.-X., Paczyński B., 1998, Astrophys. J. , 507, L59

Li W., et al., 2011, Mon. Not. R. Astron. Soc. , 412, 1441

Li W., et al., 2019, ApJ, 870, 12

Ligo Scientific Collaboration VIRGO Collaboration 2019, GRB Coordinates Network, 24168, 1

Lipunov V., et al., 2010, Advances in Astronomy, 2010, 349171

Lundquist M. J., et al., 2019, ApJ, 881, L26

Lyman J. D., et al., 2018, Nature Astronomy, 2, 751

Lyutikov M., Barkov M. V., Giannios D., 2020, ApJ, 893, L39

Macquart J.-P., et al., 2010, Publications of the Astronomical Society of Australia, 27, 272

Macquart J. P., et al., 2020, 4, 581, 391

Magnier E. A., et al., 2020, ApJS, 251, 3

Makarov D., Prugniel P., Terekhova N., Courtois H., Vauglin I., 2014, A&A, 570, A13

Makhathini S., et al., 2021, ApJ, 922, 154

Malanchev K., et al., 2022, arXiv e-prints, p. arXiv:2211.07605

Margalit B., Metzger B. D., 2017, ApJ, 850, L19

Margalit B., Berger E., Metzger B. D., 2019, ApJ, 886, 110

Margutti R., et al., 2017, ApJ, 848, L20

Margutti R., et al., 2018, ApJ, 856, L18

Marion G. H., et al., 2016, ApJ, 820, 92

Matheson T., et al., 2021, AJ, 161, 107

McCully C., Volgenau N. H., Harbeck D.-R., Lister T. A., Saunders E. S., Turner M. L., Siiverd R. J., Bowman M., 2018, in Proc. SPIE. p. 107070K (arXiv:1811.04163), doi:10.1117/12.2314340

McLean I. S., et al., 2012, in McLean I. S., Ramsay S. K., Takami H., eds, Society of Photo-Optical Instrumentation Engineers (SPIE) Conference Series Vol. 8446, Ground-based and Airborne Instrumentation for Astronomy IV. p. 84460J, doi:10.1117/12.924794

Merkel D., 2014, Linux J., 2014

Metzger B. D., 2017, Living Reviews in Relativity, 20, 3

Metzger B. D., 2019, Living Reviews in Relativity, 23, 1

Metzger B. D., et al., 2010, Mon. Not. R. Astron. Soc. , 406, 2650

Metzger B. D., Margalit B., Sironi L., 2019, MNRAS, 485, 4091

Miller A. A., et al., 2020, ApJ, 902, 47

Modjaz M., et al., 2009, ApJ, 702, 226

Möller A., et al., 2021, MNRAS, 501, 3272

Moroianu A., Wen L., James C. W., Ai S., Kovalam M., Panther F. H., Zhang B., 2023, Nature Astronomy, 7, 579

Morris B. M., et al., 2018, AJ, 155, 128

Most E. R., Nathanail A., Rezzolla L., 2018, ApJ, 864, 117

Mould J., et al., 1990, Astrophys. J. , 353, L35

Murguia-Berthier A., et al., 2017, ApJ, 848, L34

Nation J., Bowman M., Daily M., Lister T. A., Sohi J., Storrie-Lombardi L. J., Street R. A., 2022, in Adler D. S., Seaman R. L., Benn C. R., eds, Society of Photo-Optical Instrumentation Engineers (SPIE) Conference Series Vol. 12186, Observatory Operations: Strategies, Processes, and Systems IX. p. 121860Q, doi:10.1117/12.2629809

Neustadt J. M. M., et al., 2020, MNRAS, 494, 2538

Nicholl M., Short P., Wiseman P., Pursiainen M., Angus C., Yaron O., 2019, Transient Name Server Classification Report, 2019-642, 1

Nordin J., et al., 2019, A&A, 631, A147

Nynka M., Ruan J. J., Haggard D., Evans P. A., 2018, ApJ, 862, L19

Oates S. R., et al., 2021, MNRAS, 507, 1296

Ofek E. O., et al., 2010, ApJ, 724, 1396

Oke J. B., Gunn J. E., 1983, ApJ, 266, 713

One-Meter Two-Hemisphere (1M2H) collaboration 2017, GRB Coordinates Network, 21529

Oppenheimer J. R., Volkoff G. M., 1939, Physical Review, 55, 374

Pan Y.-C., et al., 2015, Mon. Not. R. Astron. Soc. , 452, 4307

Pan Y. C., et al., 2017, ApJ, 848, L30

Panther F. H., et al., 2023, MNRAS, 519, 2235

Pâris I., et al., 2017, A&A, 597, A79

Pastorello A., et al., 2022, arXiv e-prints, p. arXiv:2208.02782

Paterson K., et al., 2021, ApJ, 912, 128

Pedregosa F., et al., 2011, Journal of Machine Learning Research, 12, 2825

Persson S. E., et al., 2013, Publ. Astron. Soc. Pac. , 125, 654

Phinney E. S., 1991, Astrophys. J. , 380, L17

Pian E., et al., 2017, 4, 551, 67

Piro L., et al., 2019, MNRAS, 483, 1912

Pooley D., Kumar P., Wheeler J. C., Grossan B., 2018, ApJ, 859, L23

Prochaska J. X., et al., 2020a, pypeit/PypeIt: Release 1.0.0, doi:10.5281/zenodo.3743493

Prochaska J., et al., 2020b, The Journal of Open Source Software, 5, 2308

Rajwade K. M., et al., 2022, MNRAS, 514, 1961

Rau A., et al., 2009, PASP, 121, 1334

Rest A., et al., 2005, ApJ, 634, 1103

Rest A., et al., 2014, ApJ, 795, 44

Roberts L. F., Kasen D., Lee W. H., Ramirez-Ruiz E., 2011, ApJ, 736, L21

Roming P. W. A., et al., 2005, Space Sci. Rev., 120, 95

Rosswog S., Piran T., Nakar E., 2013, MNRAS, 430, 2585

Ruan J. J., Nynka M., Haggard D., Kalogera V., Evans P., 2018, ApJ, 853, L4

Ruiz M., Shapiro S. L., Tsokaros A., 2018, Phys. Rev. D, 97, 021501

Rutledge R. E., 1998, PASP, 110, 754

Saha A., Matheson T., Snodgrass R., Kececioglu J., Narayan G., Seaman R., Jenness T., Axelrod T., 2014, in Peck A. B., Benn C. R., Seaman R. L., eds, Society of Photo-Optical Instrumentation Engineers (SPIE) Conference Series Vol. 9149, Observatory Operations: Strategies, Processes, and Systems V. p. 914908 (arXiv:1409.0056), doi:10.1117/12.2056988

Savchenko V., et al., 2017, ApJ, 848, L15

Schechter P., 1976, ApJ, 203, 297

Schechter P. L., Mateo M., Saha A., 1993, PASP, 105, 1342

Schlafly E. F., Finkbeiner D. P., 2011, ApJ, 737, 103

Schlegel D. J., Finkbeiner D. P., Davis M., 1998, ApJ, 500, 525

Scolnic D., et al., 2015, Astrophys. J. , 815, 117

Secrest N. J., Dudik R. P., Dorland B. N., Zacharias N., Makarov V., Fey A., Frouard J., Finch C., 2015, ApJS, 221, 12

Shappee B. J., et al., 2014, ApJ, 788, 48

Shappee B. J., et al., 2016, Astrophys. J. , 826, 144

Shappee B. J., et al., 2017, Science, 358, 1574

Shappee B. J., et al., 2019, ApJ, 870, 13

Shibata M., Taniguchi K., 2006, Phys. Rev. D, 73, 064027

Shibata M., Fujibayashi S., Hotokezaka K., Kiuchi K., Kyutoku K., Sekiguchi Y., Tanaka M., 2017, Phys. Rev. D, 96, 123012

Shingles L., et al., 2021, Transient Name Server AstroNote, 7, 1

Siebert M. R., et al., 2017, ApJ, 848, L26

Simon et al. 2017, GRB Coordinates Network, 21551

Singer L. P., Price L. R., 2016, Phys. Rev. D, 93, 024013

Singer L. P., et al., 2016a, ApJS, 226, 10

Singer L. P., et al., 2016b, ApJ, 829, L15

Skrutskie M. F., et al., 2006, AJ, 131, 1163

Smartt S. J., et al., 2015, A&A, 579, A40

Smartt S. J., et al., 2016, MNRAS, 462, 4094

Smartt S. J., et al., 2017, 4, 551, 75

Smith D. G. A., Gray J., 2018, Journal of Open Source Software, 3, 753

Smith R. C., et al., 2002, in American Astronomical Society Meeting Abstracts. p. 78.08

Smith K. W., et al., 2020, PASP, 132, 085002

Soares-Santos M., et al., 2016, ApJ, 823, L33

Soares-Santos M., et al., 2017, ApJ, 848, L16

Soderberg A. M., et al., 2008, 4, 453, 469

Spergel D., et al., 2015, arXiv e-prints, p. arXiv:1503.03757

Steeghs D., et al., 2022, MNRAS, 511, 2405

Sternberg A., et al., 2011, Science, 333, 856

Street R. A., Bowman M., Saunders E. S., Boroson T., 2018, in Guzman J. C., Ibsen J., eds, Society of Photo-Optical Instrumentation Engineers (SPIE) Conference Series Vol. 10707, Software and Cyberinfrastructure for Astronomy V. p. 1070711 (arXiv:1806.09557), doi:10.1117/12.2312293

Swift J. J., et al., 2022, PASP, 134, 035005

Tachibana Y., Miller A. A., 2018, PASP, 130, 128001

Tanaka M., Kato D., Gaigalas G., Kawaguchi K., 2020, MNRAS, 496, 1369

Tanvir N. R., Levan A. J., Fruchter A. S., Hjorth J., Hounsell R. A., Wiersema K., Tunnicliffe R. L., 2013, 4, 500, 547

Tanvir N. R., et al., 2017, ApJ, 848, L27

Tartaglia L., et al., 2018, ApJ, 853, 62

Team T. P. D., 2022, pandas-dev/pandas: Pandas, Zenodo, doi:10.5281/zenodo.7344967

Terreran G., et al., 2022, ApJ, 926, 20

The HDF Group 1997, Hierarchical Data Format, version 5

The LIGO Scientific Collaboration et al., 2021, arXiv e-prints, p. arXiv:2111.03606

Thorne K. S., 1987, Gravitational radiation.. pp 330–458

Tinyanont S., et al., 2022, MNRAS, 512, 2777

Tolman R. C., 1939, Physical Review, 55, 364

Tonry J. L., et al., 2018, PASP, 130, 064505

Troja E., et al., 2018, MNRAS, 478, L18

Troja E., et al., 2019, MNRAS, 489, 1919

Troja E., et al., 2020, MNRAS, 498, 5643

Tsapras Y., et al., 2009, Astronomische Nachrichten, 330, 4

Valenti S., et al., 2016, MNRAS, 459, 3939

Van Kemenade H., et al., 2022, python-pillow/Pillow: 9.2.0, Zenodo, doi:10.5281/zenodo.6788304

Van Kerkwijk M., 2021, liberfa/pyerfa: v2.0.0, Zenodo, doi:10.5281/zenodo.3940698

Virtanen P., et al., 2020, Nature Methods, 17, 261

Walmsley M., et al., 2020, MNRAS, 491, 1554

Wang Q., et al., 2021, ApJ, 923, 167

Ward S. M., et al., 2022, arXiv e-prints, p. arXiv:2209.10558

Waskom M. L., 2021, Journal of Open Source Software, 6, 3021

White D. J., Daw E. J., Dhillon V. S., 2011, Classical and Quantum Gravity, 28, 085016

Williams G. G., 2018, in Marshall H. K., Spyromilio J., eds, Society of Photo-Optical Instrumentation Engineers (SPIE) Conference Series Vol. 10700, Ground-based and Airborne Telescopes VII. p. 107002T, doi:10.1117/12.2314422

Wilson J. C., et al., 2004, in Moorwood A. F. M., Iye M., eds, Society of Photo-Optical Instrumentation Engineers (SPIE) Conference Series Vol. 5492, Ground-based Instrumentation for Astronomy. pp 1295–1305, doi:10.1117/12.550925

Wright E. L., et al., 2010, AJ, 140, 1868

Wright D. E., et al., 2017, MNRAS, 472, 1315

Wu Y., MacFadyen A., 2018, ApJ, 869, 55

Wu Y., MacFadyen A., 2019, ApJ, 880, L23

Wyatt S. D., Tohuvavohu A., Arcavi I., Lundquist M. J., Howell D. A., Sand D. J., 2020, ApJ, 894, 127

Yang Y., et al., 2020, ApJ, 902, 46

York D. G., et al., 2000, AJ, 120, 1579

Zackay B., Ofek E. O., Gal-Yam A., 2016, ApJ, 830, 27

Zevin M., et al., 2017, Classical and Quantum Gravity, 34, 064003

Zhang B., 2013, ApJ, 763, L22

Zhang B., 2022, arXiv e-prints, p. arXiv:2212.03972

Zhou B., Li X., Wang T., Fan Y.-Z., Wei D.-M., 2014, Phys. Rev. D, 89, 107303

Zhou R., et al., 2021, MNRAS, 501, 3309

Zonca A., Singer L., Lenz D., Reinecke M., Rosset C., Hivon E., Gorski K., 2019a, Journal of Open Source Software, 4, 1298

Zonca A., Singer L., Lenz D., Reinecke M., Rosset C., Hivon E., Gorski K., 2019b, The Journal of Open Source Software, 4, 1298

Zonca A., Singer L., Lenz D., Reinecke M., Rosset C., Hivon E., Gorski K., 2019c, Journal of Open Source Software, 4, 1298

van der Walt S. J., Crellin-Quick A., Bloom J. S., 2019, Journal of Open Source Software, 4